

# Design and Testing of a Scale-Model Surface Undersea Kite (SUSK)

A Major Qualifying Project Report  
Submitted to the Faculty of the  
WORCESTER POLYTECHNIC INSTITUTE  
in Partial Fulfillment of the Requirements for the  
Degree(s) of Bachelor of Science in:


Aerospace Engineering

by:



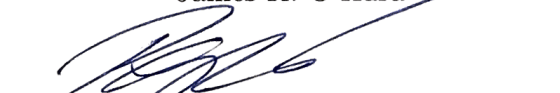
---

Austin J. Higgins




---

James K. O'Hara



---

Mladen Pepic

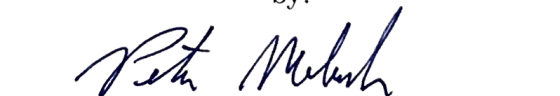


---

Derek J. Porter

Aerospace Engineering and Physics


by:



---

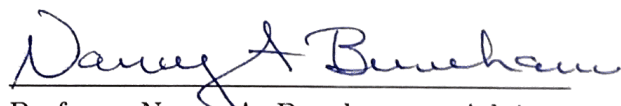
Peter D. Melander

Approved by:



---

Professor David J. Olinger, co-Advisor  
Aerospace Engineering Program  
Mechanical Engineering Department, WPI



---

Professor Nancy A. Burnham, co-Advisor  
Physics Department &  
Biomedical Engineering Department, WPI

# Table of Contents

---

Abstract . . . . .	iv
Table of Authorship . . . . .	v
Acknowledgements . . . . .	vi
List of Figures . . . . .	vii
List of Tables . . . . .	x
Nomenclature . . . . .	xi
<b>1 Introduction</b>	<b>1</b>
1.1 Renewable Energy . . . . .	2
1.1.1 Hydrocarbon and Fossil Fuel Issues . . . . .	2
1.1.2 Use of Air and Water Currents . . . . .	3
1.2 Tethered Energy . . . . .	3
1.2.1 Cross-current Motion . . . . .	3
1.2.2 AWE . . . . .	4
1.2.3 TUSK . . . . .	5
1.3 Commerical AWE and TUSK Systems . . . . .	5
1.4 Past WPI Project Work on TUSK . . . . .	6
1.5 Goal and Objectives . . . . .	7
<b>2 Design</b>	<b>9</b>
2.1 Hull Design . . . . .	9
2.2 Airfoil Design . . . . .	11
2.2.1 Overall Considerations . . . . .	11
2.2.2 XF5R5 Simulations . . . . .	14
2.2.3 Force Analysis . . . . .	16
2.2.4 Force Analysis Results . . . . .	17
2.2.5 Wind Tunnel Testing . . . . .	18
2.3 Turbine Design . . . . .	20
2.4 Other Design Considerations . . . . .	21

2.4.1	Buoyancy and Stability . . . . .	21
2.4.2	Water Absorption . . . . .	23
<b>3</b>	<b>Fabrication</b>	<b>24</b>
3.1	General System Overview . . . . .	24
3.2	Main Body . . . . .	25
3.2.1	Water Proofing . . . . .	27
3.3	Tether Connection . . . . .	27
3.4	Gimbal and Control Box . . . . .	29
3.5	Turbine Assembly . . . . .	31
<b>4</b>	<b>Testing</b>	<b>33</b>
4.1	Water Tank Test . . . . .	33
4.2	WPI Pool Test without Turbine . . . . .	33
4.3	Tests at Alden Research Laboratory . . . . .	34
<b>5</b>	<b>Simulations of SUSK System</b>	<b>43</b>
5.1	Equations of Motion . . . . .	43
5.1.1	Simplification of TUSK Simulation . . . . .	44
5.1.2	Derivations From First Principles . . . . .	46
5.2	Development of Generalized Hydrodynamic Forces . . . . .	46
5.2.1	Drag of Turbine and Hull . . . . .	47
5.2.2	Lift and Drag of Wing . . . . .	47
5.2.3	Leading Edge and Effective Angle of Attack . . . . .	51
5.2.4	Adjustment of Wing Angle . . . . .	56
5.3	Post-processing of Simulation Results . . . . .	57
5.3.1	Simulation Outputs . . . . .	57
5.4	Simulation Results Compared to Tests . . . . .	63
5.5	Sensitivity Study . . . . .	68
5.6	Scaled-Up Simulation Results and Comparison . . . . .	75
<b>6</b>	<b>Discussion and Conclusions</b>	<b>81</b>

7	Future Work	83
A	XFLR5 Wing Testing Wind Tunnel	84
B	Wiring Chart for Gimbal and Control Box	88
C	Arduino Code for Servo Control and Data Logging	89
D	Table of Test Runs from Alden Research Laboratory	91
E	TUSK Equations of Motion	92
F	Derivation of Lagrangian for TUSK	94
G	Equations of Motion from Derived Lagrangian	98
H	Derivation of SUSK Lagrangian	101
I	Derivation of Boat Equations of Motion Using Newton's Laws	102
J	MATLAB <sup>®</sup> Code for Dynamic Simulations	103
	References	113

# Abstract

---

Surface Undersea Kites (SUSK) is a concept for extracting energy from tidal flows with a tethered boat. Existing work in Airborne Wind Energy (AWE) and Tethered Undersea Kites (TUSK) has shown tethered kites to be a viable renewable energy technology in both air and water currents. SUSK employs a tethered boat with a submerged, vertical wing rather than a fully submerged kite to increase energy output by eliminating drag on an underwater tether. A half-chord symmetric airfoil below the boat is used to drive the planar, reversing motion of the boat, and this rarely used airfoil type is shown to have lift characteristics comparable with common airfoils. A scale-model SUSK system has been designed and constructed using mainly 3D printed components including a streamlined surface boat hull, an underwater wing, a dragging turbine assembly, and a carbon fiber tether attached to a stationary gimbal above the water surface. Dynamic simulations of the system, incorporating boat and tether dynamics, have also been developed to obtain power estimates for the scale-model and full-size SUSK systems. The scale-model system was tested in a large water flume at a local hydraulics laboratory, and its performance was comparable to performance predicted by the dynamic simulations. Recommendations are made to improve the initial SUSK system design.

Certain materials are included under the fair use exemption of the U.S. Copyright Law and have been prepared according to the fair use guidelines and are restricted from further use.

# Authorship Table

---

Section	Author(s) of section	Project work completed by
1	All	N/A
1.1.1	AH	N/A
1.1.2	AH	N/A
1.2	PM	N/A
1.2.1	PM, JO	N/A
1.2.2	PM, JO	N/A
1.2.3	JO	N/A
1.3	JO, MP	N/A
1.4	MP	N/A
1.5	JO, MP	N/A
2	DP	All
2.1	AH, PM, JO, DP	AH, PM, JO, MP
2.2.1	PM, JO, DP	AH, JO, DP
2.2.2	JO	JO, DP
2.2.3	JO	JO
2.2.4	PM, JO	AH
2.2.5	JO, DP	All
2.3	DP	DP, PM
2.4.1	PM, JO	AH, PM
2.4.2	PM, JO	AH, PM
3.1	JO, MP	AH, PM
3.2	MP	AH, PM
3.2.1	JO, MP	AH, PM, MP
3.3	MP	AH, PM, MP
3.4	AH	AH
3.5	PM, MP	PM, DP
4.1	JO	AH, PM
4.2	JO	All
4.3	AH, PM	All
5 (All)	PM	PM***
6	AH, PM	N/A
7	AH	N/A
A	PM	All
B	AH	All
C	AH	All
D	AH, PM	All
E-J	PM	PM***
		Key
AH		Austin Higgins
PM		Peter Melander
JO		James O'Hara
MP		Mladen Pepic
DP		Derek Porter
*** Represents work completed specifically for double major in Physics		

# Acknowledgements

---

The SUSK MQP team would like to recognize the following people for their efforts that were critical to the success of our project:

- Erica Stults - WPI Rapid Prototyping, for assisting with the fabrication of parts of the SUSK system
- James Loiselle, Lily Ouellette - WPI Manufacturing Labs, for assisting with the fabrication of parts of the SUSK system
- Paul Bennett - WPI Athletics, for use of the WPI swimming pool for preliminary testing of the SUSK system
- Brian McMahon, Nicholas Lucia - Alden Research Laboratories, for use of the 20 ft × 10 ft water flume for testing of the SUSK system and for their support and assistance during the testing process
- Professor David J. Olinger, Professor Nancy A. Burnham - Project Advisors, for assistance and insight throughout the project
- Amirmahdi Ghasemi, Yao Wang, Haocheng Li - Graduate students under Professor Olinger working with TUSK, for answering questions and generally supporting project work

# List of Figures

---

1	TUSK and SUSK Concepts . . . . .	2
2	Differences between wind turbine and AWE motion . . . . .	4
3	WPI TUSK Pool Test . . . . .	7
4	Final SUSK boat design, image and CAD . . . . .	9
5	Boat Hull Design Candidates . . . . .	10
6	Different cases for movement of the SUSK boat . . . . .	12
7	Airfoil Symmetry . . . . .	13
8	Airfoil Models for XFLR5 Simulations . . . . .	15
9	Force Analysis Diagram . . . . .	17
10	Airfoil Shapes for Wind Tunnel Testing . . . . .	19
11	Wind Tunnel Testing of Airfoils . . . . .	19
12	Wind Tunnel Testing Results . . . . .	20
13	CAD Rendering of turbine assembly . . . . .	21
14	Final Scale-model SUSK system . . . . .	24
15	CAD Rendering of final SUSK system . . . . .	25
16	Main Body Design and Wing with Shaft . . . . .	26
17	Caption . . . . .	26
18	Waterproofing process . . . . .	27
19	Carbon-fibred Tether . . . . .	28
20	Tether mount . . . . .	28
21	Tether Joint and Holder . . . . .	28
22	Rewiring of the Gimbal . . . . .	29
23	SUSK control box . . . . .	31
24	Components of the turbine assembly . . . . .	32
25	SUSK system with finalized turbine assembly . . . . .	32
26	Initial Pool Test Setup . . . . .	34
27	Recorded data for Test 47 with a current velocity of $0.5 \frac{\text{ft}}{\text{s}}$ . . . . .	39
28	Recorded data for Test 49 with a current velocity of $0.5 \frac{\text{ft}}{\text{s}}$ . . . . .	39



29	Recorded data for Test 23 with a current velocity of $1.0 \frac{\text{ft}}{\text{s}}$ . . . . .	40
30	Recorded data for Test 29 with a current velocity of $1.0 \frac{\text{ft}}{\text{s}}$ . . . . .	40
31	Recorded data for Test 33 with a current velocity of $1.5 \frac{\text{ft}}{\text{s}}$ . . . . .	41
32	Recorded data for Test 35 with a current velocity of $1.5 \frac{\text{ft}}{\text{s}}$ . . . . .	41
33	Recorded data for Test 45 with a current velocity of $2.0 \frac{\text{ft}}{\text{s}}$ . . . . .	42
34	Recorded data for Test 46 with a current velocity of $2.0 \frac{\text{ft}}{\text{s}}$ . . . . .	42
35	Diagram of TUSK Coordinates . . . . .	45
36	Lift coefficient and drag coefficient fitted using splines . . . . .	48
37	Boat Motion Diagram . . . . .	51
38	SUSK Diagram . . . . .	53
39	Sample output of simulation run, part 1 . . . . .	58
40	Sample output of simulation run, part 2 . . . . .	59
41	Sample output of simulation run, part 3 . . . . .	60
42	Testing and simulation comparison for Test 47 with a current velocity of $0.5 \frac{\text{ft}}{\text{s}}$ .	64
43	Testing and simulation comparison for Test 49 with a current velocity of $0.5 \frac{\text{ft}}{\text{s}}$ .	64
44	Testing and simulation comparison for Test 23 with a current velocity of $1.0 \frac{\text{ft}}{\text{s}}$ .	65
45	Testing and simulation comparison for Test 29 with a current velocity of $1.0 \frac{\text{ft}}{\text{s}}$ .	65
46	Testing and simulation comparison for Test 33 with a current velocity of $1.5 \frac{\text{ft}}{\text{s}}$ .	66
47	Testing and simulation comparison for Test 35 with a current velocity of $1.5 \frac{\text{ft}}{\text{s}}$ .	66
48	Testing and simulation comparison for Test 45 with a current velocity of $2.0 \frac{\text{ft}}{\text{s}}$ .	67
49	Testing and simulation comparison for Test 46 with a current velocity of $2.0 \frac{\text{ft}}{\text{s}}$ .	67
50	Sensitivity Study 0 - Baseline . . . . .	69
51	Sensitivity Study 1 - Boat mass $\times 5$ . . . . .	70
52	Sensitivity Study 2 - Boat mass and tether density $\times 5$ . . . . .	70
53	Sensitivity Study 3 - Tether length $\times 3$ . . . . .	71
54	Sensitivity Study 4 - Current speed $\times 2$ . . . . .	71
55	Sensitivity Study 5 - Current speed $\times 0.5$ . . . . .	72
56	Sensitivity Study 6 - $q_{2,\text{lim}} = 20^\circ$ instead of $40^\circ$ . . . . .	72
57	Sensitivity Study 7 - $q_{2,\text{lim}} = 30^\circ$ instead of $40^\circ$ . . . . .	73
58	Sensitivity Study 8 - $q_{2,\text{lim}} = 45^\circ$ instead of $40^\circ$ . . . . .	73

59	Sensitivity Study 9 - Hull drag $\times 0.5$ . . . . .	74
60	Sensitivity Study 10 - Boat size $\times 1.2$ . . . . .	74
61	Small-scale simulation comparison cartesian output. . . . .	76
62	Large-scale simulation comparison cartesian output. . . . .	76
63	Small-scale simulation comparison angular data output. . . . .	77
64	Large-scale simulation comparison angular data output. . . . .	78
65	Small-scale simulation comparison miscellaneous data output. . . . .	79
66	Large-scale simulation comparison miscellaneous data output. . . . .	80

# List of Tables

---

1	Comparison of pros and cons of candidate SUSK hull designs. . . . .	11
2	Force Generated at Maximum Lift Coefficient . . . . .	18
3	Force Generated at Maximum Lift to Drag Ratio . . . . .	18
4	Surface Area, Volume, and resultant Mass of SUSK Components . . . . .	22
5	Scale-Model and Full-Size Simulation Parameters . . . . .	44
6	Simplification of TUSK degrees of freedom to SUSK parameters . . . . .	46
7	Four cases of apparent flow over the wing . . . . .	51
8	Cases of state and their trim $\theta$ for control . . . . .	57
9	Summary of sensitivity study simulation runs . . . . .	68
10	Data from wind tunnel tests used to nondimensionalize lift and drag results .	84
11	Small-scale wind tunnel testing data for Airfoil 12 (candidate optimal airfoil)	85
12	Small-scale wind tunnel testing data for Airfoil 3 (less cambered than candi- date optimal airfoil) . . . . .	86
13	Small-scale wind tunnel testing data for Airfoil 10 (thinner than candidate optimal airfiol) . . . . .	87

# Nomenclature

---

$A$	Axial force
$c$	Chord length
$C_L$	Coefficient of lift
$C_D$	Coefficient of drag
$C_P$	Coefficient of power
$D$	Drag
$F$	Force
$F_p$	Force parallel to tether
$F_n$	Force normal to tether
$g$	Gravitational constant
$J_i$	$J^{\text{th}}$ principal moment of inertia
$K$	Kinetic Energy
$L$	Lift
$L_t$	Tether length
$m$	Mass
$N$	Normal Force
$\mathcal{L}$	Lagrangian
$P$	Power
$q$	Dynamic pressure
$q_2$	Angular position of boat
$q_i$	Generalized coordinate
$Q_{q_i}$	Generalized force associated with the $q_i$ coordinate
$r$	Radial position
$\mathbf{r}_{\text{boat}}$	Boat position
$RB$	Reserve buoyancy
$S$	Area
$s$	Distance along tether
$T$	Tension
$U$	Potential Energy
$\mathbf{V}_c$	Ambient current velocity vector
$V_{\text{current}} =  \mathbf{V}_c $	Ambient current velocity magnitude
$\mathbf{V}_{c,\text{total}}$	Total apparent current velocity
$V_a =  \mathbf{V}_{c,\text{total}} $	Total apparent current velocity magnitude
$\mathbf{V}_{\text{boat}}$	Boat velocity
$\hat{\mathbf{w}}$	Unit vector parallel to wing direction
$\alpha$	Angle of attack
$\alpha_{\text{eff}}$	Effective angle of attack
$\rho$	Density
$\rho_c$	Tether linear density
$\rho_b$	TUSK buoyant density
$\theta$	Wing angle with respect to cartesian system
$\phi$	Apparent velocity angle with respect to cartesian system
$\boldsymbol{\omega}$	Angular velocity vector
$\tau$	Torque

# Chapter 1: Introduction

---

To counteract the dependence on fossil fuel power, many forms of renewable energy are emerging as options to power the world. Many naturally occurring phenomena contain large quantities of stored energy which current renewable energy technologies are only starting to harness. In particular, stationary turbines draw energy from natural wind and tidal currents. These systems, however, are limited by the speed of fluid flow through the turbine. As a way to improve the energy drawn from these resources, tethered mobile vehicles have been developed to increase effective flow velocities through turbines. The system works by harnessing the power of the flow to move the tethered vehicle in the cross-current direction, often at speeds several times the speed of the current. This causes the turbine to experience a flow speed far greater than the current flow. Tethered vehicles were first studied in air, and this concept is known as Airborne Wind Energy (AWE) [1, 2]. Due to the higher power density, this concept was then studied in ocean currents, known as Tethered Undersea Kites (TUSK) [3]. Studies have shown that AWE and TUSK are feasible methods to improve on stationary wind and water turbines.

This project conducted preliminary studies and simulations based around a new tethered mobile vehicle system, known as Surface Undersea Kites (SUSK). This concept was conceived and patented by HydroRun Technologies, Ltd in 2013 [4]. The SUSK implements a boat as the tethered vehicle and keeps the turbine underwater. This keeps many of the positives of TUSK over AWE, but also will allow the tether to remain in air. While a kite in the TUSK system is moving underwater, the tether is also moving through the water, which causes a significant amount of drag. According to [3], "tether drag can be a substantial portion of total system drag; initial estimates show that the tether drag for a 60 mm diameter tether would be about 60% of the kite drag." Meanwhile, SUSK can potentially significantly reduce tether drag. Additionally, kites in AWE and TUSK move in three dimensional figure eight patterns, while SUSK boats will sweep out a two dimensional arc, simplifying simulations and reducing control complexity. A comparison of the TUSK and SUSK systems is shown in Figure 1.

The following sections will lay review previous work done with AWE and TUSK, both

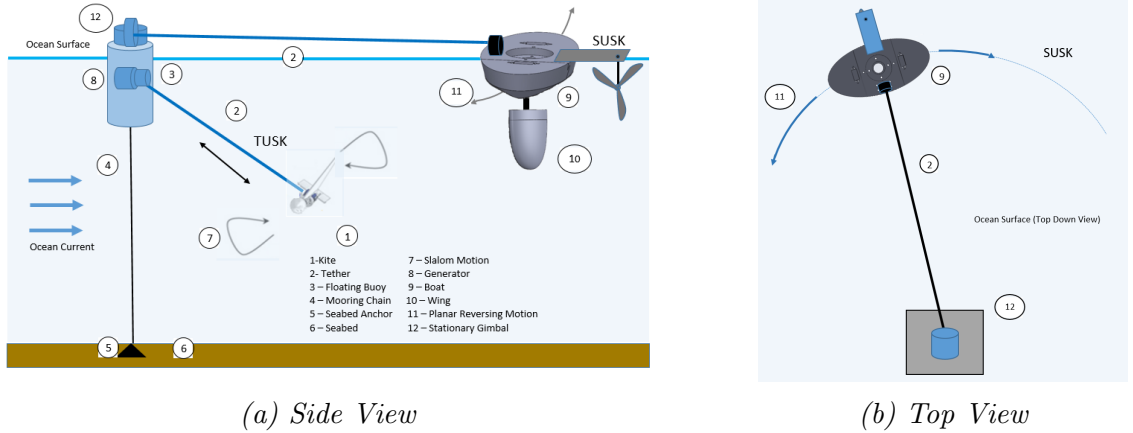


Figure 1: Comparison of the TUSK and SUSK system concepts.

at WPI and in industry, and will explain how SUSK will both extend that work and differ from it.

## 1.1 Renewable Energy

### 1.1.1 Hydrocarbon and Fossil Fuel Issues

Fossil Fuels are one of the most common power sources in today's culture. Fossil fuels make up 75% of all greenhouse gas emissions, and are a nonrenewable resource [5]. Greenhouse gasses cause a temperature increase over long periods of time, and after certain points, may become irreversible [6]. While not only being harmful to the environment, fossil fuels are a limited resource that will at some point no longer be able to be used. Newer methods have been discovered and improved on over time (such as pumpjack systems for oil harvesting, and better tools for hydraulic fracking), but after a certain point there will be nothing left to harvest, no matter how advanced the extraction methods get.

Outside of global climate change, emissions from the burning of fossil fuels can cause harmful effects on humans, including respiratory irritation or disease, and lung cancer. The large use of fossil fuels in densely packed cities in countries like China have caused a large amount of damage to their residents, and some have even had smog clouds to the point of limiting visibility [7].

## 1.1.2 Use of Air and Water Currents

Due to the negative effects and non-renewable nature of fossil fuels, many companies have turned towards power sources such as solar, wind, and hydroelectric energy. These types of energy sources are renewable, which means that the amount you use them has no bearing on its future output. Wind energy, for example, is mostly captured using windmills or wind turbines that spin with a wind current to charge batteries or generators. Most hydroelectric power is taken from dams and turbines placed underwater in either fast or large currents of water. Solar power does not require any moving parts, but rather uses photoelectric cells and the sun's light to generate power with solar panels. Wind and solar energy are widely used, as all they require is a location to place them, and sufficient energy to drive them. For wind, this is large open areas without tall mountains or buildings (some turbines are even placed in open water to take advantage of ocean wind currents). Solar energy just needs a wide, unobstructed view of the sun, and in some cases, the panels can pivot to always face the sun to maximize power output.

Hydroelectric power runs into the issue of needing a specific type of area to be set up. Dams are the usual location to harness hydroelectric power, but there is a smaller limit to how many dams we can create, and how much power we can extract from those dams. This leaves us with trying to find other ways to use the power of moving water to expand on the current technology.

## 1.2 Tethered Energy

Tethered vehicle energy harvesting (i.e. AWE and TUSK) is a method of optimizing the energy that can be obtained from a flow. Current methods of extracting renewable energy harness only a small fraction of the total energy available in most sources. For example, the Florida Current of the Gulf Stream has an estimated energy potential of  $50 \frac{\text{TW}\cdot\text{hr}}{\text{yr}}$  and could power millions of US homes if efficiently harvested [8].

### 1.2.1 Cross-current Motion

Stationary wind and water turbines are limited by the speed of the flow over them. Increasing the speed at which a flow passes over a power harvesting turbine will increase the

power output. With tethered vehicles that carry turbines, aerodynamic surfaces drive the vehicle across the current to allow the turbine to experience higher apparent flow velocities. [9] showed that cross-current velocities of tethered vehicles depend on their overall lift to drag ratios such that

$$V_a = \frac{2}{3}V_{current} \left( \frac{C_L}{C_D} \right). \quad (1.1)$$

Additionally, [9] showed that the power generated by a cross-current moving vehicle can be as high as

$$P = \frac{2}{27}\rho V_a^3 S C_L \left( \frac{C_L}{C_D} \right). \quad (1.2)$$

The presence of the lift over drag terms shows that the presence of aerodynamic surfaces which produce lift from the flow greatly increase the power that can be produced by moving vehicles as compared to stationary turbines.

### 1.2.2 AWE

Tethered airborne energy systems can reach higher altitudes and larger areas than stationary turbines [10]. Estimates have shown that tethered wind energy systems can produce up to five times the power of their stationary counterparts [1]. Tethered kites travel in a cross current pattern, making a figure eight. This is contrasted with the circular motion of a conventional wind turbine in Figure 2.

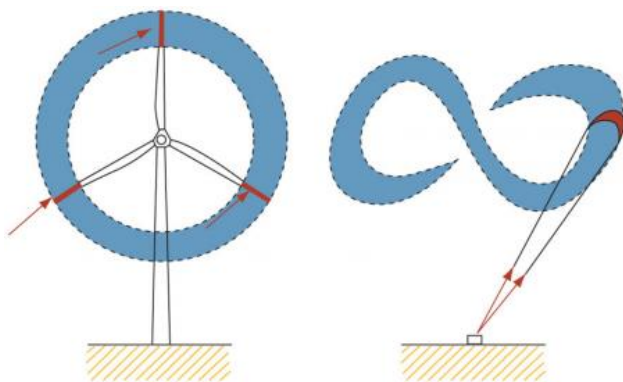


Figure 2: Differences between stationary wind turbine motion (left) and AWE system motion (right), from [11] Copyright ©2011 RTC Group, Inc.



### 1.2.3 TUSK

Tethered underwater energy systems have many advantages over conventional undersea turbines. TUSK systems can be used in a wider range of locations, including those where current flows are too slow for turbines. Additionally, TUSK systems are more efficient, simple to maintain, less expensive, and their implementation can be scaled easily [12]. Stationary underwater power systems often involve dams which not only require significantly more material but also disrupt wildlife by completely blocking off the river. TUSK systems also have advantages over similar AWE systems. TUSK evolved from AWE, motivated by the higher power density of water. According to simple calculations, TUSK can produce over 10 times the power of AWE [3].

## 1.3 Commerical AWE and TUSK Systems

Although not yet commonplace, kite power is not new in industry. Most recent studies and work have been focused on airborne wind energy (AWE) kite systems. Windlift, a small company, aims to produce prototype AWE systems off the coast of North Carolina in the next five years [13]. Other companies have been developing TUSK systems, such as Minesto and HydroRun Technologies.

Minestos Deep Green Technology focuses primarily on attached turbine-kites, which generates power from the water current. The team in Minesto has been able to achieve underwater kite speeds 10 times higher than that of the water current [14]. The kites are designed to operate cost-effectively at water sites with depths between 60 m and 120 m and velocities between  $1.2 \frac{\text{m}}{\text{s}}$  and  $2.5 \frac{\text{m}}{\text{s}}$  [15].

HydroRun Technologies is another company that has been focusing on developing tethered powered kite systems, referred to as Freestream Gliders. These gliders use hydrodynamic principles, moving underwater in the trajectory of a pendulum. Water rushes across the Glider, generating lift that pulls on its 40 m tether to generate electricity. HydroRuns Freestream Glider is recorded as producing an output of 40 kW at  $2.5 \frac{\text{m}}{\text{s}}$  of current speed, with an operating range of  $1.5 \frac{\text{m}}{\text{s}}$  to  $8 \frac{\text{m}}{\text{s}}$  of current speed [16].

Upon researching patent information for a SUSK-type system, a similar patent was dis-

covered for a tethered water surface power generator. The international patent number is WO 2014/063258 A1 [4], and is owned by HydroRun Technologies Inc. Included in this patent is a diagram and design for a tethered floating hull with a vertical wing. In the patent, the design is listed under Figure 11 is similar to the SUSK system in looks, though they use a different means of generating power from the water current. This design exists as a drawing included in the patent for methods to harness hydrokinetic energy, but it does not seem that the system has been developed any further.

## 1.4 Past WPI Project Work on TUSK

At WPI there have been multiple projects that have focused on generating electricity using a kite-shaped system, both from air and water currents. The projects most applicable to ours have been those developing and improving the TUSK system. These TUSK projects designed, manufactured, and tested a scale model system constructed from 3D printed ABS plastic. The kite included an integrated turbine that was able to generate power, see Figure 3. The kite moved in a cross-current figure eight path, controlled by a user via a rudder. The kite was able to generate a significantly higher effective velocity than that of just the current. This project began as an MQP led by Professor Olinger, and was then built on by Ryan Fredette in his Masters Thesis.

These previous TUSK projects designed, manufactured, and tested a scale model system constructed from 3D printed ABS plastic. The original MQP designed a preliminary system, and then Fredette modified the design and the testing of the system. A year after that, Morar and Morozov improved on the project by modifying the controls system, as well as by implementing a 12 ft long, 0.75 in diameter tether made out of carbon fiber. For our project, we will be producing new designs while at the same time reusing some original parts from the previous years project [17, 18].

Our SUSK system is a new implementation of the current designs of TUSK systems. In the original system, the method for obtaining power from the current came in the form of a kite at the end of a tether, where the tether is fixed to a stationary point on the bottom or surface of the body of water it is in. One of the major drawbacks to this type of system is that the tether creates a very noticeable amount of drag as it sweeps through the water. To

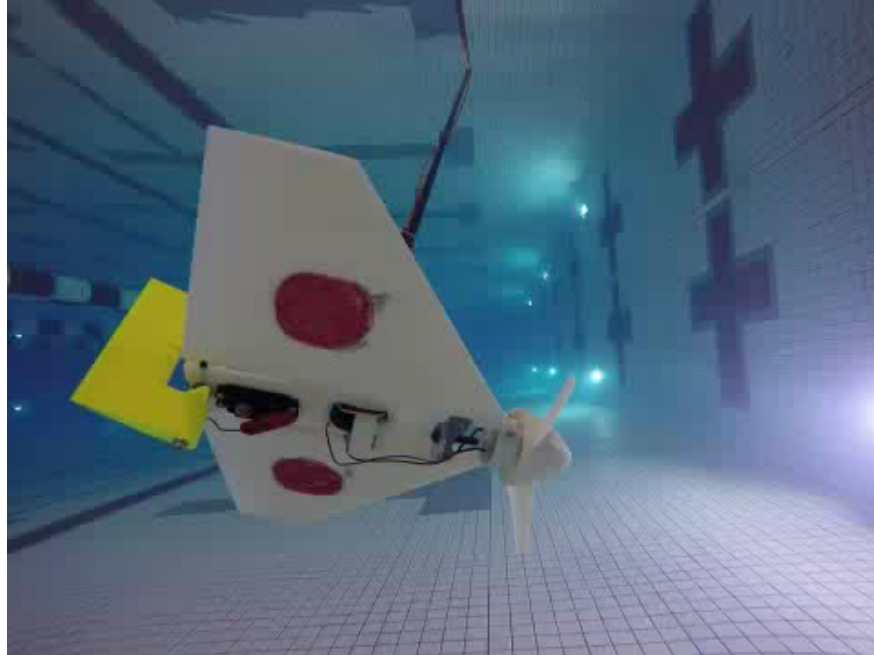


*Figure 3: A tethered undersea kite from a previous WPI MQP being tested in the WPI pool*

test this we went to the WPI swimming pool with the existing 12 ft long, 0.75 in diameter tether, submerged it, and tried to move it through the water. What we found is that at even pretty low velocities, the tether had a very noticeable drag. Professor Olinger suggested that we should try to fully remove the tether from the water, and turn the undersea kite into a surface boat, with a vertical wing underneath it for generating the cross-current movement. Every other TUSK system relies on a fully submerged kite and tether, so our project is new, and this type of power generation has not been done before.

## 1.5 Goal and Objectives

Our project goal is to create a scale-model prototype of the Surface Underwater Kite system for renewable energy generation from water currents. Our project objectives include:

1. Design a preliminary SUSK system: This included conducting tests to develop an optimal hull and wing shape, as well as creating a CAD model of the boat. The system needed to be made compatible with the existing tether and gimbal, although the control system was mostly redesigned.
2. Construct a prototype of the SUSK system: The CAD models created in the design

process were 3D printed or otherwise machined and constructed. Modifications to the gimbal and tether were made to allow for better control of the system.

3. Conduct scale model experiments with the SUSK system: The system was tested multiple times in the WPI swimming pool, as well as the 20 ft wide  $\times$  10 ft deep water flume at Alden Research Laboratory in Holden, MA.
4. Develop dynamic simulations of the SUSK system: Physics simulations developed using the Lagrangian formulation of mechanics as well as aerospace fundamentals to predict dynamic characteristics of the SUSK system, as well as estimate optimal power generation.
5. Identify opportunities for further development of the SUSK system: Based on test results, recommendations were made for future researchers for the development of SUSK systems and their applications.

# Chapter 2: Design

This chapter outlines our design process. The final design of the prototype system, along with a component-labeled computer-aided-design (CAD) rendering, is shown in Figure 4. The design features a plate style hull with a half-chord symmetric vertical wing for control. The hull attaches to the existing tether above the water line, and the turbine system extends off of the downstream side of the system.

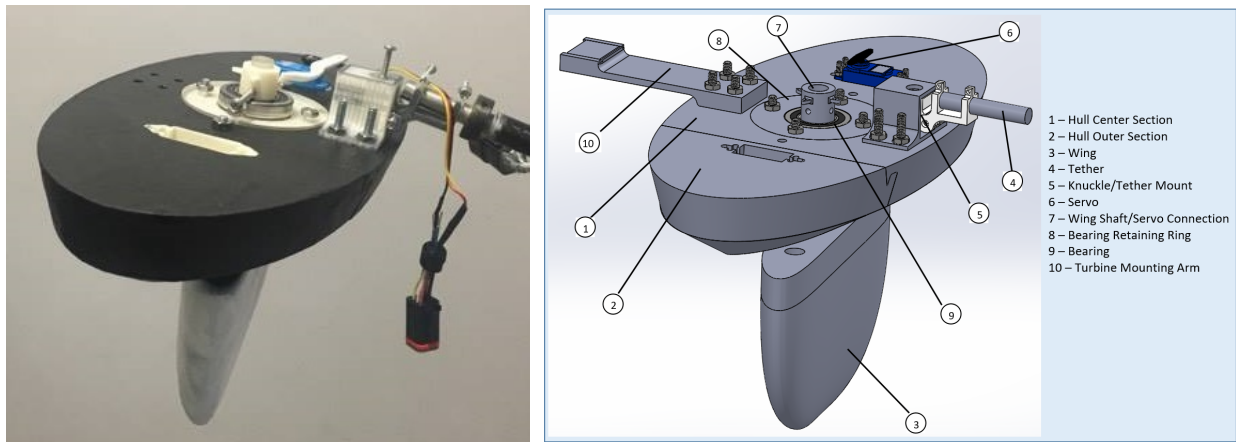


Figure 4: Final SUSK scale-model boat design and CAD rendering

## 2.1 Hull Design

Due to the orientation of the boat with respect to the current, our boat’s design required the system to be aerodynamic in more than just its chord direction. When travelling in line with the current, the relative velocity of the free-stream is parallel to the chord line of the hull. However, as the boat moves in the cross current direction, the angle between the current and the hull increases up to  $90^\circ$ . This means that our boat not only has to be aerodynamic head-on, but also sufficiently aerodynamic to current flowing against the broadside. The biggest effect from the sideways drag (which we will call perpendicular drag) is that it will create tension on the tether, and will put stress on the connection point of the boat and the tether. As a result, the hull needs to be shaped to minimized drag in the direction of travel, which slows the boat, and in the perpendicular direction, which stresses the tether. This requires a relative trade-off between characteristics in the two main directions that flow will

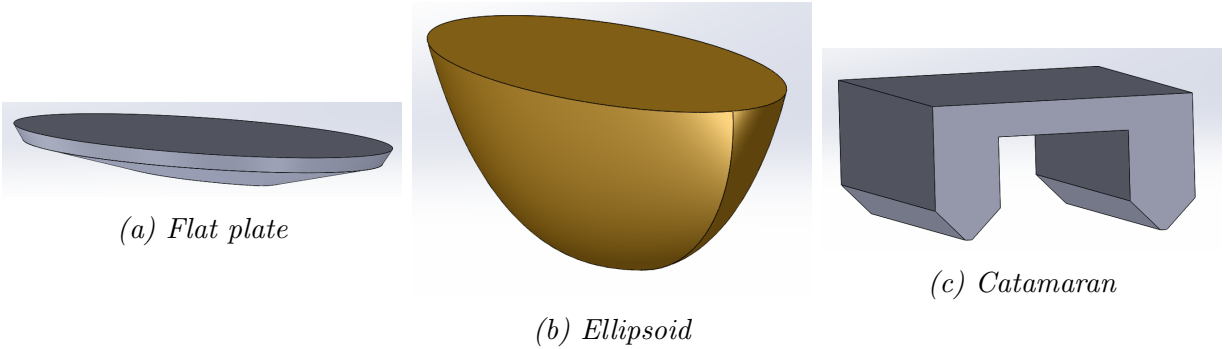


Figure 5: CAD renderings of candidate boat hull designs

hit the hull. To maximize the cross-current velocity of the system we must minimize overall drag.

The stability of the system is another concern. The tether will help keep the boat stable, but if the boat had a tendency to capsize, it would cause issues even with the help of the tether. A very thin kayak-styled boat would be very stable in its direction of travel, but in the sideways direction it would tend to roll, especially with a vertical wing attached to the bottom on it producing torque. The only way a very thin boat system would work is by having a pontoon, or similar buoyant device attached to the boat, which might have its own drag issues of its own.

With these constraints in mind, we came up with three basic designs for the boat shape: A half ellipsoid, a rounded flat plate (horizontal), and a catamaran-styled boat. Renderings of each preliminary design are shown in Figure 5. Each has its pros and cons as seen in Table 1, so we performed tests with 3D printed scale models in a water tunnel and in WPI’s pool to see what types of drag and stability each hull style has.

To test the three main hull shapes, we decided to use the small water tunnel located in Higgins Labs. We set up a wooden jig to hold a string attached to a spring, which is then attached to each of the boat hull types. Our intention was to measure the small displacement of the boat and spring in order to use Hookes Law to determine the force the water had on the boat. In doing the first few tests, the flat plate and ellipsoid hulls did not create enough drag to make the spring displace at all, even though the spring we chose was a fairly loose spring. In the catamaran test, the spring may have displaced a slight amount, but not nearly

enough to be accurate and measurable. Another issue we ran into in the catamaran test was that the weight of the spring was enough to make the hull oscillate forwards and backwards. This phenomenon seemed to be caused by the weight force of the spring being larger than the drag force on the boat, until it hits a point where the drag force overcomes the weight force.

In terms of stability, the half ellipsoid is the least stable, then the flat plate, then the catamaran is the most stable (thanks to its two chord lengths in the water). For parallel drag, we hypothesize the three to be fairly similar to each other. As for perpendicular drag, the flat plate will have the least, then the half ellipsoid, and then the catamaran.

*Table 1: Comparison of pros and cons of candidate SUSK hull designs.*

	Flat Plate	Ellipsoid	Catamaran
Pros	Simple, Stable	Common shape in aquatic craft	Stable
Cons	Low volume (low buoyant range)	Unstable, Hard to Mount Components	Complicated Design

## 2.2 Airfoil Design

### 2.2.1 Overall Considerations

#### Lift and Drag

What makes the SUSK system more efficient than a stationary turbine? The power produced by a turbine is limited by the speed of fluid passing through it. Increasing the fluid speed increases the turbine power generation. In our system, a vertical airfoil on the bottom of the boat causes it to traverse in the cross-current direction. The turbine mounted on the boat therefore experiences an increased apparent fluid velocity that is the vector sum of the velocities of the fluid current and the boat  $\mathbf{V}_{app} = \mathbf{V}_{current} - \mathbf{V}_{boat}$ .

To qualitatively understand the optimal design parameters, consider the following three cases shown in Figure 6:

1. The system is partway through its transit and has accrued some speed. The drag of

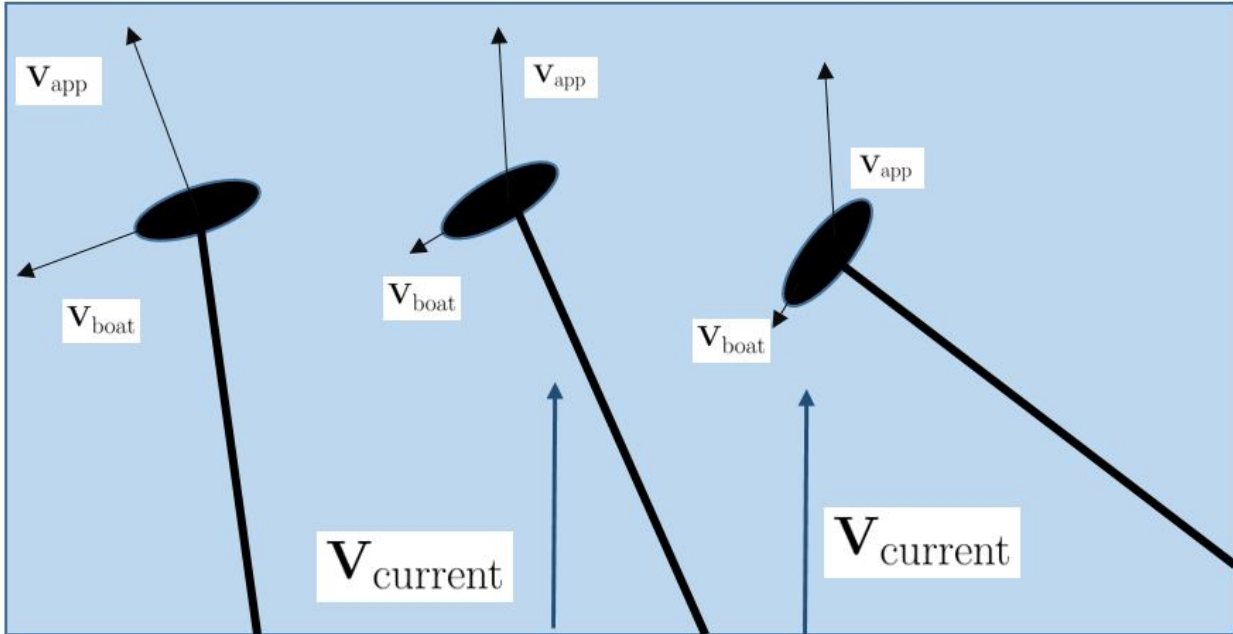


Figure 6: Different cases for movement of the SUSK boat

the boats hull and airfoil act to slow it down, while the lift of the airfoil acts to speed it up.

2. The system has completed its arcing path to one side at a low angle and must change directions. All three forces, the drag of the airfoil and hull, along with the lift of the airfoil, act to reverse the direction.
3. The system has completed its arcing path to one side at a high angle and must change directions. Now, only the drag of the airfoil and hull act in the desired direction of movement. The lift at high angles is perpendicular to the desired direction of motion and contributes little.

For the purposes of airfoil design, we consider the lift and drag of the airfoil to be variable. In the first case, we clearly want to maximize the lift while minimizing the drag. The second case is somewhat counter-intuitive; both a high lift and drag will aid in reversing direction. In the third case, the lift is negligibly beneficial, but maximizing the drag will quickly reverse the boats direction. A more detailed analysis of the effect of the lift and drag is given in Chapter 5.

This creates a trade-off. A high lift is optimal in all three cases, but our preference on



drag depends on the situation. In case one we want a low drag, but in cases two and three, a high drag is preferred.

We resolve this by taking our control over the airfoils position into account. In the event that a high drag would be beneficial, the airfoil can be turned sideways and used as a sail. Therefore, high drag is not a parameter we need to design into our airfoil. Instead we can focus on low drag and high lift. That is to say, we can use our control of the airfoil to achieve high drag whenever it is beneficial, but low drag and high lift are more difficult to achieve parameters that must be engineered into the airfoil itself. The importance of lift versus the lift to drag ratio is dependent on the other parameters of the boat, such as the hull drag, and are calculated in section 2.1.

### Symmetry

The nature of the boats movement introduces a constraint on airfoil design. Since the boat ideally moves and generates power in both directions of travel, the airfoil must exhibit some degree of symmetry. This can either be symmetry about the chord line, such as the NACA 00 series, or symmetry about the half-chord line.

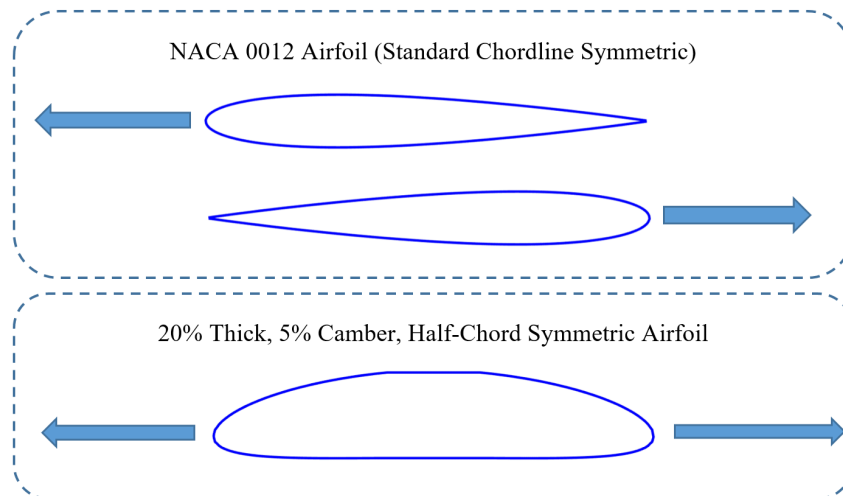


*Figure 7: A comparison of the reversible movement allowed by chord line and half-chord symmetric airfoils, demonstrating the necessary rotation control.*

Chord line symmetric foils are well studied and known to work, whereas research on half-chord symmetric foils is limited. However, half-chord symmetric airfoils provide an energy saving advantage in this particular application. When the boat reverses direction, a chord

line symmetric airfoil would need to rotate approximately one half revolution before it could propel the boat in the opposite direction, whereas a half-chord symmetric airfoils do not. This difference is displayed in Figure 7. This rotation is wasteful in both time and energy, so if a half-chord symmetric airfoil can be designed to provide lift and drag properties equivalent or exceeding those of a chord line symmetric airfoil, it would be far preferable.

## 2.2.2 XFLR5 Simulations

To answer the question of half-chord symmetric airfoils, we conducted simulations in XFLR5, an application of the Xfoil vortex panel method [19]. The front half of half-chord symmetric simulation airfoil files were generated in the program and symmetrically reflected with a custom MATLAB script before being reloaded into the program and tested. Twelve half-chord symmetric airfoils, shown in Figure 8, were simulated, ranging from thicknesses of 10% to 20% the chord length, and with cambers from 2% to 5% the chord length. We simulated Reynolds numbers of 150,000, 250,000, and 350,000, and angles of attack from  $0^\circ$  to  $18^\circ$ . Two NACA airfoils, the 0012 and the 0016 were also tested so a comparison could be made.

Since the airfoil is controlled by a servo, the optimal angle of attack can be chosen for each at any given point in the boats transit. Therefore, the half-chord symmetric airfoils were compared to each other and to NACA airfoils for each Reynolds number at the angle of attack which gave each airfoil its optimal coefficients of lift and drag. We made this comparison for both the angles of attack of maximum lift and the maximum ratio of lift to drag.

According to simulation testing, half-chord symmetric foils provided comparable and preferable properties to chord line symmetric foils. When compared at the angles of attack corresponding to the maximum ratio of lift to drag, 4% camber half-chord symmetric foils have a higher ratio of lift to drag ( $\sim 17\%$ ) and higher lift ( $\sim 19\%$ ) than chord line NACA 00 series symmetric foils of comparable thickness. Similarly, when compared at the angles of attack corresponding to the maximum lift coefficient, 2% camber half-chord symmetric foils have a higher ratio of lift to drag ( $\sim 11\%$ ) and only negligibly lower lift ( $\sim 0.5\%$ ) than chord line NACA 00 series symmetric foils of comparable thickness. This confirmed that half-chord

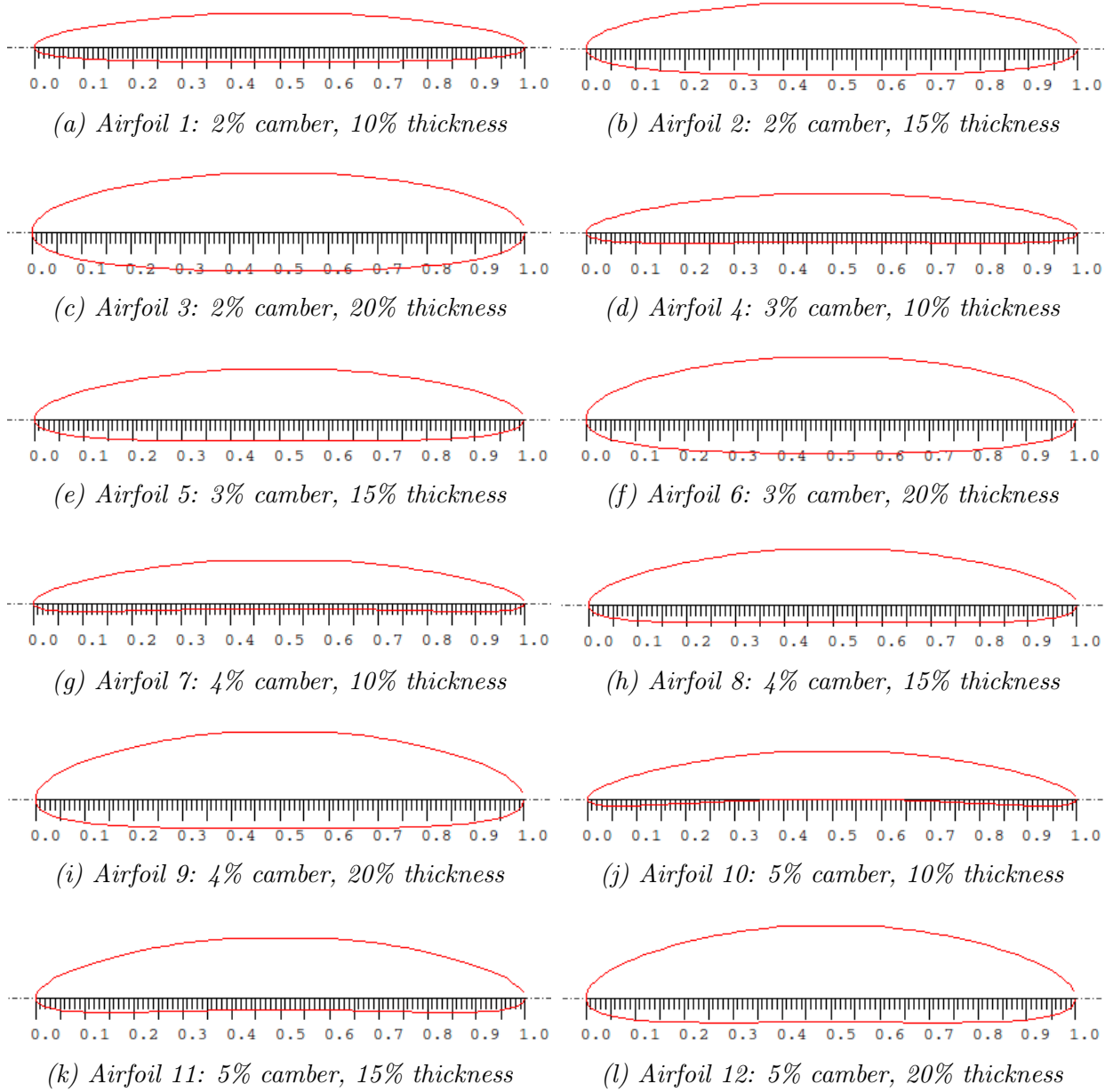


Figure 8: Airfoils for testing in XFLR5.

symmetric airfoils can be used in place of the NACA 00 series chord line symmetric airfoils, saving energy in the control of the airfoil.

Additionally, the following rough trends emerged among half-chord symmetric airfoils.

1. When compared at the angle of attack of maximum lift to drag:

The ratio of lift to drag decreases as foils become thicker ( $\sim 2\%$  of chord length) and increases as the foils becomes more cambered ( $\sim 10\%$  of chord length).

The coefficient of lift increases as foils become thicker ( $\sim 4\%$  of chord length) and more cambered ( $\sim 10\%$  of chord length).

2. When compared at the angle of attack of maximum lift:

The ratio of lift to drag decreases as foils become thicker ( $\sim 3\%$  of chord length) and more cambered ( $\sim 10\%$  of chord length).

The coefficient of lift increases as foils become thicker ( $\sim 0.8\%$  of chord length) and more cambered ( $\sim 4\%$  of chord length).

### 2.2.3 Force Analysis

Final selection of the airfoil was achieved by calculating the net force on the boat in the direction of motion. The simplified setup for this calculation is shown in Figure 9 The net forces on the boat in the direction of motion, minus the drag of the turbine, can be found as a function of boat speed and position as

$$F_b = L_w ||\hat{\mathbf{V}}_{\text{eff}} \times \hat{\mathbf{b}}|| + D_w (\hat{\mathbf{V}}_{\text{eff}} \cdot \hat{\mathbf{b}}) + D_b \quad (2.1)$$

where,

$$\begin{aligned} \text{Lift of the wing:} & \quad L_w = C_{L,w} q_c h \\ \text{Drag of the wing:} & \quad D_w = C_{D,w} q_c h \\ \text{Drag of the boat:} & \quad D_b = C_{D,b} q_b A \\ \text{Effective current velocity:} & \quad \mathbf{V}_{\text{eff}} = V_c \cos(\theta) \hat{\mathbf{r}} - (V_b + V_c \sin(\theta)) \hat{\mathbf{b}} \\ \text{Dynamic pressure:} & \quad q = \frac{1}{2} \rho V_{\text{eff}}^2 \\ \text{Dynamic pressure in } \hat{\mathbf{b}}: & \quad q_b = \frac{1}{2} \rho (\mathbf{V}_{\text{eff}} \cdot \hat{\mathbf{b}})^2 \end{aligned} \quad (2.2)$$

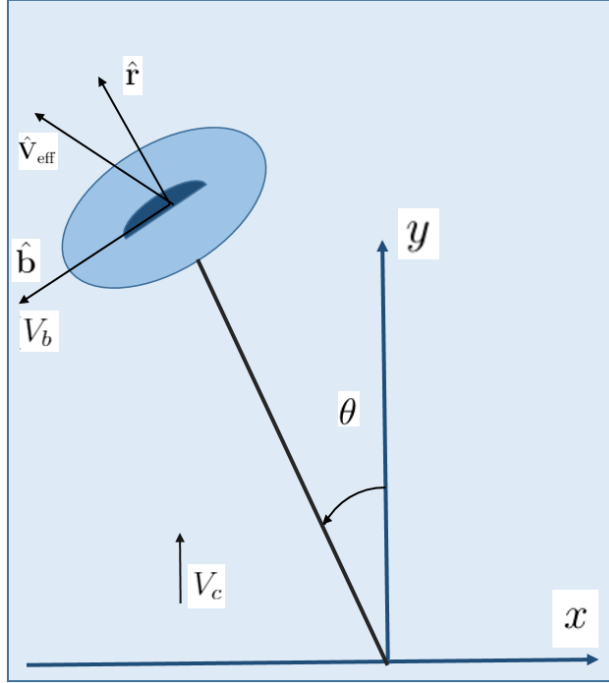


Figure 9: Diagram showing the relevant directions and quantities used in the force analysis.

and  $h$  represents the half-span of the wing. This net forward acting force accelerates the boat, leading to greater speeds and higher power generation.

Coefficients of lift and drag were chosen from the maximum coefficient of lift and maximum lift to drag ratio. Speed of the current was taken to be  $0.5 \frac{\text{m}}{\text{s}}$  with a boat speed of  $1.5 \frac{\text{m}}{\text{s}}$  at the zero angle. The chord length and half-span of the wing were taken as 0.3 m. The hull drag coefficient was approximated as that of a sphere, 0.4, with a front-facing area of  $0.0133 \text{ m}^2$ .

## 2.2.4 Force Analysis Results

Force analysis results were compared for airfoils at maximum lift and maximum lift to drag. In both cases, airfoil 12 provided the maximum force. Airfoil 12, the thickest and most cambered airfoil, produced approximately 30% more net forward force than airfoil 1, the thinnest and least cambered airfoil.

We therefore chose to print this airfoil, along with two other similar airfoils, decreasing the thickness of one to 10%, and decreasing the camber of the other to 2%, for prototyping. This allowed us to verify the validity of our force analysis. Future studies can look into

Table 2: Force (in Newtons) produced in the direction of motion by various cambers and thicknesses at maximum lift coefficient.

		Camber			
		2%	3%	4%	5%
Thickness	10%	39.627	42.407	45.115	49.998
	15%	43.524	46.255	47.947	50.998
	20%	46.975	48.375	49.771	51.204

Table 3: Force (in Newtons) produced in the direction of motion by various cambers and thicknesses at maximum lift to drag ratio.

		Camber			
		2%	3%	4%	5%
Thickness	10%	22.447	19.066	22.481	24.546
	15%	21.337	24.934	27.555	29.690
	20%	27.947	31.295	32.065	35.834

further optimizing the shape and size of the airfoil.

## 2.2.5 Wind Tunnel Testing

Airfoils 3, 10, and 12 were 3D printed for testing in the WPI 8 in  $\times$  by 8 in low-speed wind tunnel. A SolidWorks airfoil template from in WPI’s AE 3711 Aerodynamics class was used in the 3D printing process. This template allowed for easy mounting onto hardware in the wind tunnel. Airfoil 12 was determined by force analysis to be the optimal half-chord symmetric airfoil, with a thickness and camber of 20% and 5% the chord length respectively. Airfoils 3 and 10 were variations on this foil. Airfoil 10 had a decreased thickness 10% the chord length, and airfoil 3 had a decreased camber of 2% the chord length. This allowed us to verify the trends of our force analysis. Future studies can look into further optimizing the shape and size of the airfoil.

Each airfoil was tested at a chord Reynolds number of 350,000 for its lift and drag forces, varying the angle of attack from 0 to 18 degrees. A force balance connected to the wing measured the axial and normal forces as a function of the angle of attack.

We converted axial and normal force data from the wind tunnel to lift and drag coefficients and plotted them against the XFLR5 simulations results as a function of angle of attack.

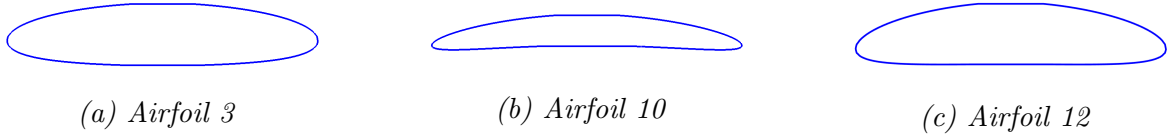


*Figure 10: Three candidate airfoils printed for testing in the wind tunnel*

Drag results were inconclusive, likely due to small magnitude of the drag and induced vortices from the wind tunnel enclosure. Lift results roughly correspond with simulation results, shown in Figure 12.

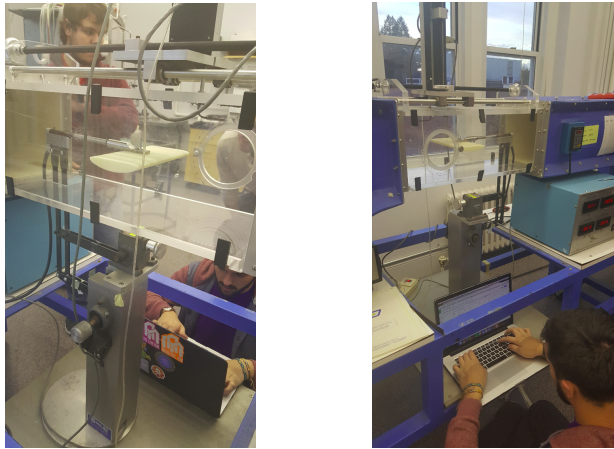
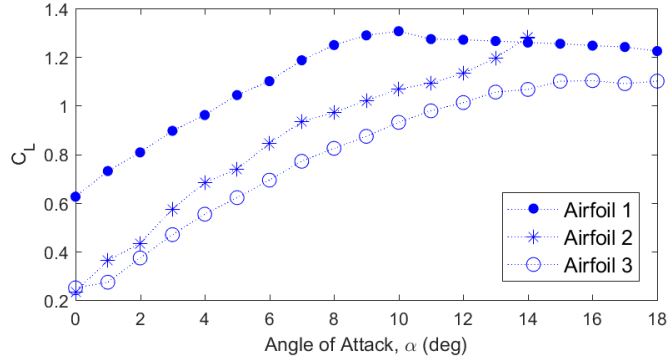
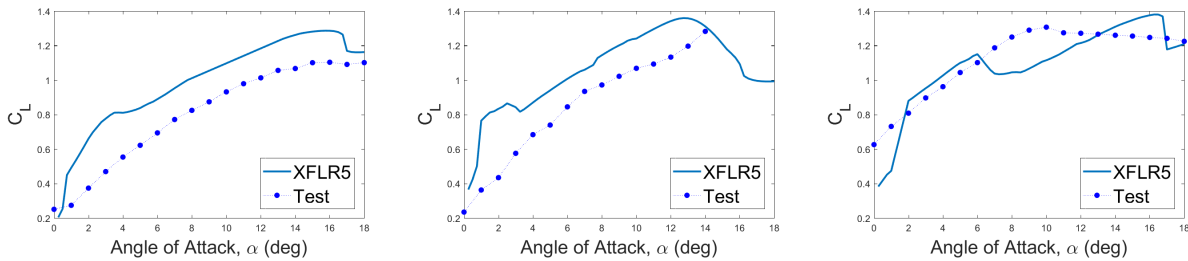


*Figure 11: Testing of the optimal airfoil and two variations inside the WPI wind tunnel.*

The maximum lift coefficient for the optimal foil was experimentally found to be 1.306, within 5% of the expected value of 1.369. However, the corresponding peak occurs at 10 rather than 16 degrees. The maximum lift coefficients of the thinner (10% chord line thickness) and reduced camber (2% chord line camber) are 1.282 and 1.103, respectively. The thinner foil matches the simulation closely, while the less cambered wind under-performs by approximately 25%. Note that we only tested the thinner foil up to an angle of attack of  $14^\circ$  due to significant shaking in the wind tunnel. The tests confirm the optimal foil and confirm the expected trends of increasing lift with increasing thickness and camber. Complete wind tunnel test results can be found in Appendix A.



(a) Wind Tunnel test results for all airfoils



(b) Airfoil 3 - Simulation versus wind tunnel results

(c) Airfoil 10 - Simulation versus wind tunnel results

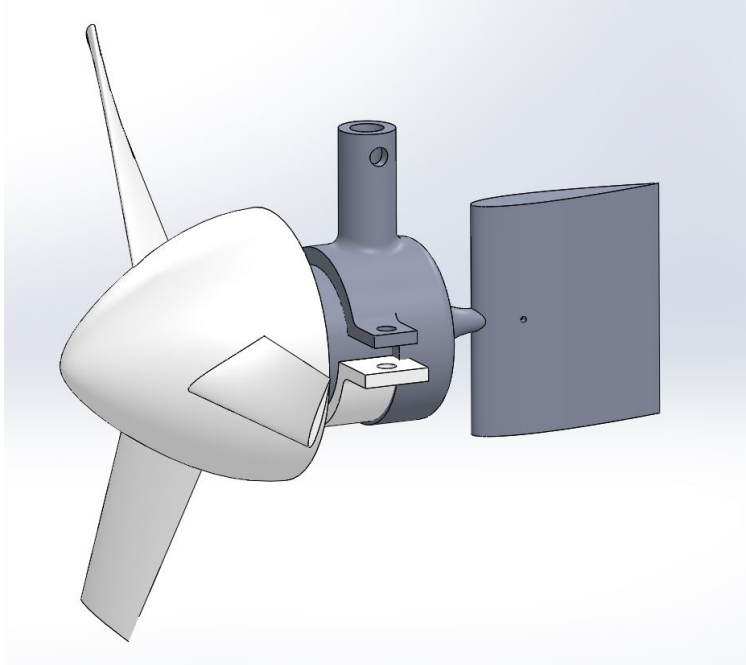
(d) Airfoil 12 - Simulation versus wind tunnel results

Figure 12: XFLR5 simulation and wind tunnel test results for candidate airfoils.

## 2.3 Turbine Design

In order to generate power, the SUSK prototype will utilize a turbine similar to the TUSK system that we are adapting. The power generation system consists of a turbine blade mounted to a small generator. This turbine is mounted on a shaft that is held off of the downstream side of the SUSK system. This shaft is free-rotating, allowing the turbine to point in the direction of highest flow and swivel back and forth as the SUSK travels back and forth cross-current. To assist in turning the turbine in the direction of the flow, a small vertical wing is positioned behind the turbine, similar to a weathervane. We used a NACA 0015 airfoil for the vertical wing on the turbine assembly due to its symmetry producing no moment at a zero angle of attack. A photo of the assembly can be seen in Figure 13. The turbine airfoil and generator model were first designed and selected by Ryan Fredette in his M.S. Thesis and were utilized for the SUSK system [17].





*Figure 13: CAD Rendering of turbine assembly showing the turbine airfoil along with an airfoil to correct its direction*

## 2.4 Other Design Considerations

### 2.4.1 Buoyancy and Stability

To function properly, the boat must remain submerged at an appropriate height. To reduce drag, the tether must remain out of the water. To maintain stability and generate power, the wing must remain completely submerged. Ideally, the surface of the boat should also remain above that water whenever possible to protect electronic components.

The buoyant force acting on the boat can be approximated through Archimedes principle as the weight of the water displaced. Assuming steady-state conditions, the water line can be approximated from the weight, density, and geometry of the boat. The boat does not have a homogeneous density even though the wing and the lower hull are primarily printed out of ABS plastic. The 3D printer uses a variable density, applying greater density to the the outer surface and load bearing sections. To approximate the density of these parts, they were assumed to be a solid shell of solid density and 0.05 in thickness and an inner low

Table 4: Surface Area, Volume, and resultant Mass of SUSK Components

Component	Surface Area (in <sup>2</sup> )	Volume (in <sup>3</sup> )	Weight (lb)
Boat Outer Section (x2)	120.68	56.39	0.747
Boat Center	211.11	62.94	0.4791
Wing Body	135.20	73.13	0.467
Torque Transmitter	17.02	1.51	0.0212
Turbine Arm	30.05	3.06	0.0394
Tether Mount Components	Weight Estimate (Different Material)		0.5
Other Turbine Components	Weight Estimate		0.75
Acrylic Shaft	Not Relevant	1.92	0.08
Acrylic Seal	Not Relevant	5.65	0.24
Lager Bolts (x12)	Component Weight Measured Directly		1.15
Larger Nuts (x12)	Component Weight Measured Directly		
Smaller Bolts (x7)	Component Weight Measured Directly		
Smaller Nuts (x7)	Component Weight Measured Directly		
Servo (x2)	Component Weight Measured Directly		
Larger Bearing (x2)	Component Weight Measured Directly		
Smaller Bearing	Component Weight Measured Directly		
Total			

density portion. From test sample 3D printed blocks, it was calculated that the density of the solid portion was  $0.0387 \frac{\text{lb}}{\text{in}^3}$  and that the density of the low density interior was  $0.00488 \frac{\text{lb}}{\text{in}^3}$ .

We need the weight of the boat to be between the buoyant force that would be supplied with only the wing submerged and the buoyant force that would be supplied with the wing and full hull submerged. Table 4 gives weights of the SUSK's components. The 3D printed components' weights are estimated using

$$W = SA t \rho_s + (V - SA t) \rho_\ell \quad (2.3)$$

with part surface area  $SA$  and volume  $V$  given by the SolidWorks files, and thickness  $t$ , solid density  $\rho_s$ , and low density  $\rho_\ell$  estimated above. An estimate of the total weight, as calculated in the table, is 4.47 lb. From Archimedes Principle, for the hull to be partially submerged, it is required that

$$\rho_w V_{\text{wing}} \leq W_{\text{boat}} \leq \rho_w (V_{\text{wing}} + V_{\text{hull}}) \quad (2.4)$$

where  $\rho_w$  is the density of water, and  $V_{\text{wing}}$  and  $V_{\text{hull}}$  are the volumes of the wing and hull respectively. With  $\rho_w = 0.0361 \frac{\text{lb}}{\text{in}^3}$  and data from Table 4, the inequality becomes

$$2.64 \text{ lb} \leq W_{\text{boat}} \leq 6.95 \text{ lb} \quad (2.5)$$

which is confirmed from Table 4.

To assess the buoyancy and stability of the final system, the final assembly was submerged and tested in a large water tank. The system had tendency to roll, but it was stable when supported by the tether connection. Buoyancy was achieved as expected for the system prior to first tests, but as additional components were added, the weight of the boat began to approach the upper limit. The results of this issue will be discussed more in Section 4.3.

### 2.4.2 Water Absorption

In addition to the short term buoyancy and reaction to perturbations, the boat was also tested for water absorption. Due to the porous nature of the 3D printed plastic, the absorption of water poses a notable threat to the long-term buoyancy of the system. In order to perform consistent and controlled tests of the final system, a time-invariant density is desired.

To test for water absorption and retention, a sample of the 3D printed material was coated with rubberized sealant. The sample was weighed and partially submerged for 30 minutes. The sample was then removed from the water and weighed again. The process was repeated with an untreated, but otherwise identical sample. Results showed that while the untreated sample gained mass over time, the treated sample did not, leading to the use of the same rubberized sealant on the majority of 3D print materials.

# Chapter 3: Fabrication

---

## 3.1 General System Overview

All of the parts of the SUSK system were modeled using the CAD program SolidWorks. The design process was iterative and modified to meet the tolerances of 3D printing. The majority of the boat was 3D printed out of ABS plastic. Some CAD models from the previous years TUSK project were also used in order to create a compatible tether interface with already existing parts.

Based on the results, a flat plate was chosen for the primary hull and the airfoil was based off of the optimal half-chord symmetric airfoil, airfoil 12. A hanging turbine was added to test the actual power generation profile, and a new control box was created to manually control the wing, monitor power generation, and record tether orientation.

After completing design tests, a finalized design was constructed. Our SUSK system consists of five main subsystems: the main body, tether connection, gimbal, control box, and the turbine. This system can be seen in the figure below. In the upcoming sections, each of these subsystems will be discussed on how they were designed.

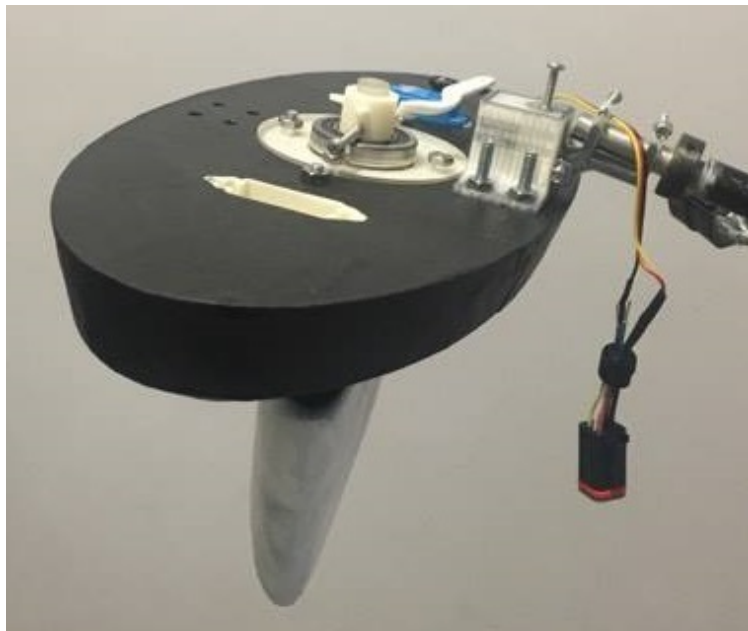


*Figure 14: Assembled scale-model SUSK system*

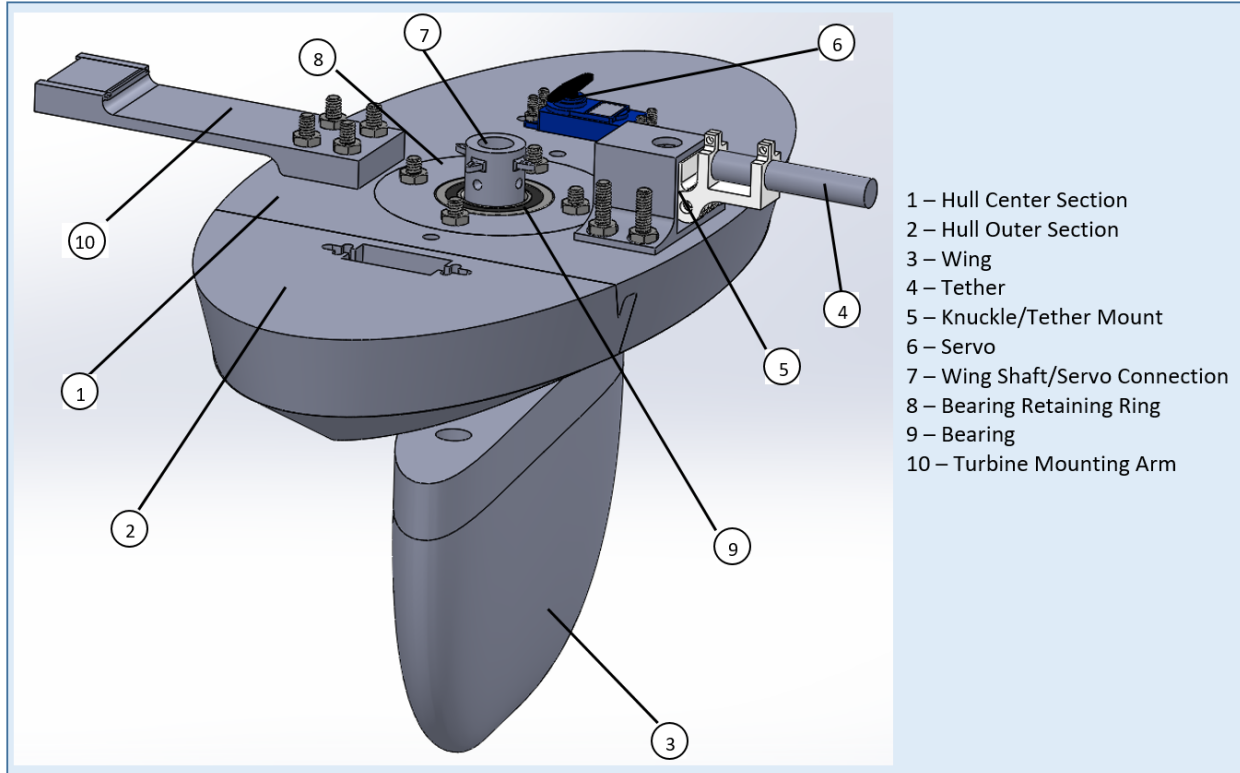


Figure 15: CAD Rendering of final SUSK system

## 3.2 Main Body

The main body of the SUSK system consisted of the hull and the wing. As previously mentioned, the flat plate design was chosen for the primary hull. From the design and stability results, the flat plate proved to be overall more stable than the other two original designs, the ellipsoid and catamaran-styled boat. Due to constraints of the printer and in order to prevent a split in the shaft hole, the hull was split and 3D printed into three parts, as can be seen in the figure below.

The boat, as well as the wing, were 3D printed out of ABS plastic. The wing shaft bearing support and wing shaft were machined from acrylic to provide additional strength.

The wing shaft/servo connection was fixed onto the main body with a sealed bearing, as well as an additional bearing retaining ring. Machine screws and nuts were used to fix the bearing retaining ring onto the main body of the boat.

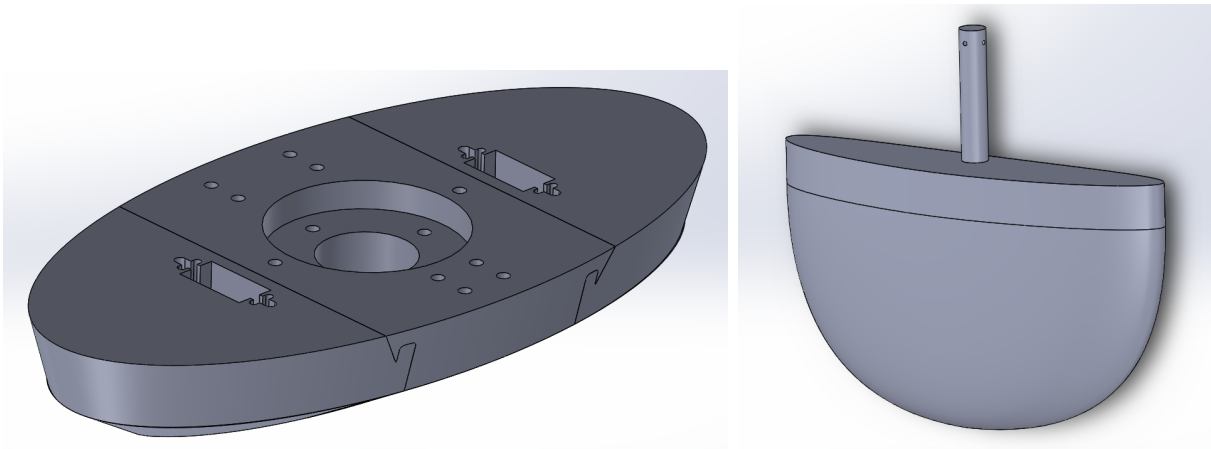
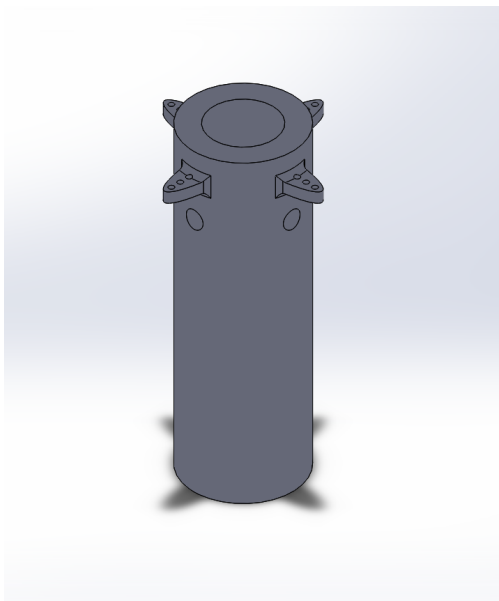
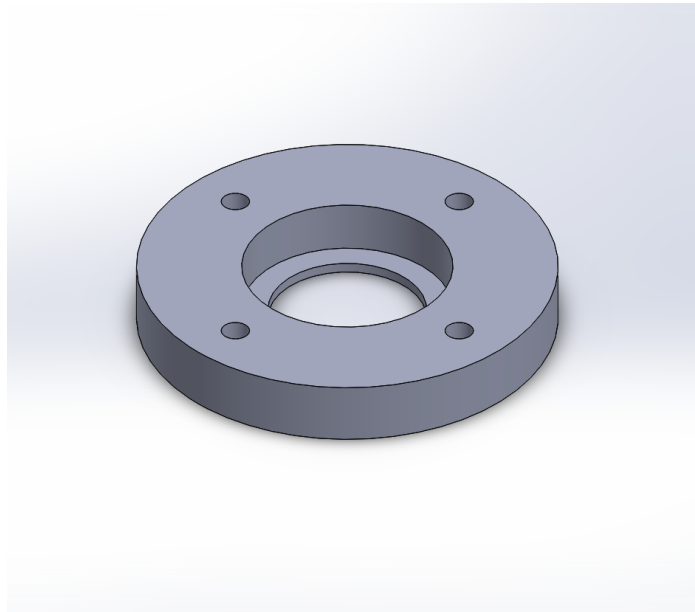


*Figure 16: Main Body Design and Wing with Shaft*



*(a) Wing Shaft/Servo Connection*



*(b) Bearing Retaining Ring*

*Figure 17: Wing Shaft and Seal*

### 3.2.1 Water Proofing

Based on the results of the waterproofing and buoyancy tests, the 3D printed hull and wing were treated with a sealant. A black sealant was chosen for visibility against a white pool background. A waterproof servo and waterproof wire connectors were installed, along with a splash resistant turbine slip ring. These are used in order to ensure that the system will not fail when exposed to water,



*Figure 18: Applying rubberized sealant to the wing*

### 3.3 Tether Connection

One of the few things from the previous projects that was reused was the 12 ft long, 0.75 in diameter tether made out of carbon fiber. However, because the SUSK system involves a whole new main body, it required a design of a new tether mount along with new joints or “knuckles.” The tether and the main connector to the hull are shown in Figures 19 and 20, respectively.

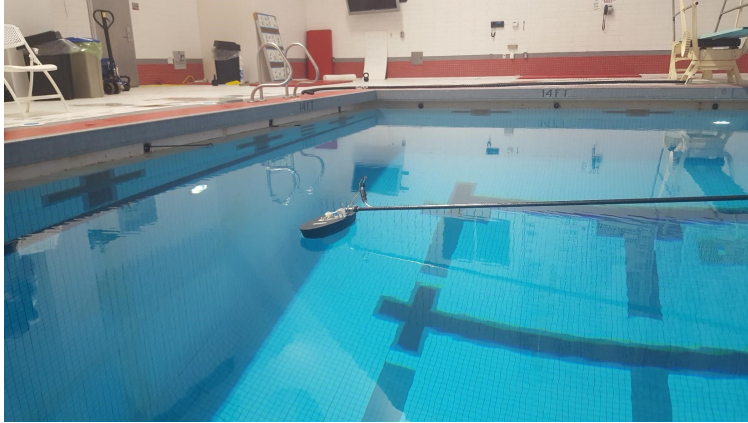


*Figure 19: Tether attached to the SUSK system in the pool.*

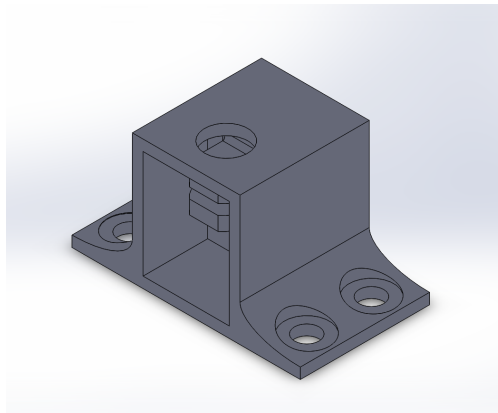
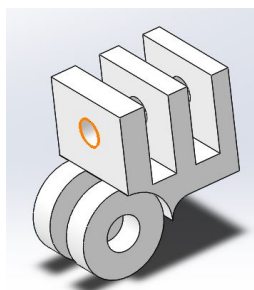
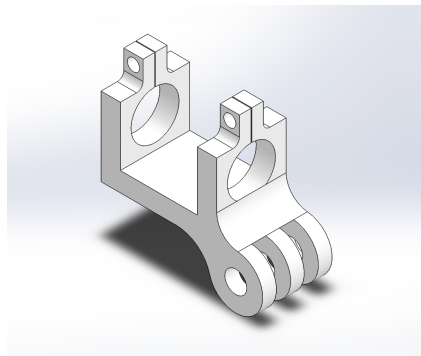


*Figure 20: Tether mount*



*(a) Knuckle*



*(b) Rod Holder*

*Figure 21: Tether Joint and Holder*



The knuckle and rod holder, shown in Figure 21, were designed to connect the tether onto the tether mount. The attachment knuckles were printed from nylon reinforced with carbon fiber after previous iterations made with ABS plastic broke. Screws and nuts were used to tighten the hinges.

### 3.4 Gimbal and Control Box

The tether and boat are connected to a 3-axis gimbal, which also serves as a connection between the control box and the tether. The mechanical structure and potentiometers of the gimbal are reused from the earlier TUSK project, but with a few modifications and simplifications in wiring in order to improve reliability.

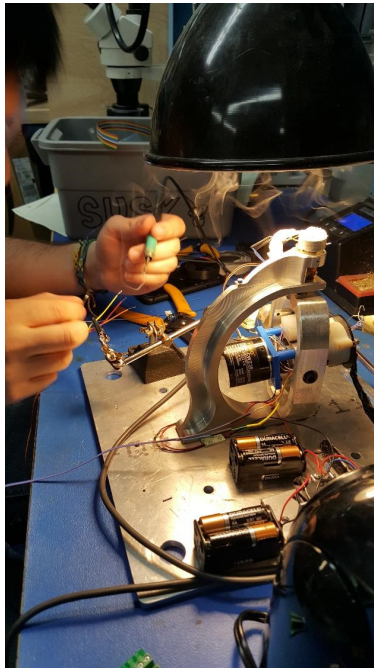


*Figure 22: Rewiring of the Gimbal*

The TUSK system was controlled by a joystick on an external control box, connected with two VGA cables. One of the cables returned rotation data from a rotary encoder, and the other returned potentiometer data and servo control signals. The wiring in the old control box was very clunky and confusing, and the wiring allowed for a lot of shorts. Having the two cables coming from the box also made the controller harder to use, and each of them were soldered directly to the box, as opposed to a VGA breakout port.

Ultimately it was decided to create a completely new control system, one that was simpler in wiring, and easier to use. This control box, as seen in Figure 23, contains an Arduino Due, a battery pack, a small perfboard with wiring for a button circuit, a microSD breakout board, and a VGA breakout. The wiring for the new control box is color coded, and documented in a wiring table seen in Appendix B. Instead of soldering cable wires into the box, a VGA breakout was used to allow for the cable to be detached. While the control box was being created, the old gimbal needed to be optimized. The wiring was very disorganized, with many frayed and severed connections, and loose connections in the slip ring. The old gimbal wiring was beyond feasible repair, so it needed to be recreated. Ribbon cables and adhesive tape were used for cable management, all with color coding. Instead of cutting the VGA cable like the last project, another VGA breakout board was used to allow the system to be broken up into three parts for ease of use: the gimbal, the control box, and the VGA cable. A progress photo of the rewiring process can be seen in Figure 22, and the finished gimbal can be seen in Figure 23.

The control box has a few basic functions: Use push buttons to move a servo clockwise and counterclockwise, read potentiometer data from the gimbal, and read voltages from the turbine. The code on the Arduino Due takes the potentiometer readings, servo angle, and turbine voltage, and outputs it into a .csv file. The code on the Arduino Due can be seen in Appendix C. The two potentiometers are set up on two different rotations on the gimbal, each measuring a voltage that can be converted into an angle. The top mounted potentiometer, labeled  $q_2$ , and the side mounted potentiometer labelled  $q_1$  allow a complete description of the location of the end of the tether. The variable naming convention will be discussed further in Chapter 5. The rotary encoder on the gimbal gives the last degree of rotation, but since the SUSK does not need to have the tether rotate, the wiring was left out of this system, but is easily integrated to work with the new control box.

The new control box was specifically designed to work with the TUSK system, so that the TUSK can be hooked up and controlled with the same control box without issue.

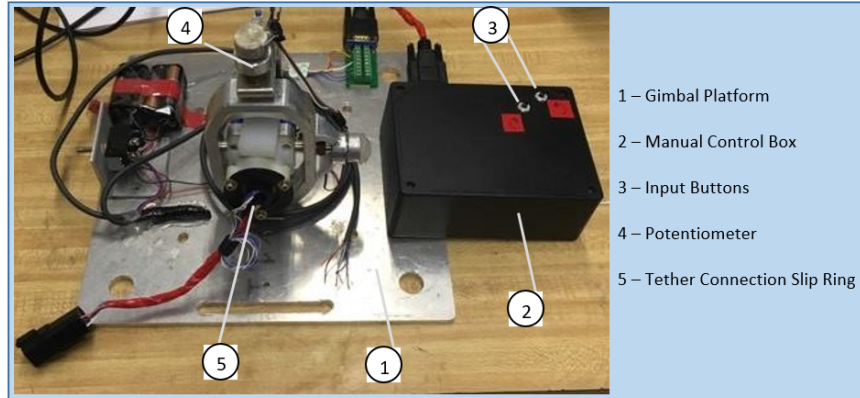
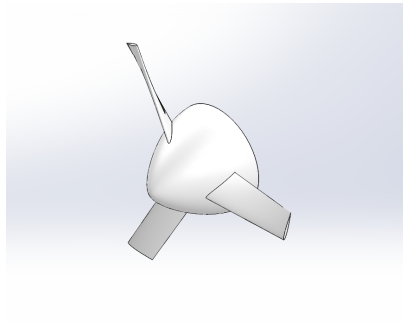


Figure 23: The control box for the SUSK system with components detailed.

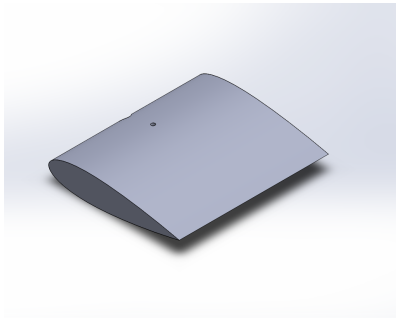
### 3.5 Turbine Assembly

As mentioned in Section 2.3, the turbine airfoil used for the SUSK system was designed by Ryan Fredette. An extra 3D printed part was available in old TUSK materials, shown in Figure 24a, so the remaining parts of the turbine assembly, shown in Figures 24b and 24c were printed to be compatible with it.

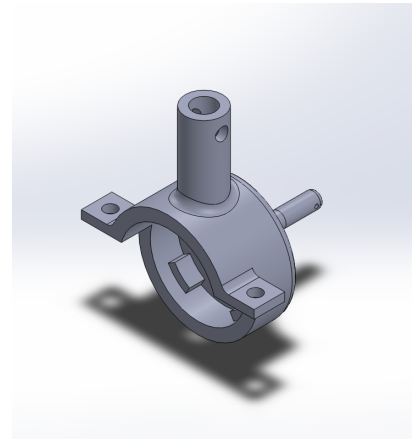
A turbine arm made out of acrylic was used to connect the turbine assembly and slip ring onto the main body of the SUSK system. Similarly, a small wooden shaft was used to attach the slip ring and the turbine wiring. This was done by drilling a small hole through the wooden shaft to hide and connect the wires from the slip ring onto the turbine generator. When we got the turbine to function, we covered the wooden shaft with a small, carbon fibered tube to protect from any water damage. To couple the turbine airfoil to the generator within the assembly, the pin on the turbine was fit and crimped to a drilled-out screw and threaded down to the turbine. A visual of the SUSK system with the finalized turbine assembly can be seen in Figure 25.



(a) Turbine Airfoil



(b) Airfoil



(c) Generator Holder

Figure 24: Components of the turbine assembly

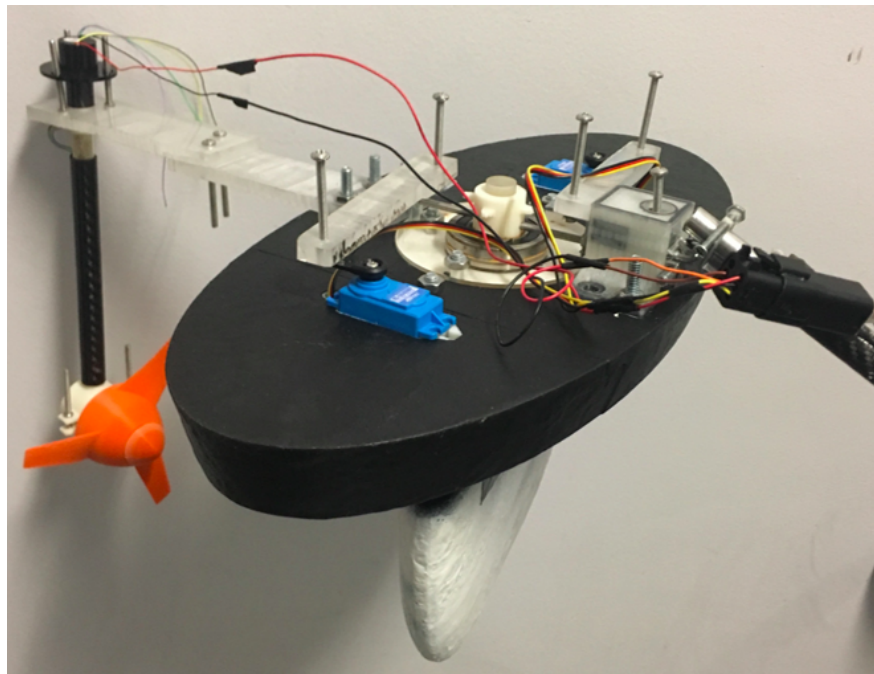


Figure 25: SUSK system with finalized turbine assembly

# Chapter 4: Testing

---

## 4.1 Water Tank Test

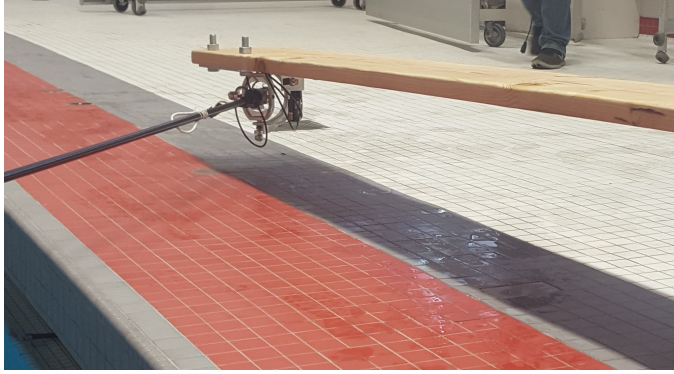
To initially test initial viability of the assembled boat, the boat was placed in a large water tank. The craft was then perturbed and pulled side-to-side to ensure stability, smooth travel, and a resistance to flipping. The boat was then pulled again side-to-side, but this time with the wing actuated to qualitatively assess the force generation of the wing, and ensure stability under actuation.

After immersion in the tank, the boat remained buoyant and stable to small perturbations. No significant weight increase was observed from water retention. The boat moved smoothly when pulled by hand across the water and experienced significant change in the force in the cross-flow direction when the wing was actuated.

## 4.2 WPI Pool Test without Turbine

To test the boat viability and control effectiveness, the boat was tested in the WPI pool. The gimbal was suspended above the water, mounted to a cart which ran alongside the pool. In this way, the cart was pulled to generate a current velocity relative to the boat and gimbal. Data logging was not yet implemented in the control system. This test was to familiarize the team with control of the system in test condition and collect qualitative data on wing effectiveness. Seven runs were conducted, varying the speed from approximately  $0.5 \frac{\text{ft}}{\text{s}}$  to  $1.5 \frac{\text{ft}}{\text{s}}$ .

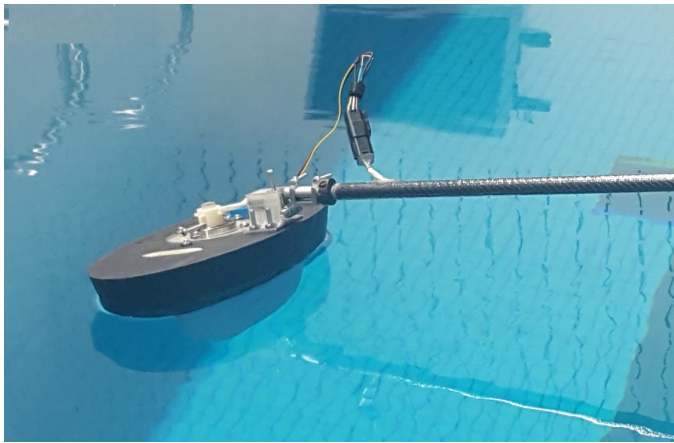
The initial pool tests proved that the system was viable and functional, and taught the team to adequately control the wing. Cross current velocities approximately 3-5 times the current velocity were achieved, however minor problems were discovered in the control system and with the gimbal. During the 4th test run along the pool, the controls became unreliable. This was attributed to friction on the wing slip ring. This ring was later adjusted to fix the problem. Additionally, as current velocity increased, the boat became more likely to flip. This flipping was later solved by reducing the gimbal range of motion. An alternative solution that was proposed was the addition of a pontoon, to compensate for wing drag.



(a) Zoomed out gimbal



(b) Zoomed in gimbal



(c) Zoomed out entire system



(d) Close up boat

Figure 26: Testing setup for initial tow-tank tests in the WPI swimming pool.

### 4.3 Tests at Alden Research Laboratory

The team and Professor Olinger went to the Alden Laboratories in Holden, MA to use their water turbine test facility. This facility has a water flume that is a 20 ft wide  $\times$  10 ft deep, and has a range of speeds from  $0 \frac{\text{ft}}{\text{s}}$  to  $3 \frac{\text{ft}}{\text{s}}$ . This allowed the SUSK to be tested at a range of speeds, and allowed for more accurate calculations of cross-current speed versus the current speed. Another benefit was the repeatability of testing, as with the same control input, a similar boat motion would output. We could then use a few trials that had consistent results and see how those compare to the simulation results for similar control inputs.

The first day of testing we just had the full SUSK system, minus the turbine assembly.

The arm that holds the turbine assembly had yet to be printed, and the specific design for how the turbine wiring and slip ring would attach was not fully decided on. The first day had some success, with the boat moving in similar ways to the pool test, and started off very responsive. However, about halfway through testing the servos were occasionally not responding to inputs while in the water, but were somewhat responsive when pulled out of the flume for inspection. The servo appeared to be overworked when the current speed was at  $1 \frac{\text{ft}}{\text{s}}$ , and would not respond. It was decided to add a second servo in the other slot, wired to move in tandem with the original.

After a few more tests, the servo became completely unresponsive, but still had holding torque (so it was still receiving power). The issue was determined to be a severed wire, specifically the servo data wire, on the SUSK-side of the MOLEX connector. This wire had broken before, and had since been repaired, so it needed to have a more permanent fix. It originally was made using solid copper wire, but this has proven too brittle to be used as a long term solution. If the system is ever quickly jarred, such as hitting a wall of the testing flume, a solid wire has more of a potential to break.

When the system was brought back to the MQP lab, the wires were swapped to stranded copper, which are far more flexible than the solid copper wires. After the new wires were attached, the system was re-tested, but failed to be responsive. Every power, ground, and servo data wire was tested at each junction, and all but servo power passed the test. The slip ring wire that had been used for power was loose or frayed internally, so the connection would sever depending on the angle that the tether wire made with the slip ring. That bad wire was replaced with a more reliable one that did not lose connection at different angles.

Once that wire was fixed, the system still did not work. After retesting all of the connections, it was determined that the original servo was actually burned out, and would not respond to any inputs. This servo was replaced with a new one, and it worked as it was intended to. After that wiring issue was fixed, the second servo was attached and wired to use the same input from the control box as the original servo. A preventative fix was also applied to the servo arm connection, as the original plastic arm was too pliable and had a risk of breaking. To fix this, two acrylic bars were created and attached to the servos and the wing rod assembly. These bars provide much more stability than the original thin plastic,

but were more difficult to attach. Modifications were added to the wing rod cap in order to accept larger screws instead of just smaller pins.

The next day had more success, and the controlling became easier with more practice. The turbine assembly was still missing, but data on the movement of the SUSK was there and good. It was noticed that the connection between the tether and the SUSK was pliable, and the joint would sag more and more the longer it was in the water. Over many tests, the screw joint would loosen, and the angle between the tether and the SUSK would more permanently change. This could be temporarily fixed by retightening the connection, but it was not a long-lasting solution. Towards the end of the testing, the connection quickly dropped in the middle of a test. The connector holding the tether to the SUSK had a part that was not thick enough to be carbon-fiber reinforced, and had broken.

There was a day gap between testing, so a new piece needed to be created to replace the broken one. The team decided to use a harder and less pliable material for the replacement, which ended up being aluminum. This meant that a modified CAD and a CAM had to be created in order to machine the new piece. In addition to the broken piece, the arm that holds on the turbine assembly was not going to be ready for this week of testing. A temporary arm needed to be created, and made to attach to the 3D printed turbine assembly and slip ring. Two acrylic sheets were bolted together, had holed drilled, and was used in place of the 3D printed one.

A CAM was created with the help of a Washburn Shops TA (Lily Ouellette), and a piece of aluminum was found to machine the piece from. With this CAM, the aluminum block slowly turned into the shape of the piece we needed, with a few caveats: In order to speed up milling, a larger end mill was used for the first segment, but not accounted for fully in the subsequent CAMs (for milling at different angles). Once some of the intricate curves had been formed, the mill repositioned for another cut, but ended up passing right through a chunk of the finished part of the piece. The damage was not severe or catastrophic, but it was unexpected. The bad cut was due to not accounting for the change in end mill size from the previous CAM.

While the last few cuts were being milled, the new turbine assembly arm was wired through the slip ring, and fixed to the SUSK. The change between the 3D printed arm to



the newly created acrylic piece meant that the original method for attaching the slip ring would no longer work, and a new method had to be implemented. A raised slip ring with an attached, hollow shaft was created and wired together, and then attached to the SUSKs MOLEX connector alongside the servo wiring. The makeshift turbine assembly was able to rotate freely, but posed an issue during testing where it would lock occasionally, and stay in the same position.

During the final few passes of the new aluminum part, the piece caught on the mill, and started to shred the piece. This meant that the final piece was warped and had ragged, sharp edges. With some bending, cutting, and drilling, it fit into the parts it needed to. Luckily it was secure enough to have a rigid connection, and would work as a replacement part.

The third day was the first day that the turbine was attached. The first few tests the speed of the system was slower than the tests without the turbine. This shows that the turbine causes a significant amount of drag on the system, and that it is an important part in determining the speed of the system. Many tests at different speeds were conducted, and the person controlling the SUSK got used to the added drag that the turbine added. During the testing, the anti-rotation gimbal attachment broke along a 3D printing line, and needed to be repaired. The repair was made with a hose clamp, and proved sufficient for removing rotation of the tether.

On the final day, tests were completed in groups of 10, with each group at a different current speed. With each test, the controller was told to do a the same motion with the servo control, and try to make the periods of movement as symmetric as possible. This allowed for easier comparisons between the tests, and showed that the system could be controlled reliably and consistently. Having similar test results also gave the simulation more set of data to compare to. Each test this day was documented and video taped, and the datasheet for the specific tests can be seen in Appendix D.

Each speed increase caused the motion of the boat to increase, and the period time to decrease, as predicted. For each test, the recorded turbine voltage had a very distinguished shape, but it only was able to record turbine voltage in one direction due to the turbine assembly not being able to rotate freely. Tests done with the similar control inputs yielded similar motion outputs, which proved the consistency of the system. The newly machined

aluminum piece was holding together very well, and did not allow the system to sag like it did previously.

For speeds of  $0.5 \frac{\text{ft}}{\text{s}}$ ,  $1.0 \frac{\text{ft}}{\text{s}}$ , and  $1.5 \frac{\text{ft}}{\text{s}}$ , the boat had a faster velocity, and the recorded turbine voltage increased. However for the  $2.0 \frac{\text{ft}}{\text{s}}$  test, the results were inconsistent and nearly useless in information. This is due to the high current speed causing the boat to drag under the surface of the water, greatly increasing the drag as soon as the top plane of the boat went under the water. When the boat submerged, the speed would instantly drop, and then the boat would resurface to its normal position. This caused the controls needing to be heavily feathered in order to balance the speed in order to not let it go fast enough to submerge. The turbine voltage readings were very inconsistent between tests, and very choppy due to the quick changes in speed.

After we finished tests at  $2.0 \frac{\text{ft}}{\text{s}}$ , we went back down to  $0.5 \frac{\text{ft}}{\text{s}}$  to test the turbine voltage without the vertical wing to see what voltage is read for just the velocity of the current alone. The no boat motion voltage was taken at  $0.5 \frac{\text{ft}}{\text{s}}$ ,  $1.0 \frac{\text{ft}}{\text{s}}$ ,  $1.5 \frac{\text{ft}}{\text{s}}$  and  $2.0 \frac{\text{ft}}{\text{s}}$ . After these main values were recorded, the turbine was left in the water as the system slowed down to zero velocity in order to measure the turbine voltage at all current speeds, mostly as a quick voltage range reference, and to see the change in voltage based on a constantly changing current speed.

The baseline no boat movement voltages were recorded and used as a reference for each of the tests. This allowed comparison between the cross-current aided voltage and the voltage that a stationary turbine would read in the same current conditions. This will provide some data to back up the claim that the SUSK is more efficient than the stationary turbines it would replace.

Figures 27 - 34 show data collected during tests at Alden Laboratories. The top graph shows the angle of the wing with respect to the boat ( $\theta$ ), the angular position of the boat ( $q_2$ ), and the voltage produced by the turbine. The nomenclature of the angles will be explained more in Chapter 5. In order, there two tests at each of the following current speeds,  $0.5 \frac{\text{ft}}{\text{s}}$ ,  $1.0 \frac{\text{ft}}{\text{s}}$ ,  $1.5 \frac{\text{ft}}{\text{s}}$ , and  $2.0 \frac{\text{ft}}{\text{s}}$ .

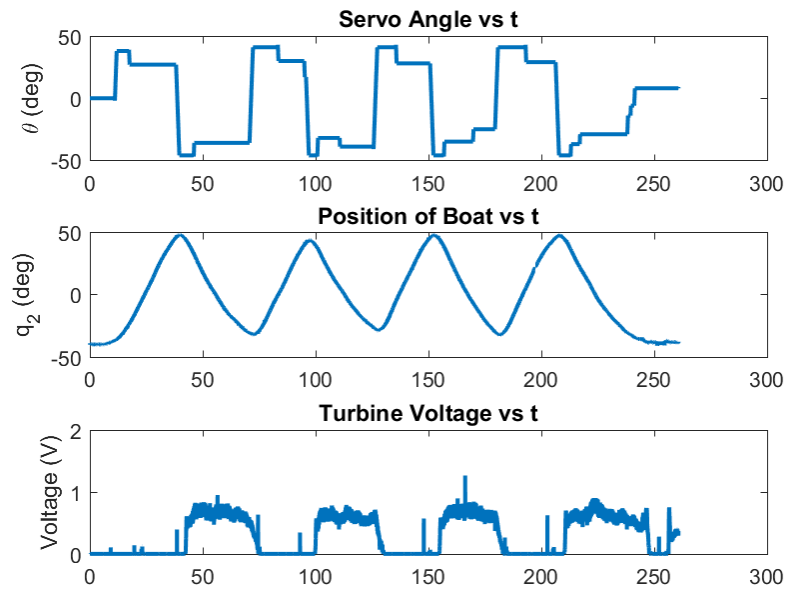


Figure 27: Recorded data for Test 47 with a current velocity of  $0.5 \frac{ft}{s}$ .

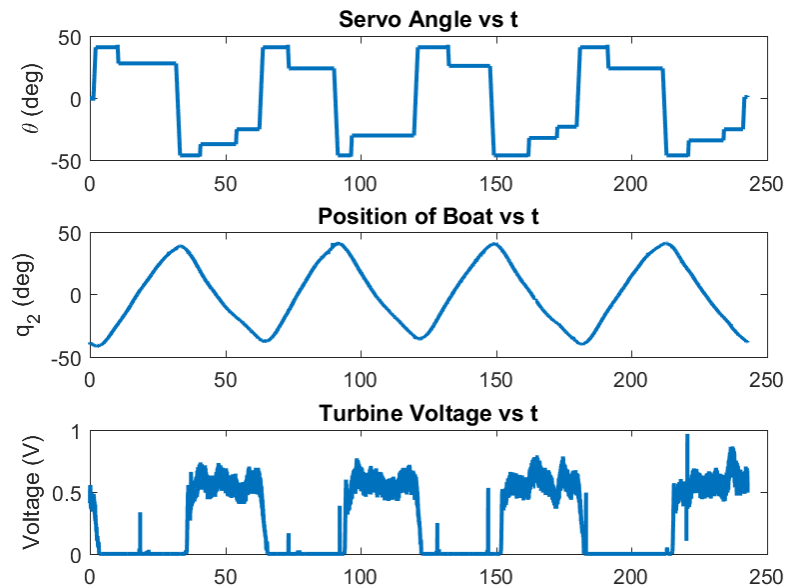


Figure 28: Recorded data for Test 49 with a current velocity of  $0.5 \frac{ft}{s}$ .

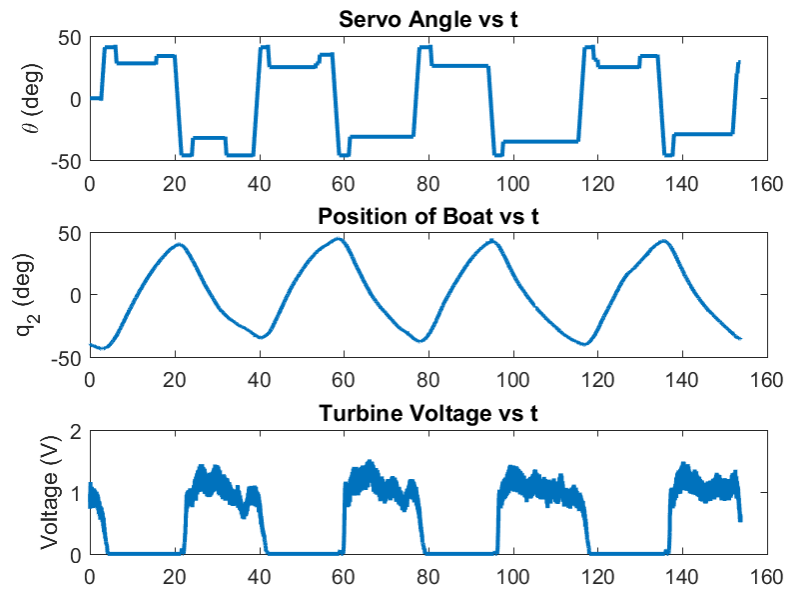


Figure 29: Recorded data for Test 23 with a current velocity of  $1.0 \frac{ft}{s}$ .

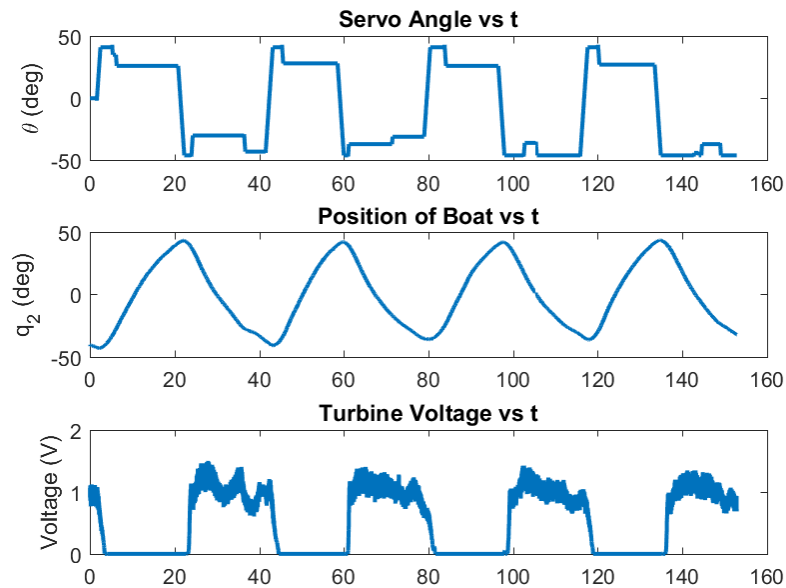


Figure 30: Recorded data for Test 29 with a current velocity of  $1.0 \frac{ft}{s}$ .

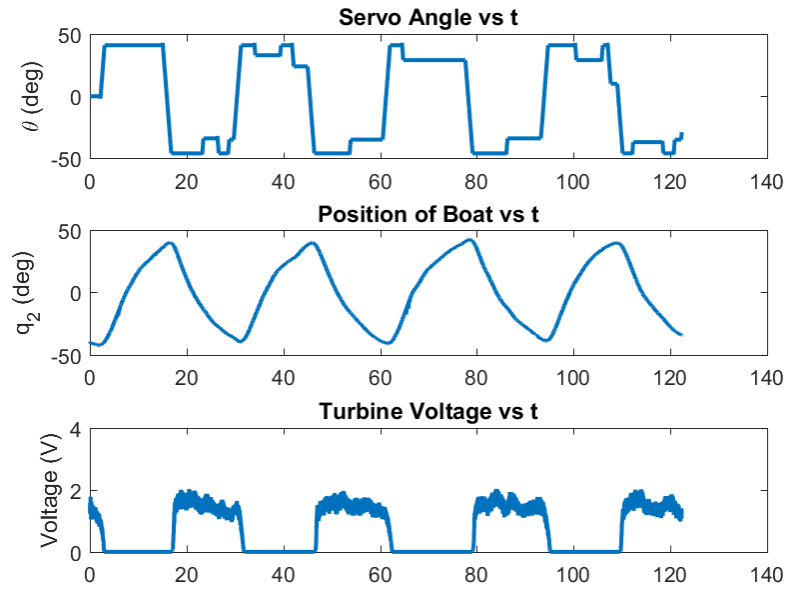


Figure 31: Recorded data for Test 33 with a current velocity of  $1.5 \frac{ft}{s}$ .

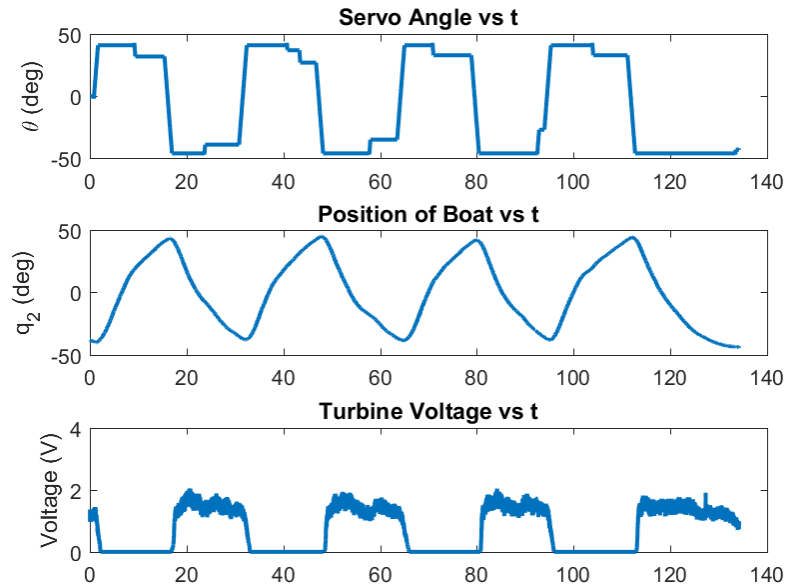


Figure 32: Recorded data for Test 35 with a current velocity of  $1.5 \frac{ft}{s}$ .

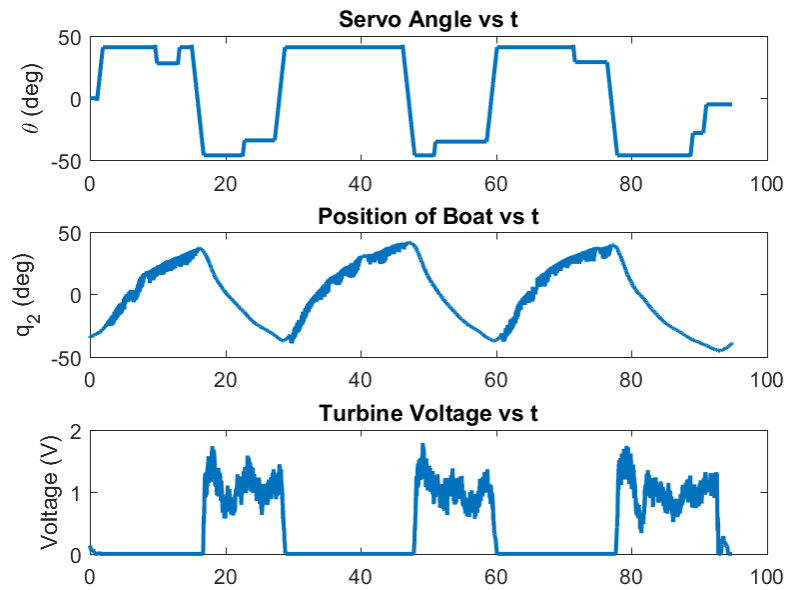


Figure 33: Recorded data for Test 45 with a current velocity of  $2.0 \frac{ft}{s}$ .

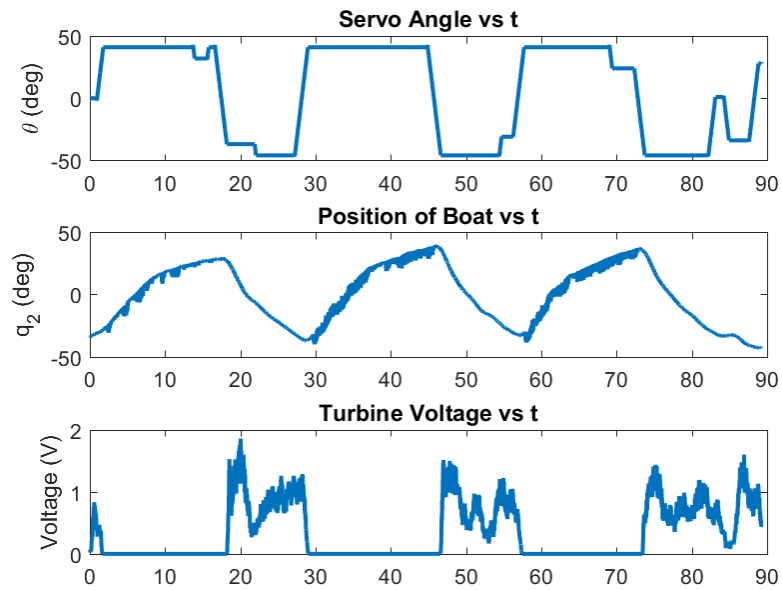


Figure 34: Recorded data for Test 46 with a current velocity of  $2.0 \frac{ft}{s}$ .

# Chapter 5: Simulations of SUSK System

---

According to David McIntyre, “the real power of a theory is its ability to predict results of experiments that you haven’t yet done.” [20]. This sentiment is relevant to this project because while a scale-model system provides a relatively inexpensive method to validate the new SUSK concept, it can not predict the effect of scaling up the system to an industrial level. However, if in general theoretical models can be developed and validated for scale-model systems, they can then be extended to their corresponding full-size system without significant time and effort.

With respect to SUSK, models and simulations are concerned with the effect that scaling up has on velocities, structural loadings, and power output. A full-size system could, for example, require a larger wing to effectively facilitate the reversing motion or could require a larger diameter tether to support tensile loads from forces on the boat.

The simulations of the SUSK system were developed in tandem with the scale-model from the beginning of the conceptual design. There were three main aspects of the development of the simulation. The first main aspect was deriving and verifying the boat’s equations of motion both from first principles and from simplification of previous work by Olinger and Wang [3]. Next, the airfoil selected for the scale-model system was incorporated into the simulation with its aerodynamic data, namely lift and drag coefficients. The hydrodynamic forces on the wing had to be calculated and converted into components radial and tangential to the boat’s motion. The final aspect of developing the simulations was to calculate the necessary outputs from the simulation based off of the simulated values. Overall, simulations showed agreement with test data, which gives opportunity for future work. MATLAB<sup>®</sup> code for the simulation is given in Appendix J.

## 5.1 Equations of Motion

An important first step to developing an accurate simulation of the power generation of the SUSK system was to develop equations of motion. Although the motion of the boat in the SUSK system is not the same as the kite in a TUSK system as discussed in Section 1.4, there are distinct similarities between the two. For this reason, a primary goal was to come to

Table 5: This table shows the parameters of the scale-model SUSK system and how they scale to a full-size system that would be used for power generation. The full-size simulation gives a more realistic idea of potential power output. Scaling factor of 20 used. Some effect of scaling factor on each parameter from [17]

Parameter	Scale-Model Value	Full-Size Value	Dependence on Scale Factor
Boat Area	0.08 m <sup>2</sup>	32 m <sup>2</sup>	$SF^2$
Viscosity of Water	$1 \times 10^{-3} \frac{\text{N}\cdot\text{s}}{\text{m}^2}$	$1 \times 10^{-3} \frac{\text{N}\cdot\text{s}}{\text{m}^2}$	1
Density of Water	$1025 \frac{\text{kg}}{\text{m}^3}$	$1025 \frac{\text{kg}}{\text{m}^3}$	1
Mass of Boat	2.4 kg	19200 kg	$SF^3$
Tether Density	$0.2 \frac{\text{kg}}{\text{m}}$	$0.64 \frac{\text{kg}}{\text{m}}$	$SF^2$
Current Velocity	$0.4572 \frac{\text{m}}{\text{s}}$	$1.3631 \frac{\text{m}}{\text{s}}$	$\sqrt{SF}$
Wing Area	0.05 m <sup>2</sup>	20 m <sup>2</sup>	$SF^2$
Tether Length	3.6 m	72 m	$SF$
Turbine Area	0.073 m <sup>2</sup>	6.88 m <sup>2</sup>	$SF^2$

equations of motion for the SUSK system both by simplifying the more complicated TUSK simulations and also by deriving them from first principles with no previous knowledge of TUSK using both the Lagrangian formulation and the Newton formulation.

### 5.1.1 Simplification of TUSK Simulation

In their 2015 paper, Olinger and Wang presented a six-degree of freedom (DOF) model of a TUSK system. The six coordinates used in the simulation were three spherical coordinates to describe the kite’s position and three Euler angles to describe its orientation. The coordinates can be seen in Figure 35. Given in the paper were extensive, coupled dynamical equations of motion that were derived using the Lagrangian formulation. These equations are given in Appendix E and derived in detail in Appendices F and G.

The Lagrangian

$$\mathcal{L} = K - U \tag{5.1}$$

is constructed as a function of the six generalized coordinates and their time derivatives.



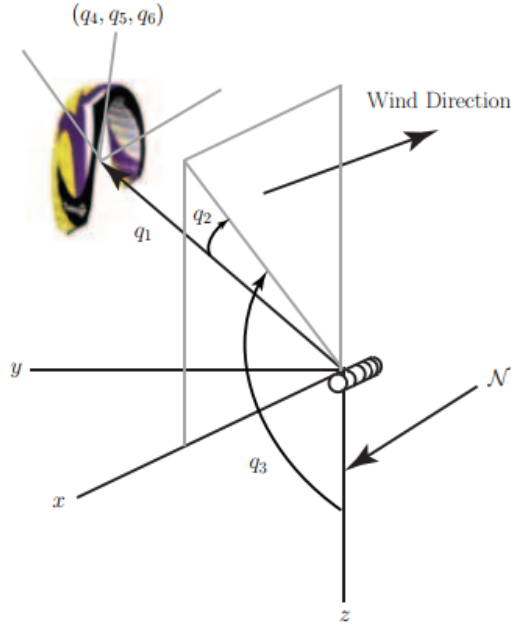


Figure 35: Shown here are the six degrees of freedom of the TUSK system [3]. There are three position coordinates ( $q_1, q_2, q_3$ ) and three orientation coordinates ( $q_4, q_5, q_6$ ). From [21] Copyright ©2011 Worcester Polytechnic Institute

The Euler-Lagrange equation,

$$\frac{d}{dt} \left( \frac{\partial \mathcal{L}}{\partial \dot{q}_i} \right) - \frac{\partial \mathcal{L}}{\partial q_i} = Q_{q_i}, \quad (5.2)$$

gives the equation of motion for a particular generalized coordinate, with  $Q_{q_i}$  being the ‘generalized force’ associated with that coordinate. For angular coordinates, generalized forces are torques, while generalized forces are truly forces for linear coordinates.

Because the SUSK system travels with a constant tether length on the surface of the water, two of the three position coordinates are constant. Additionally, two of the three Euler angles of the wing are constant, and the third was effectively a control angle rather than a true dynamical degree of freedom. Although the three Euler Angles are relevant in the TUSK equations, the orientation of the wing is specified with the single control angle  $\theta$ , measured from a more convenient zero point. The simplification of each coordinate is shown in Table 6.

If the simplifications shown in Table 6 are made in the equations in Appendix E, the

resultant equation (in terms of the density  $\rho$  and variables defined in Table 5) is given by

$$\ddot{q}_2 = \frac{Q_{q_2}}{L_t^2} \left[ \frac{\rho L_t}{3} + M \right]^{-1}. \quad (5.3)$$

### 5.1.2 Derivations From First Principles

Equation 5.3 can be obtained without previous knowledge of the TUSK equations of motion. Appendices H and I use the Lagrangian Formulation applied to the SUSK system and Newton’s 2nd Law in rotational form to arrive at the same equation of motion. It is important that the equation of motion matches when derived in multiple ways because it confirms that this equation is valid for the system. It also reinforces the similarity between the previous TUSK work and the current SUSK work. In these equations, the  $Q_{q_2}$  term still contains all of the hydrodynamic forces on the boat, and these forces will be developed further in the next section.

*Table 6: Simplification of TUSK degrees of freedom to SUSK parameters*

Coordinate	Common Name	TUSK	SUSK
$q_1$	Tether Length	Variable $q_1$	Fixed $L$
$q_2$	Azimuth Angle	Variable $q_2$	Variable $q_2$
$q_3$	Polar Angle	Variable $q_3$	Fixed $\pi/2$
$q_4$	Yaw Angle	Variable $q_4$	N/A
$q_5$	Pitch Angle	Variable $q_5$	N/A
$q_6$	Roll Angle	Variable $q_6$	N/A

## 5.2 Development of Generalized Hydrodynamic Forces

Equation 5.3 suggests that the motion of the boat in the SUSK system is simple compared to the TUSK kite, but the  $Q_{q_2}$  term in the equation still remains ambiguous. The term represents non-conservative generalized forces affecting the  $q_2$  coordinate, which in this case is the hydrodynamic moment produced on the boat about the tether origin.

### 5.2.1 Drag of Turbine and Hull

To estimate the drag due to the hanging turbine, the drag coefficient of a Betz Turbine was assumed, as was done in [3], to be  $\frac{4}{9}$ . The drag was then calculated as

$$D = C_D \left( \frac{1}{2} \rho V_a^2 S_t \right), \quad (5.4)$$

with  $S_t$  as the area of the turbine. Additionally, the drag coefficient from the hull was estimated from various hull models as 0.0035 from [22]. After the application of rubber sealant and incorporation of all portions of the system, the drag coefficient estimate was increased to be 0.35, which is on the same order of magnitude as the turbine drag. This drag is due to the turbine assembly, the hull, the interface between the bottom of the hull and the wing, and other miscellaneous sources of drag in the system. Further work is required to better estimate drag not due to the wing or the turbine airfoil.

### 5.2.2 Lift and Drag of Wing

A majority of the hydrodynamic forces acting on the SUSK system are produced by the vertical wing that is submerged in the apparent flow, which is a vector sum of the boat's velocity and the ambient current velocity. Lift and drag coefficient data as a function of angle of attack for the SUSK's half-chord symmetric airfoil was required to calculate the forces that the wing would produce from the flow. The dimensionless lift and drag coefficients,  $C_L$  and  $C_D$  are converted to lift and drag forces,  $L$  and  $D$ , by

$$\begin{aligned} L &= C_L \left( \frac{1}{2} \rho V_a^2 S \right) \\ D &= C_D \left( \frac{1}{2} \rho V_a^2 S \right), \end{aligned} \quad (5.5)$$

where  $\rho$  is the density of water,  $V_a$  is the total apparent current velocity (discussed more in the next section), and  $S$  is the planform area of the vertical wing [19].

The open-source XFRLR5 airfoil analysis software tool was used to develop lift and drag data for the half-chord symmetric airfoil. The program uses a method known as vortex-panel finite element method to develop lift and drag coefficients for airfoils. A more detailed

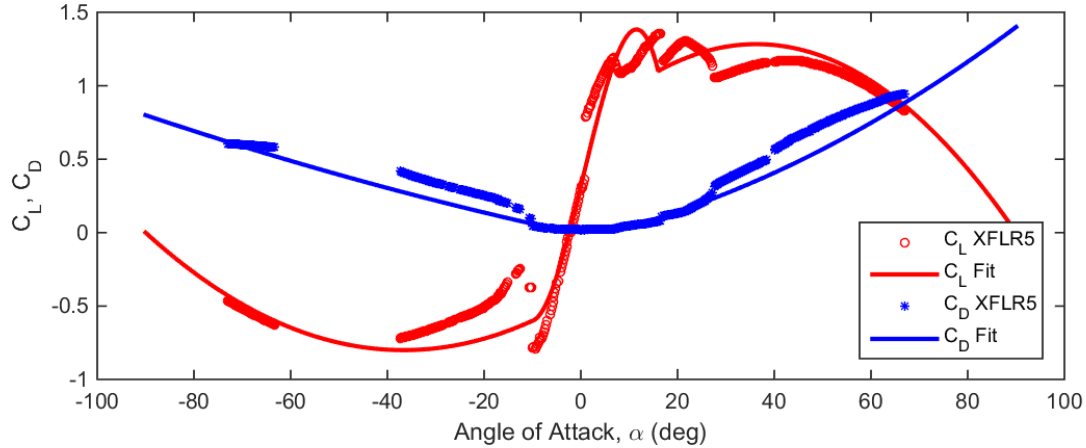


Figure 36: Lift coefficient and drag coefficient fitted using splines

description of the method used by the software can be found in [19]. The program's numerical algorithm failed to converge at many angles of attack  $\alpha$  outside of the interval  $-15^\circ \leq \alpha \leq 15^\circ$ , so a method of curve fitting the converged points was required. The method of spline fitting was selected for fitting the data. Spline fitting fits multiple spline curves, generally polynomials, to distinct subintervals of the domain of a function, allowing intervals with differently shaped curves to be independent. Based on how many unknown coefficients each spline has, a certain number of conditions can be met on the graph (i.e. fixing function values at given points, fixing derivatives at certain points, matching function values between splines, matching derivative values between splines). For fitting the coefficients of lift and drag, the total interval of  $-90^\circ \leq \alpha \leq 90^\circ$  was divided into three subintervals, based on inspection of where the curves changed character, as follows:

- $-90^\circ \leq \alpha < -10^\circ$
- $-10^\circ \leq \alpha \leq 16^\circ$
- $16^\circ < \alpha \leq 90^\circ$

Lift coefficient and drag coefficients were then fit as three part splines with different spline curves for each segment. The final spline fits for both lift and drag coefficients are shown in Figure 36, showing three distinct intervals for both coefficient's.

## Lift Coefficient

For fitting of the lift coefficient, the outer two splines were quadratic functions, while the inner spline was a cubic, giving an equation for lift coefficient of

$$C_L(\alpha) = \begin{cases} B_1\alpha^2 + C_1\alpha + D_1 & -90^\circ \leq \alpha < -10^\circ \\ A_2\alpha^3 + B_2\alpha^2 + C_2\alpha + D_2 & -10^\circ \leq \alpha \leq 16^\circ \\ B_3\alpha^2 + C_3\alpha + D_3 & 16^\circ < \alpha \leq 90^\circ \end{cases} \quad (5.6)$$

and giving ten conditions that could be fixed on the fit. The ten conditions that were chosen were

1.  $C_L(90^\circ) = 0$
2.  $C_L(-90^\circ) = 0$
3. Match  $C_L$  splines at  $-10^\circ$
4. Match  $C_L$  splines at  $16^\circ$
5.  $C_L(-10^\circ) = -0.6$
6.  $C_L(16^\circ) = 1.25$
7.  $C_L(-50^\circ) = -0.75$
8.  $C_L(50^\circ) = 1.2$
9.  $C_L(2.4^\circ) = 0$
10.  $C_L(0^\circ) = 0.3163$

Each of these ten conditions was evaluated in Equation 5.6 to give a ten equation-ten unknown system of equations to solve for the unknown constants. The final equation for the spline fit was then

$$C_L(\alpha) = \begin{cases} 0.00028125\alpha^2 + 0.020625\alpha - 0.4219875 & -90^\circ \leq \alpha < -10^\circ \\ -0.000376346\alpha^3 + 0.00061774\alpha^2 + 0.135442\alpha + 0.3163 & -10^\circ \leq \alpha \leq 16^\circ \\ -0.00044515\alpha^2 + 0.032321145\alpha + 0.69682035 & 16^\circ < \alpha \leq 90^\circ \end{cases} \quad (5.7)$$

where the high level of decimal places is required as  $\alpha$  in this equation is in degrees.

## Drag Coefficient

For fitting the drag coefficient, all spline segments were quadratic functions. This gave an equation for the drag coefficient of

$$C_L(\alpha) = \begin{cases} A_4\alpha^2 + B_4\alpha + C_4 & -90^\circ \leq \alpha < -10^\circ \\ A_5\alpha^2 + B_5\alpha + C_5 & -10^\circ \leq \alpha \leq 16^\circ \\ A_6\alpha^2 + B_6\alpha + C_6 & 16^\circ < \alpha \leq 90^\circ \end{cases} \quad (5.8)$$

There are nine conditions that can be imposed on this function, and the nine conditions chosen were

1.  $C_D(0^\circ) = 0.02$
2. Match  $C_D$  splines at  $-10^\circ$
3. Match  $C_D$  splines at  $16^\circ$
4.  $C_D(-10^\circ) = 0.06$
5.  $C_D(16^\circ) = 0.1$
6.  $C_D(90^\circ) = 1.4$
7.  $C_D(-90^\circ) = 0.8$
8. Match  $C_D$  spline derivatives at  $-10^\circ$
9. Match  $C_D$  spline derivatives at  $16^\circ$

Each of these nine conditions can be evaluated in Equation 5.8 to give a nine equation-nine unknown system of equations to solve for the unknown constants. The final equation for the spline fit was then

$$C_D(\alpha) = \begin{cases} 0.00002235577\alpha^2 - 0.007014423\alpha - 0.0123798 & -90 \leq \alpha < -10^\circ \\ 0.000346154\alpha^2 - 0.00053846\alpha + 0.02 & -10^\circ \leq \alpha \leq 16^\circ \\ 0.0000949879\alpha^2 + 0.00749885\alpha - 0.0442985 & 16^\circ < \alpha \leq 90^\circ \end{cases} \quad (5.9)$$

Equations 5.7 and 5.9 will be used in the next section to calculate lift and drag coefficients on the wing and thus lift and drag on the wing during the simulation.

Table 7: Four cases of apparent flow over the wing

	Leading Edge Direction	Angle of Attack Sign
Case 1	Left	+
Case 2	Left	-
Case 3	Right	+
Case 4	Right	-

### 5.2.3 Leading Edge and Effective Angle of Attack

Figure 37 shows an arbitrary orientation of the boat and the variable nomenclature used to describe its orientation. The half-chord symmetric airfoil chosen for the system eliminates the need for the wing to rotate  $180^\circ$  to facilitate reversing boat motion. This also means that either end of the wing act as the leading edge. Figure 38 shows four cases, listed in Table 7.

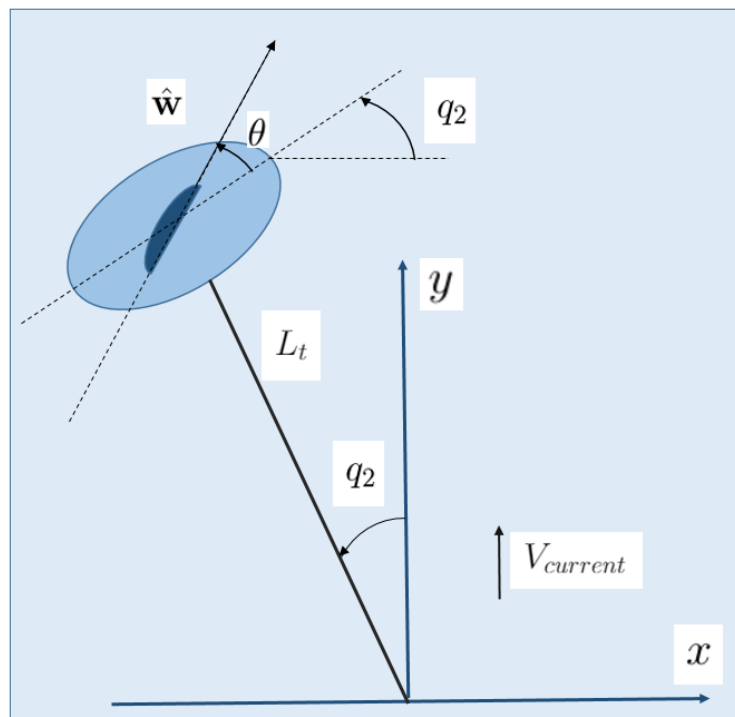


Figure 37: Boat Motion Diagram

The simulations of the SUSK system needed a way to determine which of the four cases was occurring at each simulation step. Each case will have its lift and drag oriented differ-

ently, requiring different geometric conversions to forces parallel and perpendicular to the tether.

Many aspects of the four cases in Figure 38 are identical. First, define the surrounding current velocity, which is assumed to be constant with magnitude  $V_{\text{current}}$  such that

$$\mathbf{V}_c = V_{\text{current}} \hat{\mathbf{j}} \quad (5.10)$$

Assuming that the point at which the tether attaches to the gimbal is the origin, the cartesian position and velocity of the boat can be written as

$$\mathbf{r}_{\text{boat}} = -L_t \sin(q_2) \hat{\mathbf{i}} + L_t \cos(q_2) \hat{\mathbf{j}} \quad (5.11)$$

$$\mathbf{V}_{\text{boat}} = -L_t \dot{q}_2 \cos(q_2) \hat{\mathbf{i}} - L_t \dot{q}_2 \sin(q_2) \hat{\mathbf{j}} \quad (5.12)$$

The total apparent velocity that is hitting the boat,  $\mathbf{V}_{c,\text{total}}$ , is therefore

$$\mathbf{V}_{c,\text{total}} = \mathbf{V}_c - \mathbf{V}_{\text{boat}} = (L_t \dot{q}_2 \cos(q_2)) \hat{\mathbf{i}} + (L_t \dot{q}_2 \sin(q_2) + V_{\text{current}}) \hat{\mathbf{j}} \quad (5.13)$$

To determine the effective angle of attack between this flow and the wing of the SUSK system, we need to consider the vector pointing in the direction of the wing's chordline, termed as  $\hat{\mathbf{w}}$ , which is represented in cartesian coordinates as

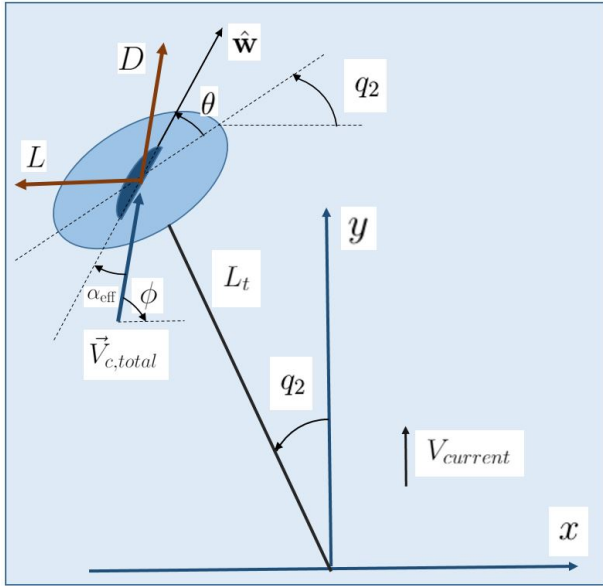
$$\hat{\mathbf{w}} = \cos(\theta + q_2) \hat{\mathbf{i}} + \sin(\theta + q_2) \hat{\mathbf{j}}. \quad (5.14)$$

The angle made between  $\mathbf{V}_{c,\text{total}}$  and  $\hat{\mathbf{w}}$  will give the magnitude of the effective angle of attack, and we can use the dot product to determine the cosine of this angle as

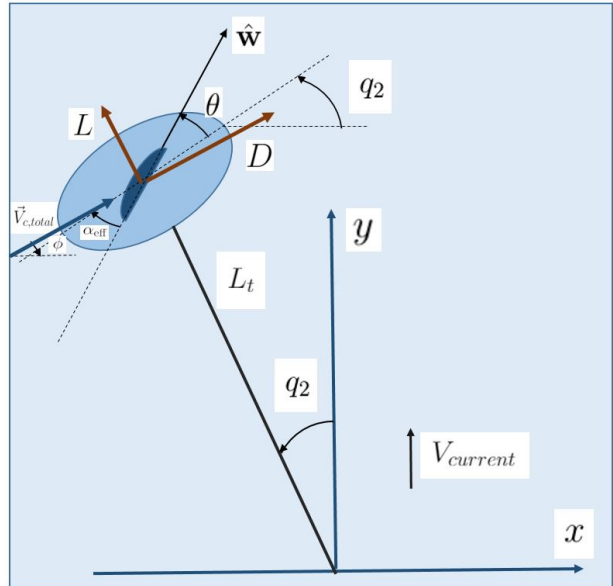
$$\cos(\alpha_{\text{eff}}) = \frac{\hat{\mathbf{w}} \cdot \mathbf{V}_{c,\text{total}}}{|\mathbf{V}_{c,\text{total}}|} \quad (5.15)$$

knowing that  $|\hat{\mathbf{w}}| = 1$  because  $\hat{\mathbf{w}}$  is a unit vector. It is required that  $\alpha$  be in the interval  $[-\frac{\pi}{2}, \frac{\pi}{2}]$ . This would require that the cosine in Equation 5.15 be positive, but that will not always be the case, so now we must consider separately the cases outline by Figure 38.

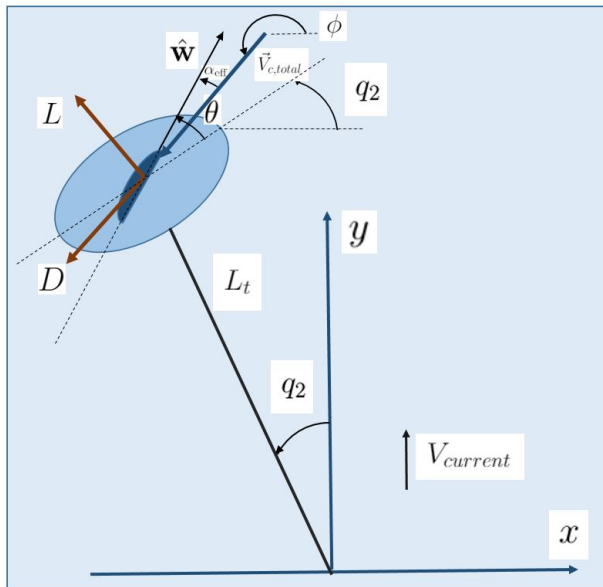




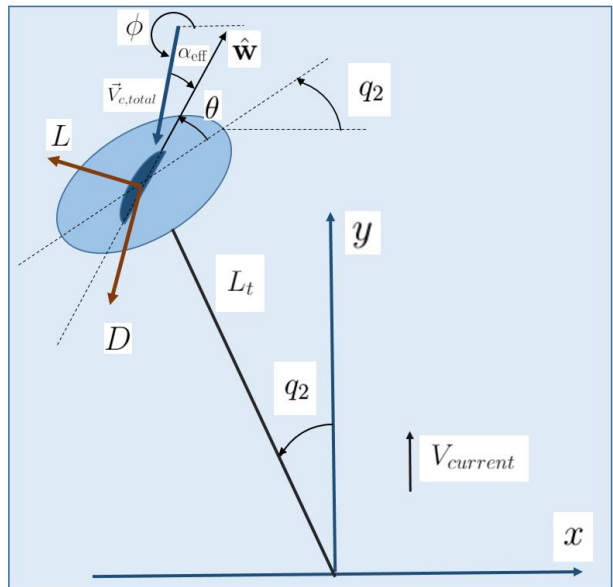
(a) Case 1



(b) Case 2



(c) Case 3



(d) Case 4

Figure 38: Four possible cases of flow in relation to the wing

## Case 1

In Case 1, the left side of the wing is acting as the leading edge, and the flow has a positive effective angle of attack with respect to the wing. The cosine in Equation 5.15 will have a negative value when the left edge is acting as the leading edge, so it is necessary to negate the result of that equation before calculating  $\alpha_{\text{eff}}$ . Additionally, the effective angle of attack will be positive if  $\phi > q_2 + \theta$ .

After calculating lift and drag, which act parallel and normal to the flow direction, the forces need to be converted to forces parallel and normal to the tether, as those are needed to calculate  $Q_{q_2}$  and the tension on the tether. For Case 1, the lift and drag are converted first to normal and axial forces as

$$\begin{aligned} N &= L \cos(\alpha) + D \sin(\alpha) \\ A &= -L \sin(\alpha) + D \cos(\alpha) \end{aligned} \tag{5.16}$$

and then converted to parallel and normal forces to the tether as

$$\begin{aligned} F_p &= N \sin(q_2) - A \cos(q_2) \\ F_n &= N \cos(q_2) + A \sin(q_2) \end{aligned} \tag{5.17}$$

These simple geometric conversions convert lift and drag on the wing at an arbitrary orientation to forces parallel and normal to the tether.

## Case 2

In Case 2, the left side of the wing is still acting as the leading edge, but now the flow has a negative effective angle of attack with respect to the wing. The cosine of Equation 5.15 will still have a negative value and thus have to be negated. However, the effective angle of attack will be positive if  $\phi < q_2 + \theta$ .

The conversions in Equations 5.16 and 5.17 also apply here to convert lift and drag forces to parallel and normal forces with respect to the tether, however they must be modified slightly based on changes in geometry and therefore become

$$\begin{aligned}
N &= L \cos(\alpha) - D \sin(\alpha) \\
A &= -L \sin(\alpha) + D \cos(\alpha)
\end{aligned}
\tag{5.18}$$

$$\begin{aligned}
F_p &= N \sin(q_2) - A \cos(q_2) \\
F_n &= N \cos(q_2) + A \sin(q_2)
\end{aligned}
\tag{5.19}$$

### Case 3

In Case 3, the right side of the wing is acting as the leading edge, and the flow has a positive effective angle of attack with respect to the wing. The cosine of Equation 5.15 will now have a positive value and the value of  $\alpha_{\text{eff}}$  can be directly calculated without negation. Now, because the angle  $q_2 + \alpha_{\text{eff}}$  is shifted by  $\pi$  from the approximate location of  $\phi$ , the direction of  $\hat{\mathbf{w}}$  must be shifted by  $\pi$  to make a similar comparison as in Cases 1 and 2. Therefore, if  $q_2 + \theta + \pi > \phi$ , then the effective angle of attack will be positive.

Calculation of forces parallel and normal to the tether requires another modification to Equations 5.16 and 5.17, giving

$$\begin{aligned}
N &= L \cos(\alpha) + D \sin(\alpha) \\
A &= L \sin(\alpha) - D \cos(\alpha)
\end{aligned}
\tag{5.20}$$

$$\begin{aligned}
F_p &= N \sin(q_2) - A \cos(q_2) \\
F_n &= N \cos(q_2) + A \sin(q_2)
\end{aligned}
\tag{5.21}$$

### Case 4

In the final flow orientation, Case 4, the right side of the wing is acting as the leading edge, and the flow has a negative angle of attack with respect to the wing. The cosine of Equation 5.15 will still be positive, so the value of  $\alpha_{\text{eff}}$  can still be directly calculated. Now, the angle of attack will be negative if  $q_2 + \theta + \pi < \phi$ , completing the four cases of flow.

Calculation of forces parallel and normal to the tether requires one final modification to Equations 5.16 and 5.17, giving

$$N = L \cos(\alpha) - D \sin(\alpha) \tag{5.22}$$

$$A = L \sin(\alpha) - D \cos(\alpha)$$

$$F_p = N \sin(q_2) - A \cos(q_2) \tag{5.23}$$

$$F_n = N \cos(q_2) + A \sin(q_2)$$

The preceding four cases completely describe the possible flow cases past the wing.

### 5.2.4 Adjustment of Wing Angle

Control of the wing angle  $\theta$  was done manually during testing of the SUSK system, but it needed to be autonomous in the simulation. To accomplish this, the states of the system ( $q_2$  and  $\dot{q}_2$  were broken up into 8 cases. For each case, a specific value of  $\theta$  was assigned as the ‘trim’ value of  $\theta$  for that case. The cases, along with their trim  $\theta$  values, are shown in Table 8. The value  $q_{2,\text{lim}}$  represents a limiting angle at which the control should start to reverse the motion of the boat, and was typically in the range of  $35^\circ \leq q_{2,\text{lim}} \leq 50^\circ$ . This divides the angular spectrum into quadrants, giving 8 cases when the quadrants are taken at both a positive and negative angular velocity  $\dot{q}_2$ .

The trim values were initially selected as the angle which provided the largest  $Q_{q_2}$  in the desired direction of acceleration, but these values were changed to lie within physical constraints posed by the setup of the SUSK system. Namely, the servos limited the travel of the wing to approximately  $-45^\circ \leq \theta \leq 45^\circ$ . Additionally, as simulations were compared to test runs, the selected angles were aligned with manual inputs as well as possible.

To model the actual motion of the servo, the angular velocity of the servo was taken to be  $1.165 \frac{\text{rad}}{\text{s}}$ . When  $\theta$  was not within  $1^\circ$  of the required trim value, the angular speed was applied until  $\theta$  was within a  $1^\circ$  envelope of its specified value.

Table 8: Cases of state and their trim  $\theta$  for control

Case	Details		
1	$\dot{q}_2 < 0$	$q_2 < -q_{2,\text{lim}}$	$Q_{q_2} > 0$
2	$\dot{q}_2 < 0$	$-q_{2,\text{lim}} \leq q_2 \leq 0$	$Q_{q_2} < 0$
3	$\dot{q}_2 < 0$	$0 \leq q_2 \leq q_{2,\text{lim}}$	$Q_{q_2} < 0$
4	$\dot{q}_2 < 0$	$q_2 > q_{2,\text{lim}}$	$Q_{q_2} < 0$
5	$\dot{q}_2 > 0$	$q_2 < -q_{2,\text{lim}}$	$Q_{q_2} > 0$
6	$\dot{q}_2 > 0$	$-q_{2,\text{lim}} \leq q_2 \leq 0$	$Q_{q_2} > 0$
7	$\dot{q}_2 > 0$	$0 \leq q_2 \leq q_{2,\text{lim}}$	$Q_{q_2} > 0$
8	$\dot{q}_2 > 0$	$q_2 > q_{2,\text{lim}}$	$Q_{q_2} < 0$

## 5.3 Post-processing of Simulation Results

For a simulation to be complete, it must output both its directly simulated parameters as well as other data calculated from those parameters. For the SUSK simulation, four parameters were simulated:  $q_2$ ,  $\dot{q}_2$ ,  $\theta$ , and  $\dot{\theta}$ . However, the simulations need to provide information including power, tether tension, effective angle of attack, and other information. The following section will outline what information is output from simulations, why it is relevant for the SUSK system, and how it was calculated within the simulation.

### 5.3.1 Simulation Outputs

Figures 39 - 41 show the output of the simulation for a sample run. Following the figures, a description of each output is given.

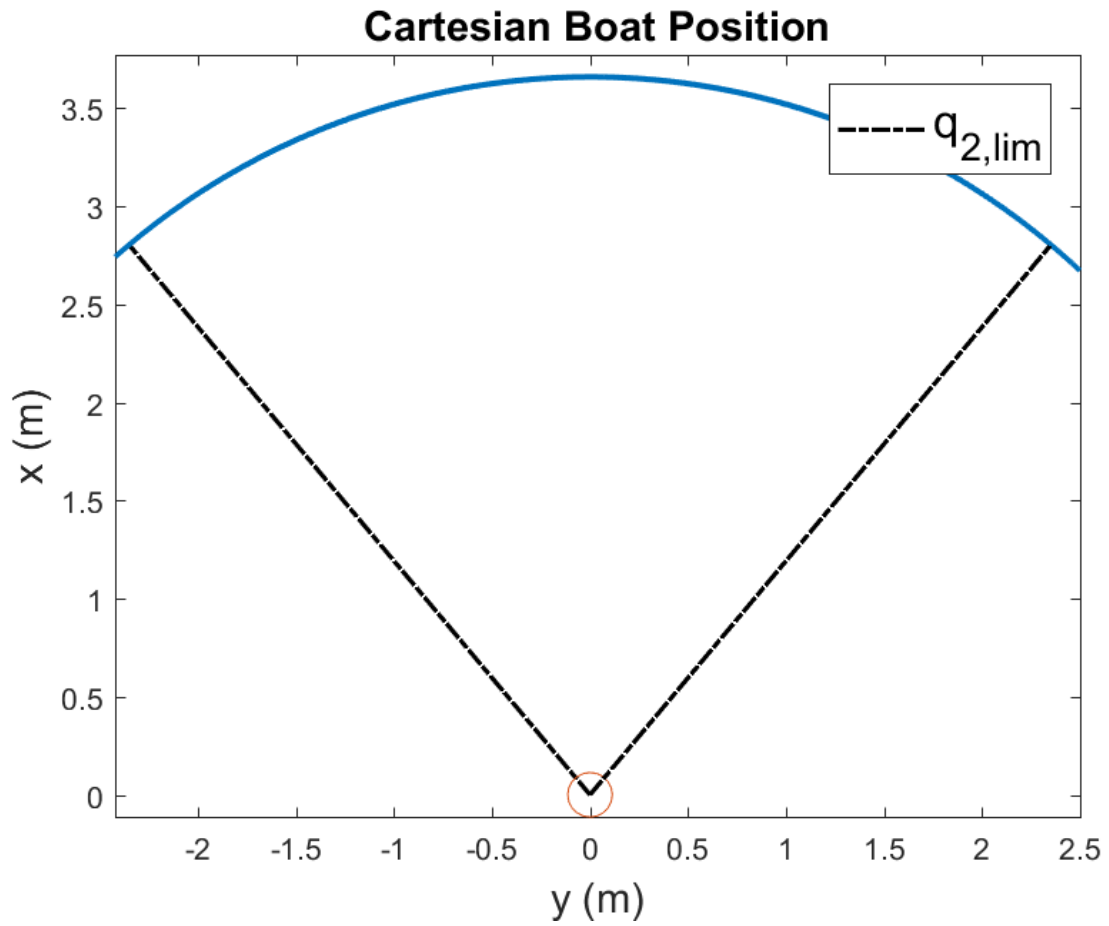


Figure 39: Sample output of simulation run, part 1

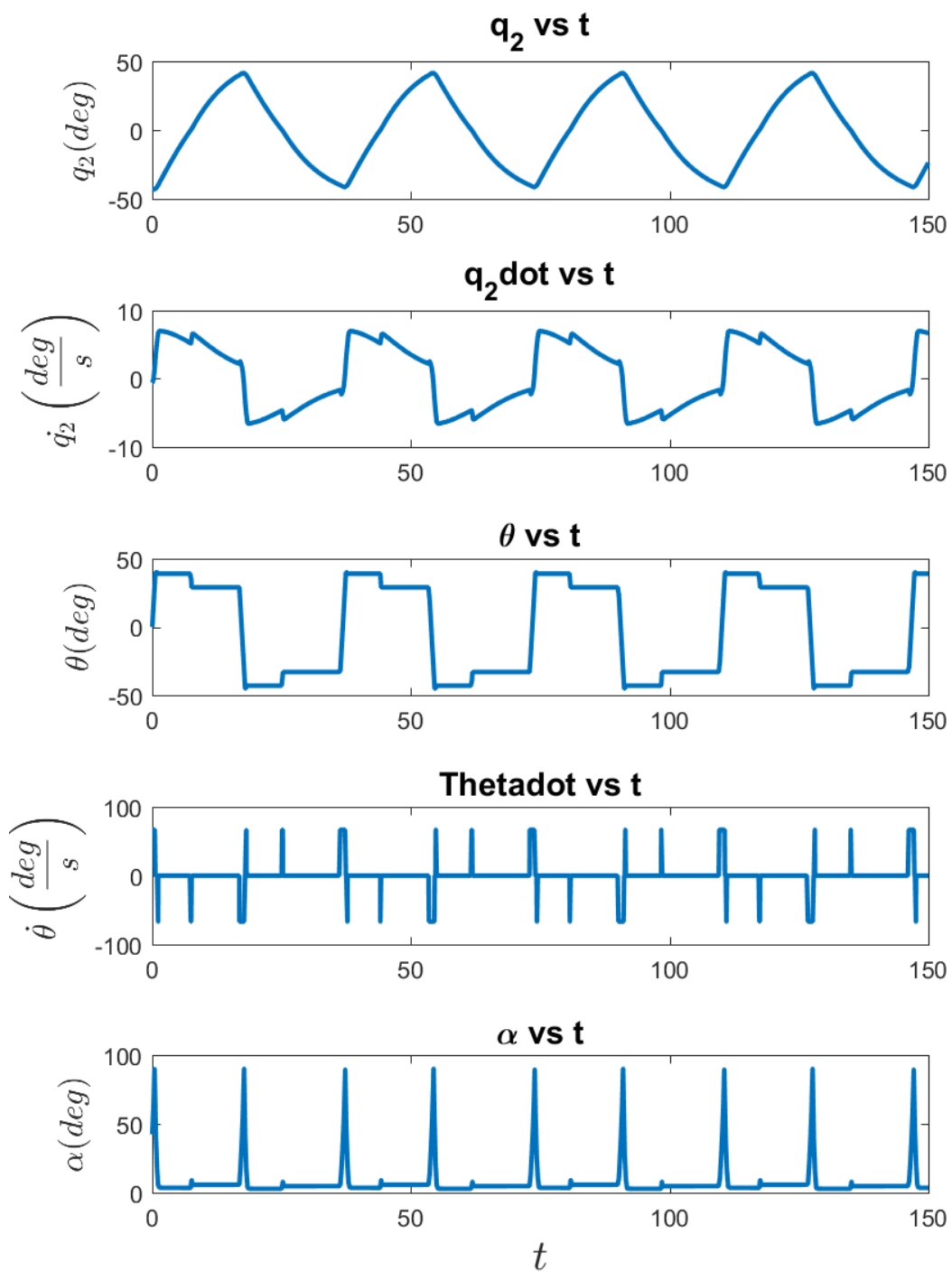


Figure 40: Sample output of simulation run, part 2

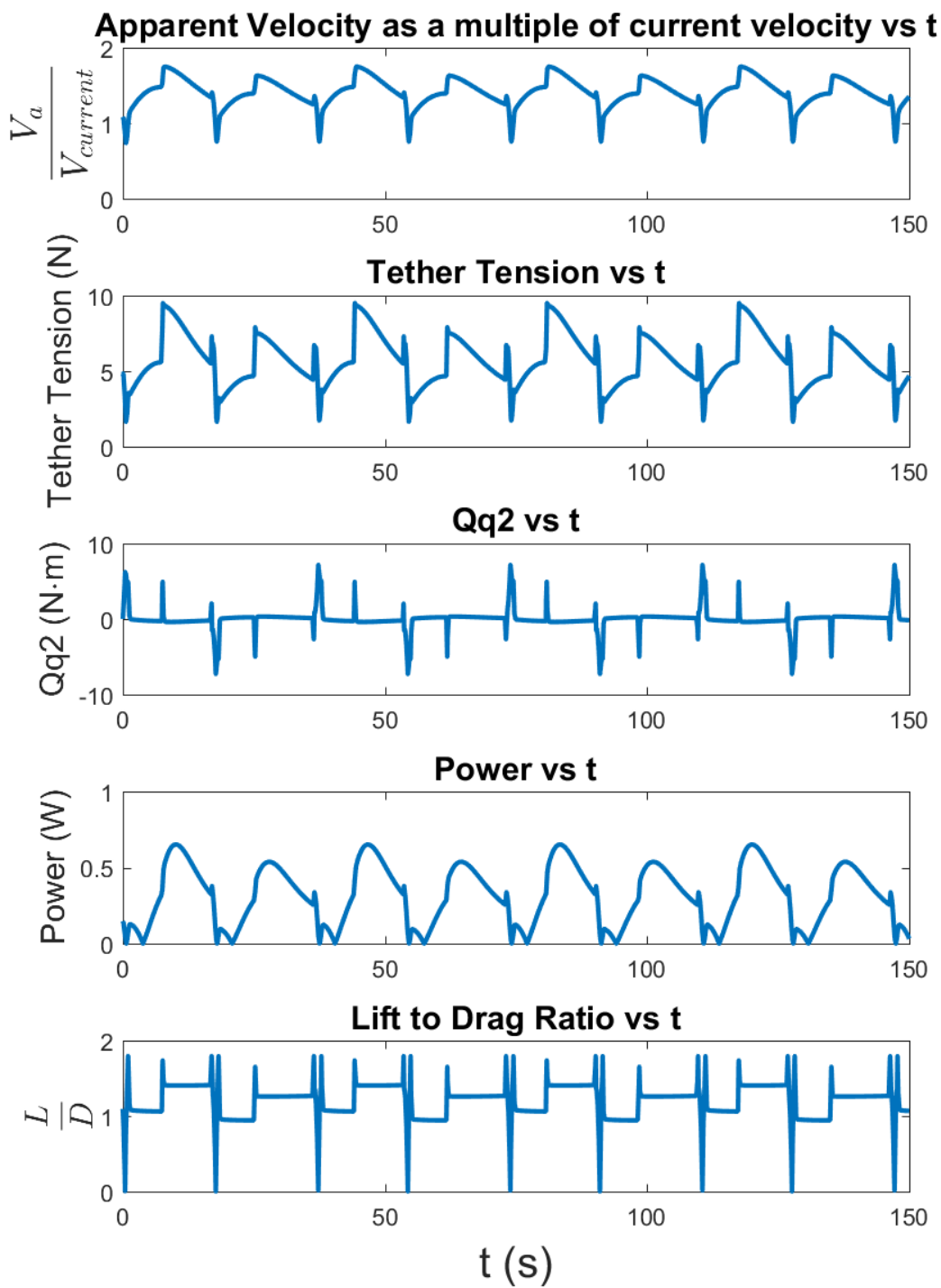


Figure 41: Sample output of simulation run, part 3



### **Cartesian Coordinates ( $x, y$ )**

Because the SUSK system remains on the surface of the water and has a rigid tether, its position is described by one angular coordinate,  $q_2$ . However, it is also useful to convert this coordinate back into cartesian coordinates to visualize the arc that the system sweeps out with its motion. The equations to convert from the  $q_2$  angle to cartesian coordinates are evident from Figure 37, and are

$$\begin{aligned}x &= -L_t \sin(q_2) \\ y &= L_t \cos(q_2)\end{aligned}\tag{5.24}$$

These results should not be more than a constant radius arc, but they provide a visualization of the physical motion of the SUSK system.

### **Effective Angle of Attack ( $\alpha_{\text{eff}}$ )**

At each step in the simulation run, the effective angle of attack  $\alpha_{\text{eff}}$  is calculated to then calculate lift and drag coefficient on the wing. This value is stored and outputted versus time. This output shows when the SUSK system is utilizing both the lift and drag of its wing at low angles of attack versus when it is utilizing the wing as a bluff body only for its drag at high angles of attack, normally during the reversing of the motion. Additionally, the fit shown in Figure 36 shows some inaccuracies in fitting in intermediate values of  $\alpha$  between approximately  $\pm 15^\circ$  and  $\pm 50^\circ$ , so the output of the effective angle of attack can evaluate how often the system operates at this effective angle of attack.

### **Boat Angular Position and Velocity ( $q_2, \dot{q}_2$ )**

Based on the way that  $\theta$  is set for each simulation run, the results for  $q_2$  and  $\dot{q}_2$  should be periodic, as the motion of the system will be. In particular  $q_2$  can be used to study how far the system will overshoot the limit  $q_{2,\text{lim}}$ , giving a sense of how long the system takes to respond to effort to reverse its motion.

### **Wing Angular Position and Velocity ( $\theta, \dot{\theta}$ )**

An important output of the simulation is a graph of  $\theta$  and  $\dot{\theta}$  versus time. This information represents how the system was controlled during the simulation and can be compared to test run control to justify any differences between manual control tests and autonomous control

simulations. Because  $\dot{\theta}$  is either zero or a single positive or negative value, the graph of  $\theta$  should be a piecewise graph with flat and steeply sloped sections.

### **Total Apparent Current Velocity Over Ambient Current Velocity ( $\frac{V_a}{V_{\text{current}}}$ )**

The total apparent current velocity expressed as a multiple of the ambient current velocity shows how effectively the SUSK system moves across the current and amplifies the ambient current velocity. Ideally, this value will be as high as 3 or 4 and will hopefully rarely be around and below 1.

### **Torque About Tether Origin ( $Q_{q_2}$ )**

The torque  $Q_{q_2}$  on the boat about the tether origin is the driver of the motion. The variation of this value throughout the period of motion can give insight on how to optimize the system's motion.

### **Tether Tension ( $T$ )**

The tension on the tether, which is the resultant force parallel to the tether, is important for structural considerations of the SUSK. As several parts completely broke or were compromised during testing, information about structural loads placed on SUSK components is important.

### **Power ( $P$ )**

The power output of the SUSK system versus time is estimated by

$$P = C_P \left( \frac{1}{2} \rho S_t V_a^3 \right) \quad (5.25)$$

where  $S_t$  is turbine area. For simulation purposes, the power coefficient  $C_P$  was taken to be  $\frac{16}{27}$ , which is the ideal case. The actual power coefficient for a SUSK system will depend on the turbine selected as well as the electronics used to harness and store the power. Regardless of power coefficient, the general profile of the power generation will depend on  $V_a^3$  and can be obtained from the simulation output.

### **Lift-to-Drag Ratio ( $\frac{L}{D}$ )**

As shown in Equations 1.1 and 1.2, the maximum theoretical apparent current velocity and maximum theoretical power output for tethered energy systems depend on their overall lift-to-drag ratio. As such, it is useful to output this data over time for a simulation, as it

can be compared to apparent current velocities and instantaneous power outputs.

## 5.4 Simulation Results Compared to Tests

Shown in the following plots a comparison of 8 simulation runs with test runs. The wing position  $\theta$  and boat position  $q_2$  are plotted for the simulation and test, and the results show a high correlation. There are two runs at four different flow velocities:  $0.5 \frac{\text{ft}}{\text{s}}$ ,  $1.0 \frac{\text{ft}}{\text{s}}$ ,  $1.5 \frac{\text{ft}}{\text{s}}$ , and  $2.0 \frac{\text{ft}}{\text{s}}$ . The only parameters that are varied between simulation runs are the trim values of  $\theta$  and the limit  $q_{2,\text{lim}}$ , corresponding to the subjectivity of manual control. The  $\theta$  versus time curve in the simulation was matched as closely as possible to the test data based on the simulation control logic. Additionally, the drag coefficient of the hull was significantly increased for the  $2.0 \frac{\text{ft}}{\text{s}}$  runs due to the hull digging into the water as mentioned in Section 4.3.

The correlation in between the simulations and test runs suggests that the simulations can be further developed to predict the motion, power output, and other information about a scaled up SUSK system.

### Simulation Result Versus Testing Result

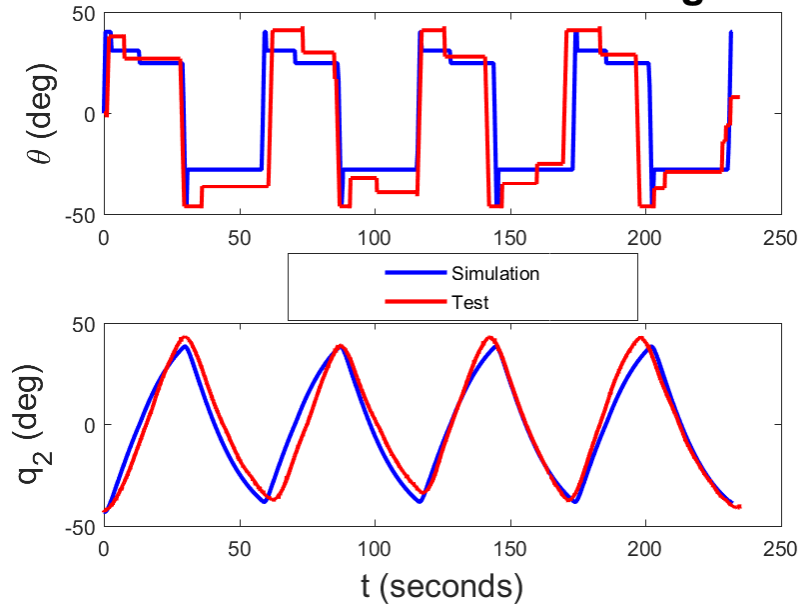


Figure 42: Testing and simulation comparison for Test 47 with a current velocity of  $0.5 \frac{ft}{s}$ .

### Simulation Result Versus Testing Result

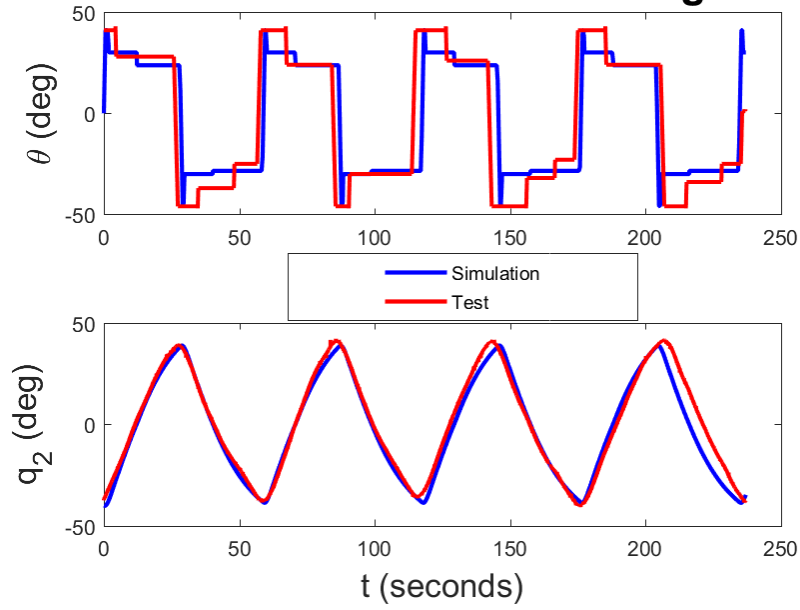


Figure 43: Testing and simulation comparison for Test 49 with a current velocity of  $0.5 \frac{ft}{s}$ .

### Simulation Result Versus Testing Result

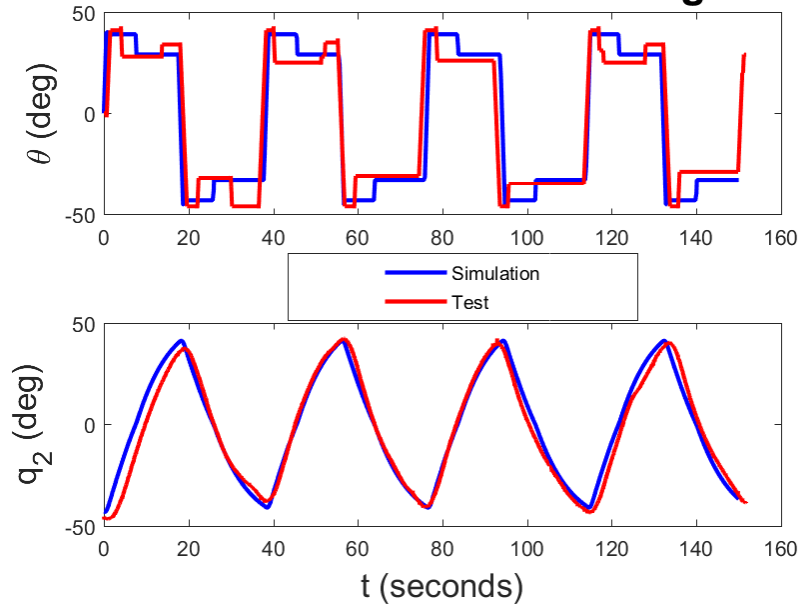


Figure 44: Testing and simulation comparison for Test 23 with a current velocity of  $1.0 \frac{ft}{s}$ .

### Simulation Result Versus Testing Result

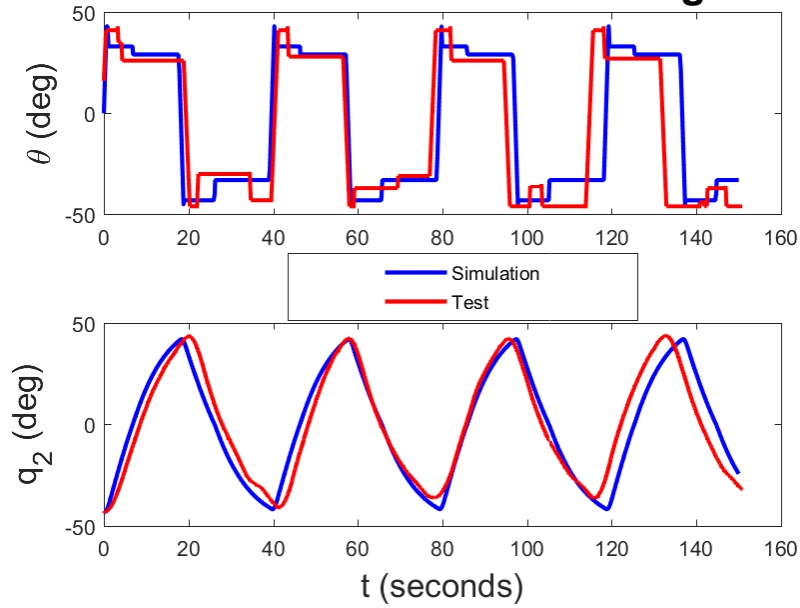


Figure 45: Testing and simulation comparison for Test 29 with a current velocity of  $1.0 \frac{ft}{s}$ .

### Simulation Result Versus Testing Result

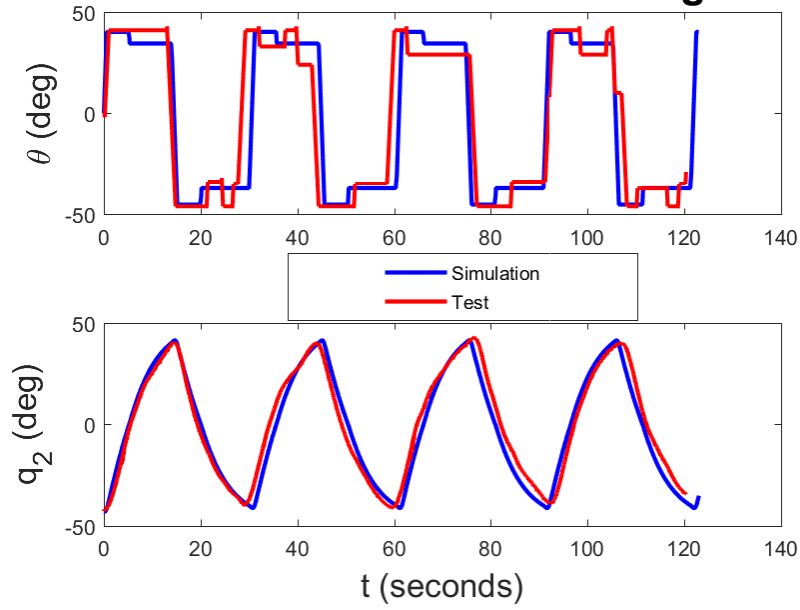


Figure 46: Testing and simulation comparison for Test 33 with a current velocity of  $1.5 \frac{ft}{s}$ .

### Simulation Result Versus Testing Result

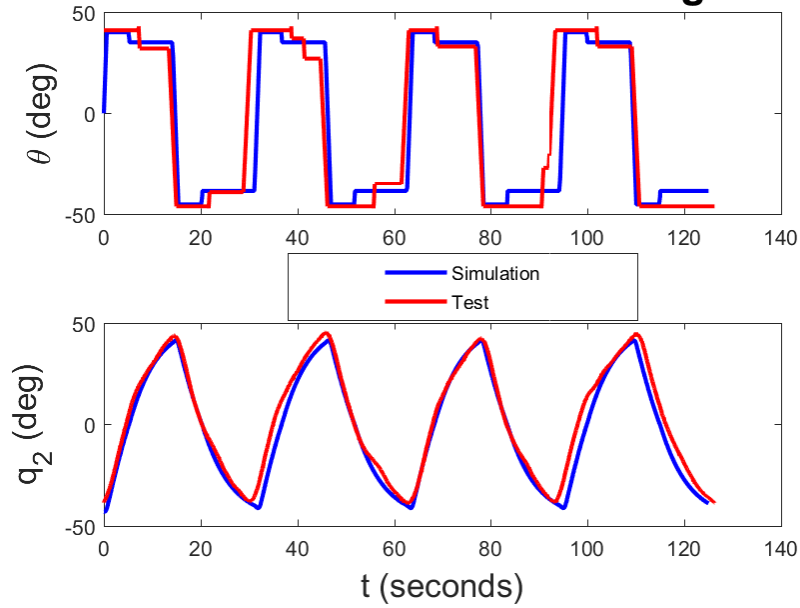


Figure 47: Testing and simulation comparison for Test 35 with a current velocity of  $1.5 \frac{ft}{s}$ .

### Simulation Result Versus Testing Result

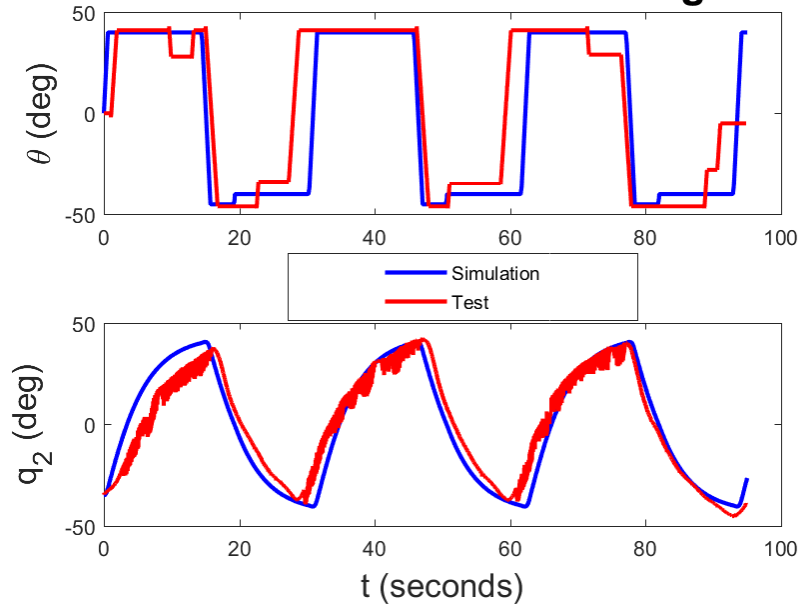


Figure 48: Testing and simulation comparison for Test 45 with a current velocity of  $2.0 \frac{ft}{s}$ .

### Simulation Result Versus Testing Result

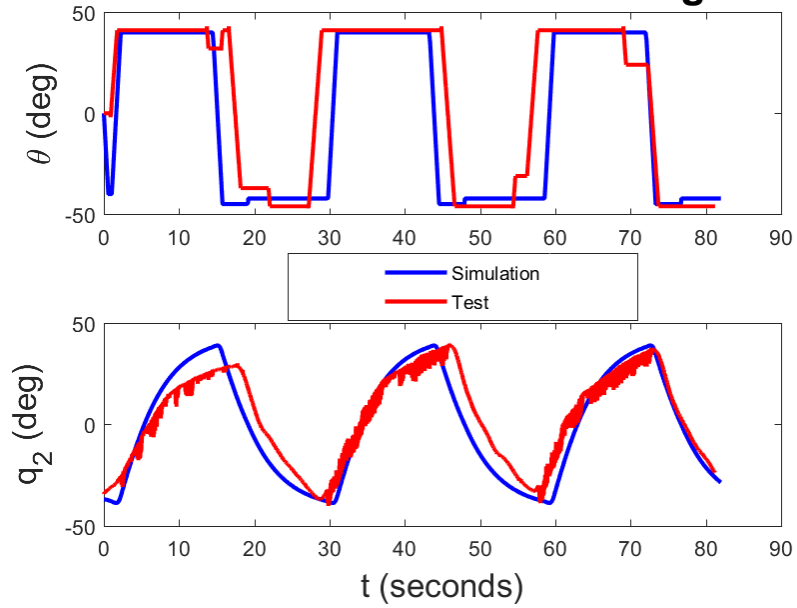


Figure 49: Testing and simulation comparison for Test 46 with a current velocity of  $2.0 \frac{ft}{s}$ .

## 5.5 Sensitivity Study

To study the effect of simulation parameters on the simulation result, the simulation parameters were varied for the well-correlated Test 35, shown in Figure 47. When parameters of the system are changed, the runs should no longer correlate well. If parameters were drastically changed and the simulation still matched, it would show that the simulation is matching test results by accident. Table 9 lists the 11 graphs shown in the sensitivity study of Figures 50 - 60 and what is varied in each one.

*Table 9: Summary of sensitivity study simulation runs*

Study Number	Variation
0	None (baseline run, identical to Figure 47)
1	Boat mass $\times 5$
2	Boat mass and tether density $\times 5$
3	Tether length $\times 3$
4	Current speed $\times 2$
5	Current speed $\times 0.5$
6	$q_{2,\text{lim}} = 20^\circ$ instead of $40^\circ$
7	$q_{2,\text{lim}} = 30^\circ$ instead of $40^\circ$
8	$q_{2,\text{lim}} = 45^\circ$ instead of $40^\circ$
9	Hull drag $\times 0.5$
10	Boat size $\times 1.2$

As would be expected, increasing size and mass of system components causes the system to react more slowly, stretching out the simulation curve with respect to the testing curve. Increasing the current speed causes faster reversing motion, fitting more periods in the same time span. Lowering the current speed causes slower reversing motion, fitting less periods in the same time span. Lowering the limit  $q_{2,\text{lim}}$  compresses the curve along both the  $q_2$  and  $t$  axes, while raising  $q_{2,\text{lim}}$  stretches the graph in the same way. Finally, lowering drag causes faster reversing motion, as expected. The sensitivity study shows that the simulation reacts as expected to changes in input parameters, further validating the correlation between the tests and the simulations.



## Simulation Result Versus Testing Result

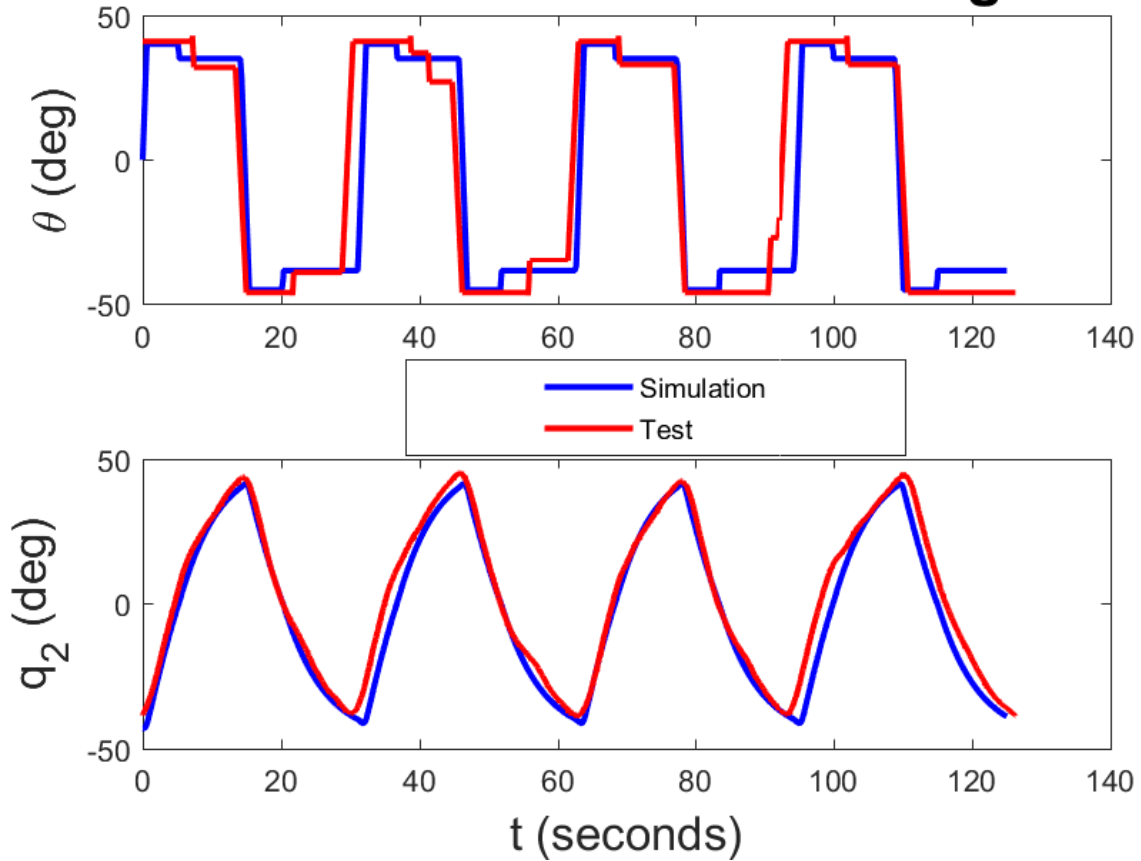


Figure 50: Sensitivity Study 0 - Baseline

### Simulation Result Versus Testing Result

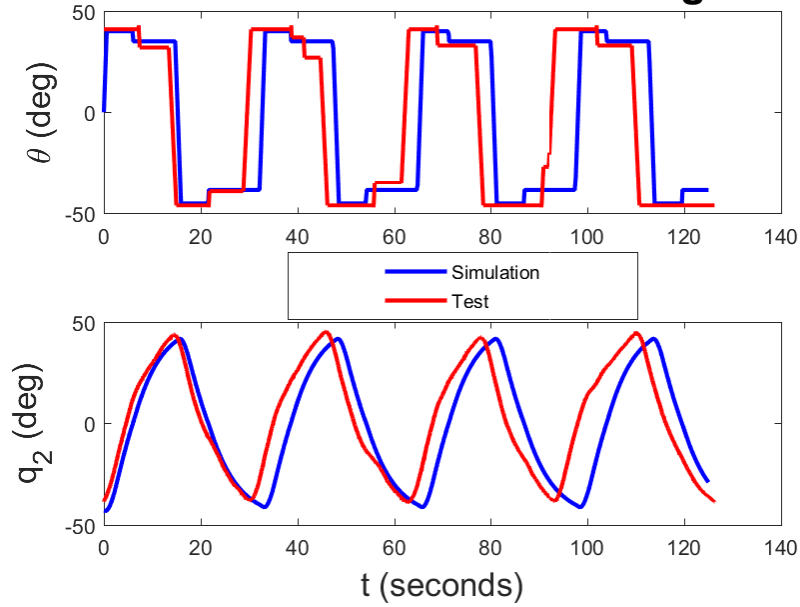


Figure 51: Sensitivity Study 1 - Boat mass  $\times 5$

### Simulation Result Versus Testing Result

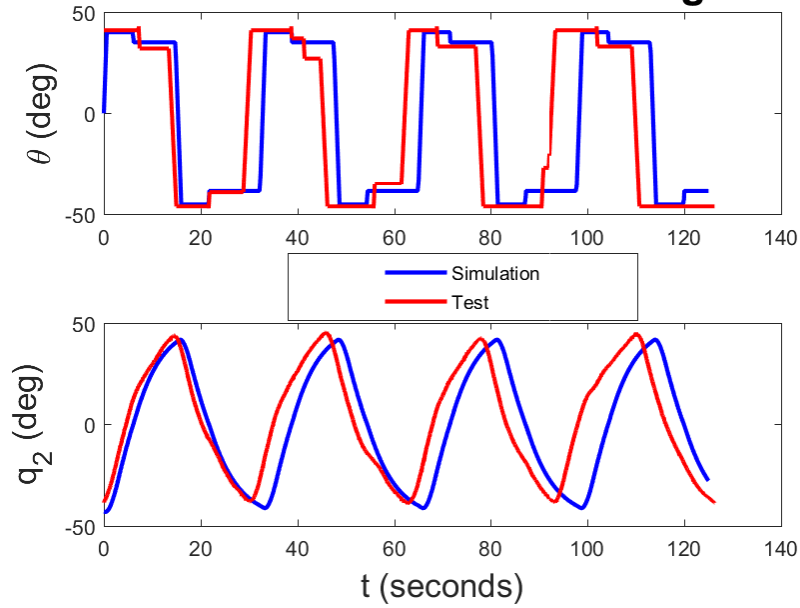


Figure 52: Sensitivity Study 2 - Boat mass and tether density  $\times 5$

### Simulation Result Versus Testing Result

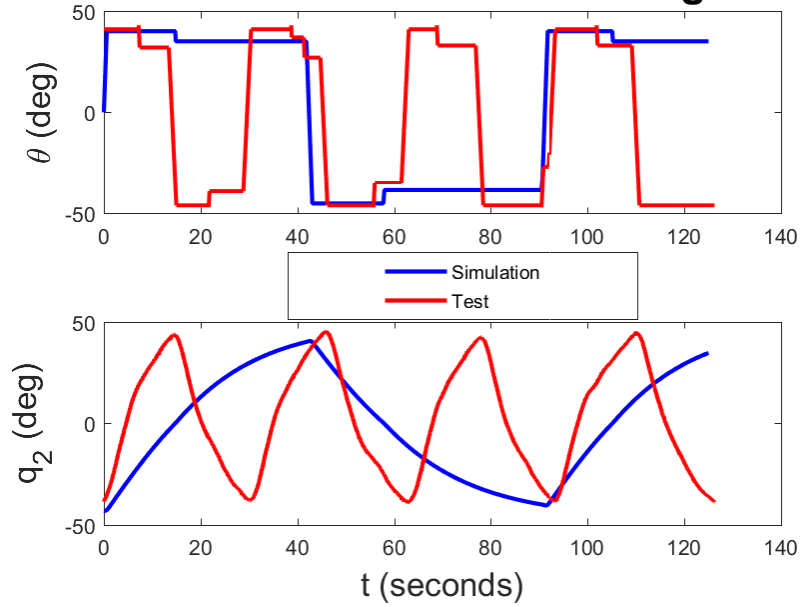


Figure 53: Sensitivity Study 3 - Tether length  $\times 3$

### Simulation Result Versus Testing Result

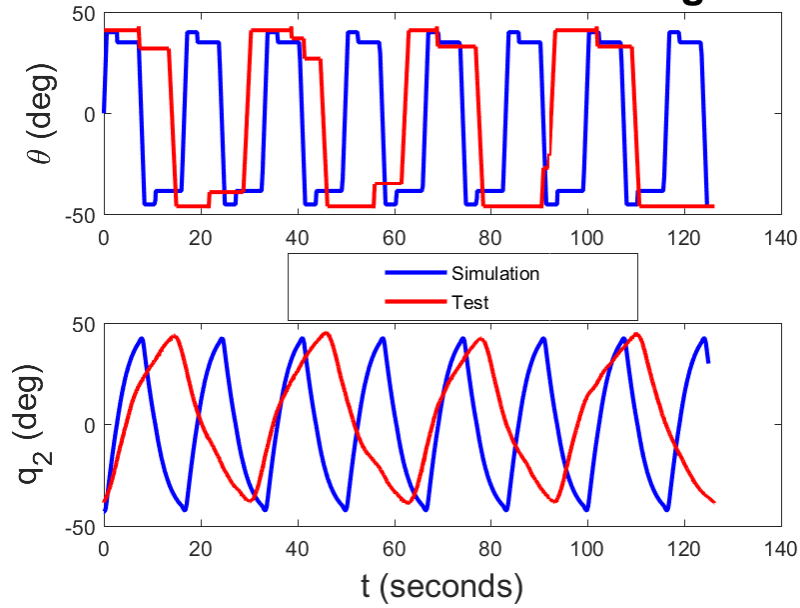


Figure 54: Sensitivity Study 4 - Current speed  $\times 2$

### Simulation Result Versus Testing Result

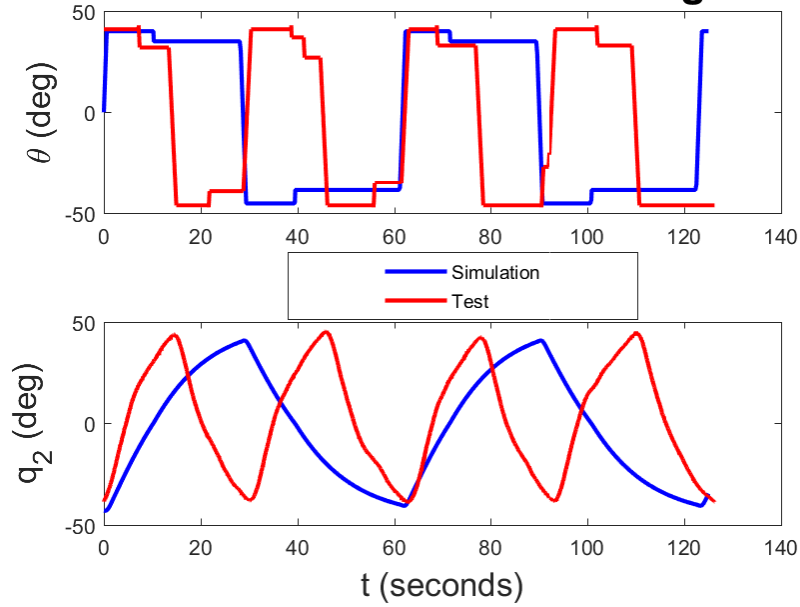


Figure 55: Sensitivity Study 5 - Current speed  $\times 0.5$

### Simulation Result Versus Testing Result

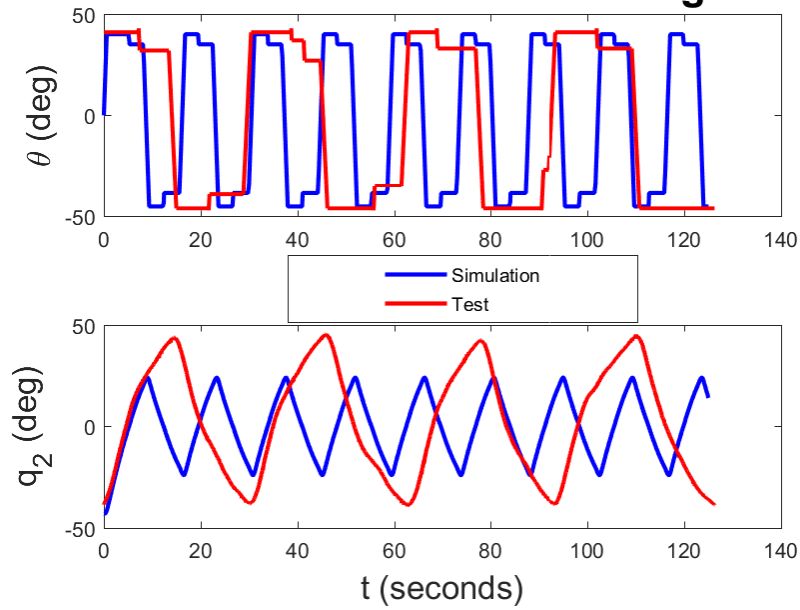


Figure 56: Sensitivity Study 6 -  $q_{2,lim} = 20^\circ$  instead of  $40^\circ$

### Simulation Result Versus Testing Result

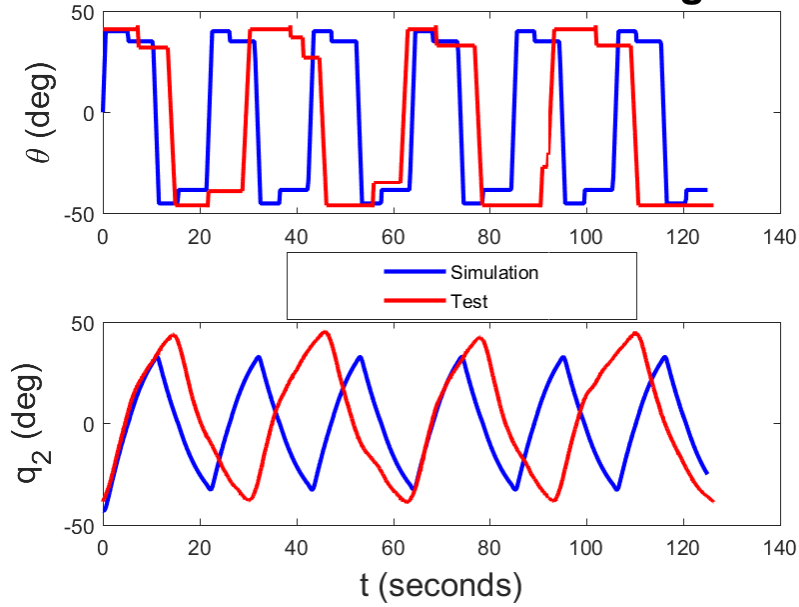


Figure 57: Sensitivity Study 7 -  $q_{2,lim} = 30^\circ$  instead of  $40^\circ$

### Simulation Result Versus Testing Result

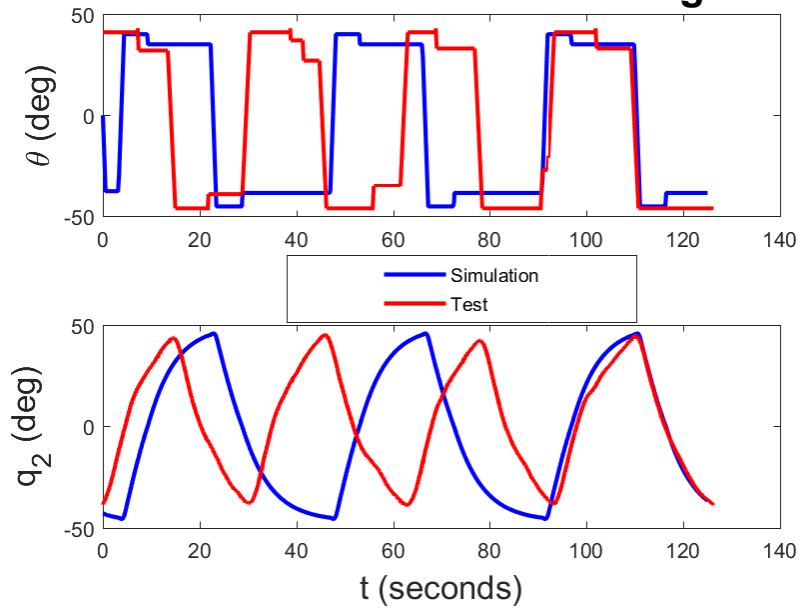


Figure 58: Sensitivity Study 8 -  $q_{2,lim} = 45^\circ$  instead of  $40^\circ$

### Simulation Result Versus Testing Result

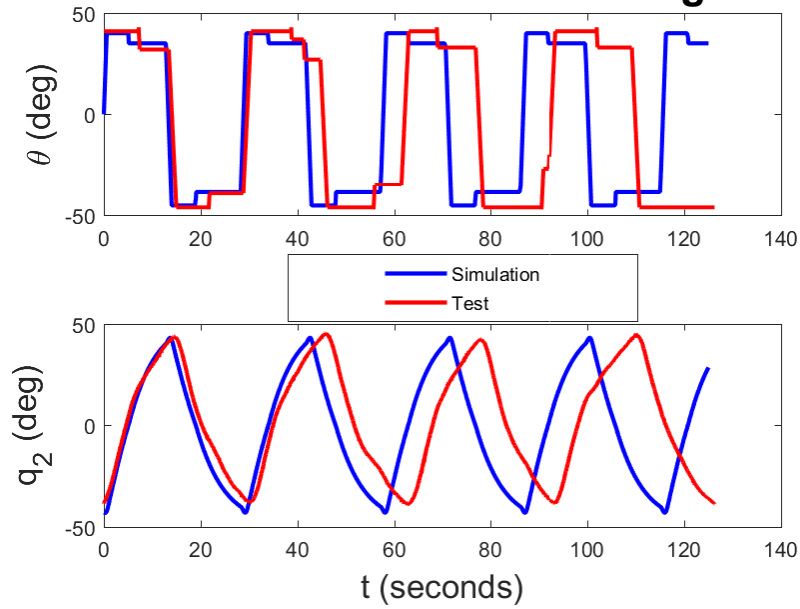


Figure 59: Sensitivity Study 9 - Hull drag  $\times 0.5$

### Simulation Result Versus Testing Result

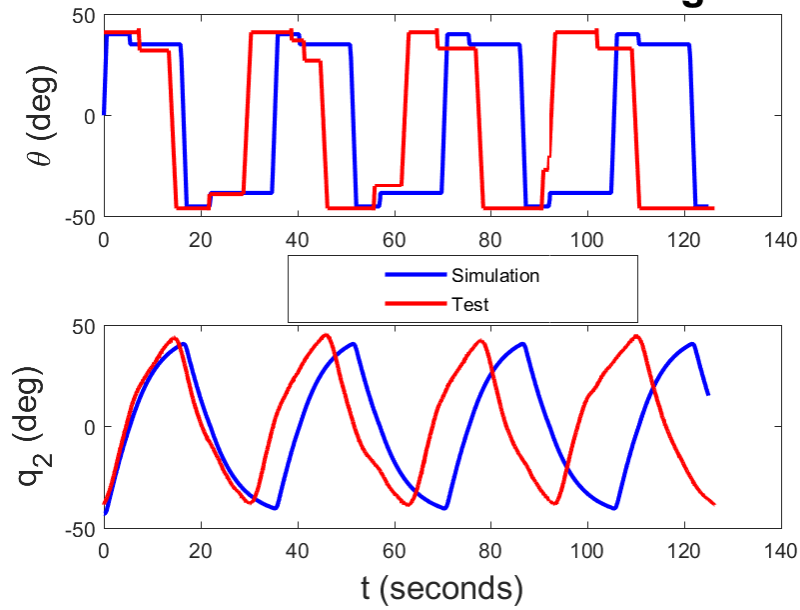


Figure 60: Sensitivity Study 10 - Boat size  $\times 1.2$

## 5.6 Scaled-Up Simulation Results and Comparison

As previously mentioned, the utility in simulations comes in their ability to predict large-scale characteristics of a SUSK system. Using Table 5 as a reference for the scaling, two simulation runs, one for the scale-model size system and one for the full size system, can be directly compared. The numerical values for forces, torques, and power will be orders of magnitude different, but the general shape of the graphs and characteristic of the system can be compared to assure no drastic changes when the simulation is scaled-up. A scaled-up simulation based on test run 35, the same test run used for the sensitivity study, is shown in Figures 61 - 66.

Although the scaled-up system has approximately five times the period of the smaller system, the shape of the graphs is very similar. Parameters that were not affected in the scaling were the limit  $q_{2,\text{lim}}$  and the  $\theta$  values that the wing was trimmed at. These would also need to be considered in the future because they would need to be different between the small and large systems. Overall, the simulations suggest that future work should be done to further validate and utilize these simulations with future work on the physical SUSK system.

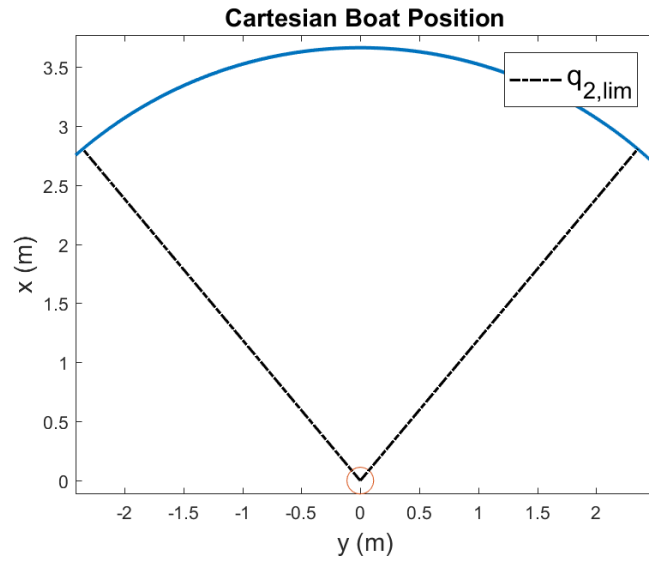


Figure 61: Small-scale simulation comparison cartesian output.

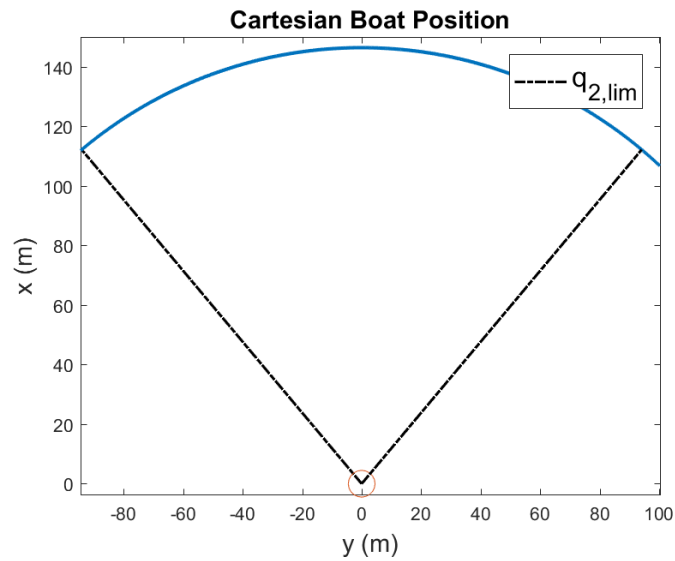


Figure 62: Large-scale simulation comparison cartesian output.



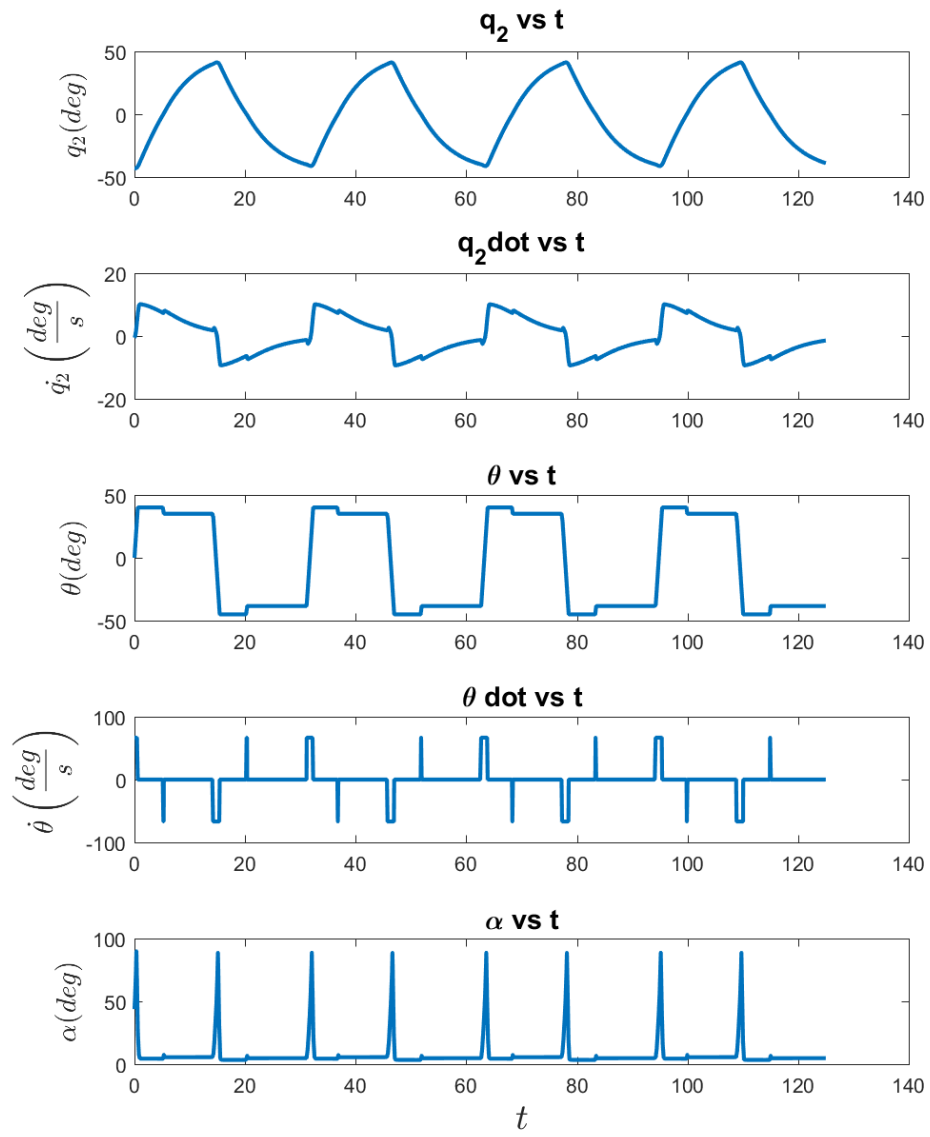


Figure 63: Small-scale simulation comparison angular data output.

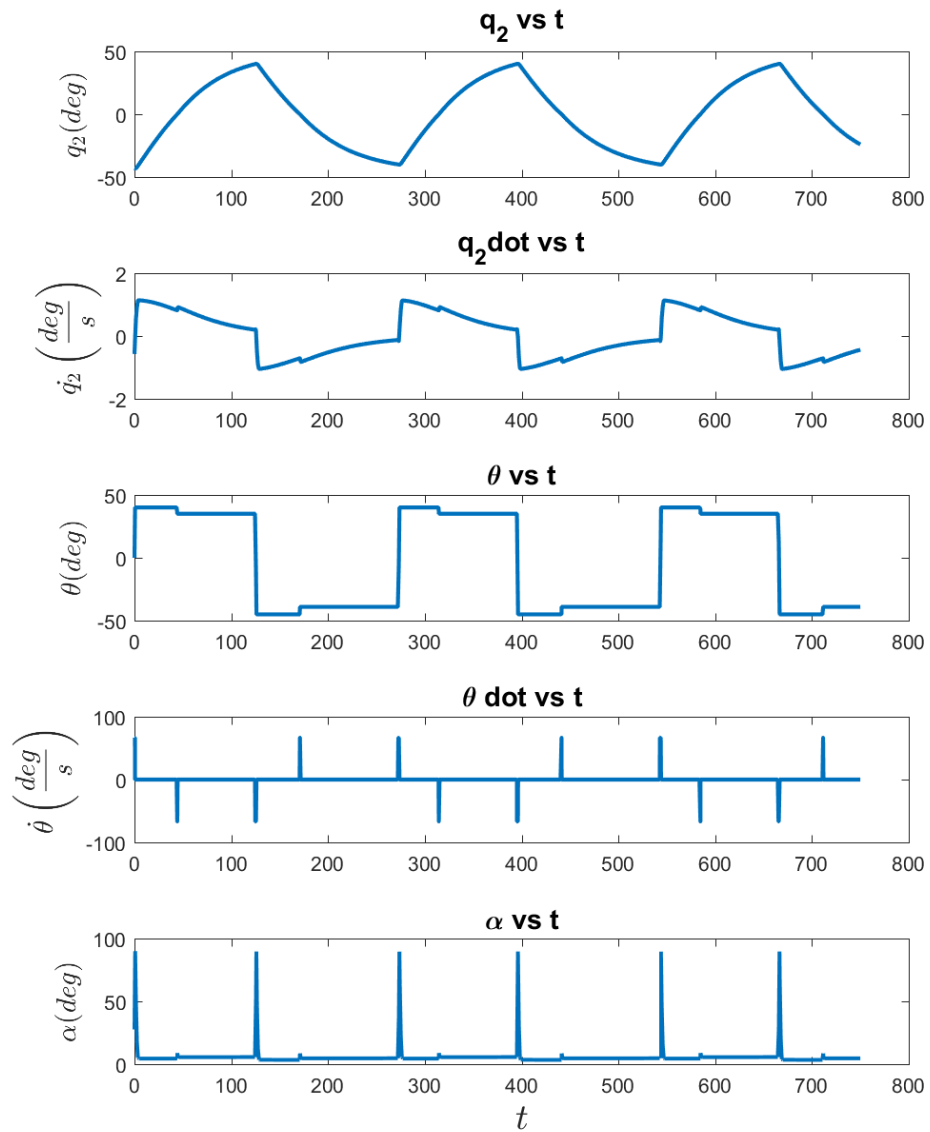


Figure 64: Large-scale simulation comparison angular data output.

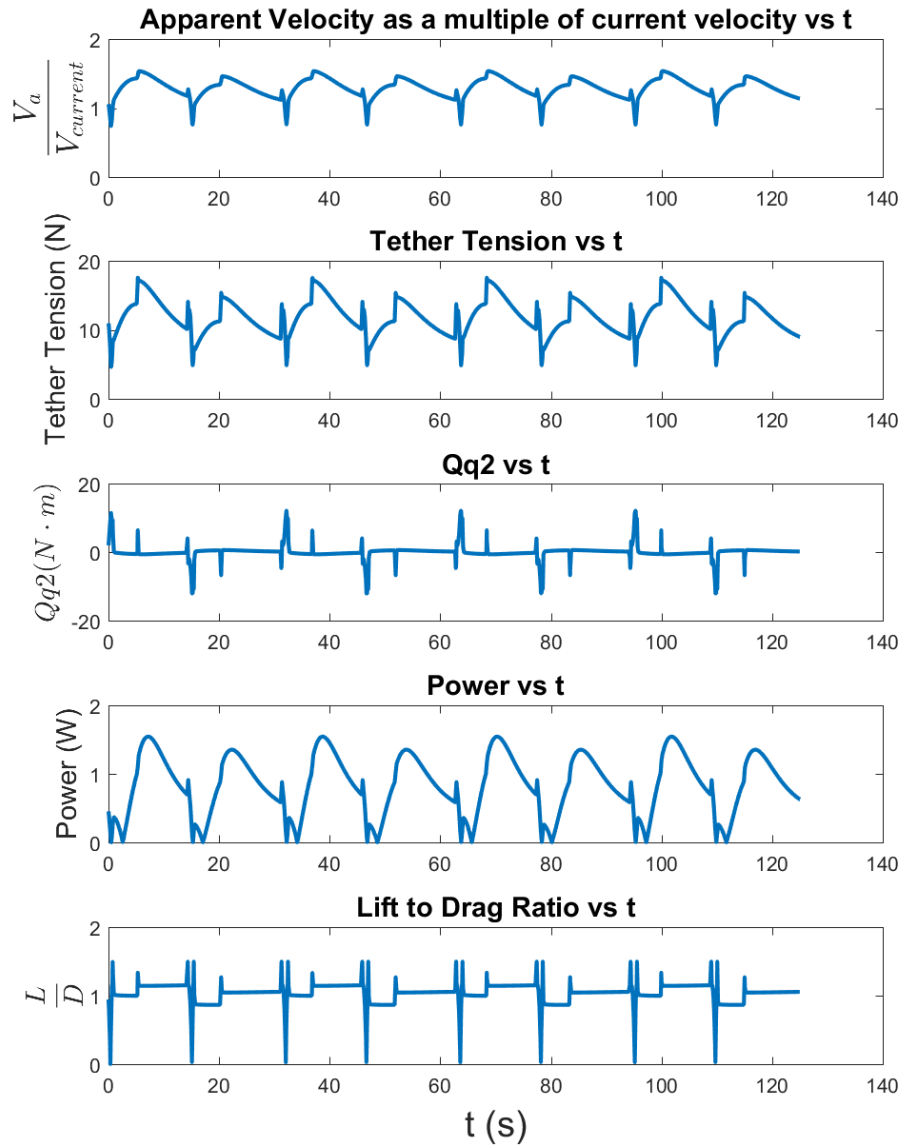


Figure 65: Small-scale simulation comparison miscellaneous data output.

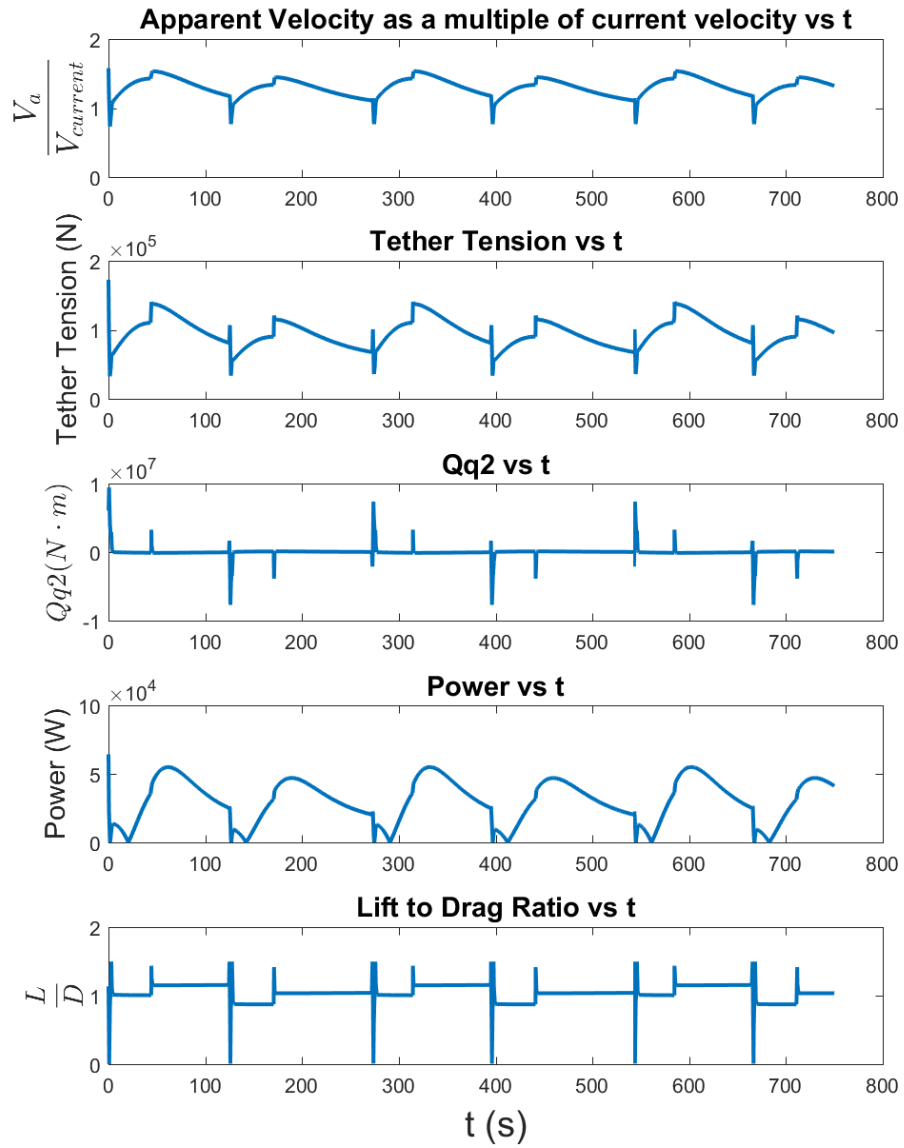


Figure 66: Large-scale simulation comparison miscellaneous data output.

## Chapter 6: Discussion and Conclusions

---

The goals of this project given in Section 1.5 were met successfully during the course of this project. The preliminary SUSK system was brought from concept to working scale-model during the project. The hull and wing design possibilities were studied and the entire system was modeled in CAD software. The system was made to be compatible with previous TUSK hardware, particularly the tether and gimbal setup, and the new control system that was designed is backward-compatible with the WPI TUSK.

A prototype of the SUSK was fabricated using mainly 3D printing and manufacturing resources at WPI, and additional components were produced for temporary modification of existing hardware to better suit the SUSK system.

Scale model-tests were completed both in the WPI swimming pool and the 20 ft wide  $\times$  10 ft deep water tunnel at Alden Research Laboratory (ARL) in Holden, MA. The initial pool tests proved to be good at measuring the general motion of the system, which allowed us to verify the hypothesized movement patterns. The ARL testing gave us a platform to control the external parameters of the testing, such as current speed. These long-term tests generated data that was used to confirm not only the accuracy of the simulations, but the feasibility of the system as a whole in producing tethered energy.

The tests conducted at Alden Labs showed that the SUSK boat traveled at approximately two times the current velocity for current speeds of approximately  $1 \frac{\text{ft}}{\text{s}}$  -  $2 \frac{\text{ft}}{\text{s}}$ . The tests also showed that the cross-current motion of the SUSK generated a higher voltage for the turbine, but due to the rotation issue of the turbine, we were not able to get an exact number on how much of a voltage increase there was. The fixed angle turbine, however, was still able to generate a larger voltage than a stationary turbine. This shows that the SUSK idea is effective at additional power generation in all but the fastest current speed test of  $2.0 \frac{\text{ft}}{\text{s}}$ . Sufficiently fast current speeds caused buoyancy issues for the hull, which prevented further testing at faster speeds.

Dynamic simulations were developed for the SUSK system, and they were compared to the ARL testing results. Test data and simulation runs showed good agreement, allowing for future work to be done studying the possibility of a scaled-up SUSK system.

The final chapter will outline future suggestions from this project's team that will assist a future team aiming to improve the SUSK system.

Overall, this project was a success in that it met its goals and demonstrated that the SUSK system has the potential to be better than stationary energy harvesting methods and as good, if not better, than other tethered energy systems.

# Chapter 7: Future Work

---

After completing the MQP testing, the team created a list of recommendations for future teams. This list contains things that the team wishes they did differently, things they wish they knew before starting, and general suggestions for any future work done.

- Ensuring that all load-bearing parts are strong enough and stiff enough to not break when under stress
- Increasing the buoyancy of the system to allow for faster current test speeds, either by reducing total weight for a given volume or increasing total volume for a given weight
- Redesigning the turbine assembly to account for the difficulty in turning during testing
- Rethink the slip ring mechanism and assembly to reduce complexity and increase reliability
- Redesign the wing shaft assembly to easier integrate to the servos, allowing for more consistent and rigid control
- For a finalized design, more protection for the wiring on the SUSK itself will be needed to both improve the looks of the system, but also to prevent snagging and water damage
- Create a new method for preventing tether rotation when used for the SUSK, and ensure that it is strong enough to handle the torques it will have applied to it
- Create a new method to attach the SUSK to the tether that does not rely on small 3D printed parts to hold it together, possibly multiple attachment points to increase overall rigidity
- Experiment with different wing planform shapes, chordlengths, and spans study effects on system performance
- Replace the carbon fiber tether with a flexible cable that would be used in a full-scale system

With these recommendations for future work, the SUSK system can be improved from this project, which proved it a feasible technology in tethered energy.

# Appendix A: XFLR5 Wing Testing Wind Tunnel

---

Shown in Tables 11 - 13 is raw force and moment data from the wind tunnel force balance. Because of limits on angle of attack in the wind tunnel, the airfoil was tested upside down. Measurement were taken from  $0^\circ$  to  $-18^\circ$  for angle of attack upside down. The conversion for axial and normal forces measured at negative angle of attack to lift and drag forces is

$$\begin{aligned} L(\alpha) &= -N \cos(-\alpha) - A \sin(-\alpha) \\ D(\alpha) &= -N \sin(-\alpha) + A \cos(-\alpha) \end{aligned} \tag{A.1}$$

From there, the data in Table 10 was used to nondimensionalize the lift and drag data by Equation 5.5.

*Table 10: Data from wind tunnel tests used to nondimensionalize lift and drag results*

Paramter	Value
Density	$0.0023769 \frac{\text{slg}}{\text{ft}^3}$
$c$	4 in
$b$	7.75 in
$S$	$31 \text{ in}^2$
$V$	$98.43 \frac{\text{ft}}{\text{s}}$
Moment Arm of Force Balance	3.9 in



Table 11: Small-scale wind tunnel testing data for Airfoil 12 (candidate optimal airfoil)

Angle (Degrees)	Axial Force (lbs)	Normal Force (lbs)	Moment (in·lbs)
0	-0.16	-1.55	-7.03
-1	-0.08	-1.81	-7.9
-2	-0.08	-2	-9.08
-3	-0.08	-2.22	-10
-4	-0.12	-2.38	-10.78
-5	-0.18	-2.58	-11.76
-6	-0.22	-2.72	-12.55
-7	-0.27	-2.93	-13.42
-8	-0.33	-3.08	-14.14
-9	-0.41	-3.17	-14.76
-10	-0.44	-3.21	-15.15
-11	-0.34	-3.15	-15.05
-12	-0.38	-3.14	-14.55
-13	-0.43	-3.12	-14.68
-14	-0.47	-3.1	-14.8
-15	-0.52	-3.08	-14.82
-16	-0.54	-3.06	-14.92
-17	-0.58	-3.04	-15.06
-18	-0.71	-2.96	-15.39

Table 12: Small-scale wind tunnel testing data for Airfoil 3 (less cambered than candidate optimal airfoil)

Angle (Degrees)	Axial Force (lbs)	Normal Force (lbs)	Moment (in · lbs)
0	0.17	-0.62	-1.73
1	0.16	-0.68	-2.41
2	0.14	-0.93	-3.42
3	0.12	-1.17	-4.4
4	0.08	-1.38	-5.44
5	0.05	-1.55	-6.28
6	0.02	-1.73	-7
7	-0.04	-1.92	-8
8	-0.09	-2.05	-8.65
9	-0.14	-2.17	-9.3
10	-0.19	-2.31	-10
11	-0.26	-2.42	-10.7
12	-0.31	-2.5	-11.2
13	-0.37	-2.6	-11.86
14	-0.42	-2.62	-12.2
15	-0.46	-2.7	-12.46
16	-0.5	-2.7	-12.72
17	-0.51	-2.67	-12.7
18	-0.55	-2.69	-12.76

Table 13: Small-scale wind tunnel testing data for Airfoil 10 (thinner than candidate optimal airfoil)

Angle (Degrees)	Axial Force (lbs)	Normal Force (lbs)	Moment (in · lbs)
0	0.12	-0.58	-2
1	0.14	-0.9	-2.71
2	0.12	-1.08	-3.64
3	0.07	-1.43	-5.02
4	0.04	-1.7	-6.28
5	0.02	-1.84	-6.78
6	-0.04	-2.1	-7.95
7	-0.1	-2.32	-8.95
8	-0.15	-2.41	-9.6
9	-0.21	-2.53	-10.2
10	-0.27	-2.64	-10.85
11	-0.3	-2.7	-11.31
12	-0.33	-2.8	-11.8
13	-0.36	-2.96	-12.6
14	-0.34	-3.19	-13.46
15	Vibrating, did not get data		
16	Vibrating, did not get data		
17	Vibrating, did not get data		
18	Vibrating, did not get data		



# Appendix C: Arduino Code for Servo Control and Data Logging

---

The code here was used to control the servos of the SUSK wing and read data during test runs.

```
#include <Servo.h>
#include <SD.h>
#include <time.h>

File myFile;

const int buttonPin = 40;
const int buttonPin2 = 42;
int buttonState = 0;
int buttonState2 = 0;

Servo servoA;
int position = 90;

void setup() {
  Serial.begin(9600);
  servoA.attach(7);
  pinMode(buttonPin, INPUT);
  pinMode(buttonPin2, INPUT);

  Serial.print("Initializing SD card...");

  pinMode(4, OUTPUT);

  if (!SD.begin(4)) {
    Serial.println("initialization failed!");
    return;
  }
  Serial.println("initialization done.");

  myFile = SD.open("susksDATA.txt", FILE_WRITE);

  if (myFile) {
    myFile.println(minute());
  } else {
    Serial.println("error opening test.txt");
  }
}
```

```

    }
}

void loop() {

    // myFile = SD.open("sus&kDATA.txt", FILE_WRITE);

    int q2 = analogRead(A0);
    int q1 = analogRead(A1);
    int tPower = analogRead(A3);
    int servoApos = servoA.read();
    myFile.print(q2);
    myFile.print(", ");
    myFile.print(q1);
    myFile.print(", ");
    myFile.print(servoApos);
    myFile.print(", ");
    myFile.println(tPower);
    Serial.print(q2);
    Serial.print(", ");
    Serial.print(q1);
    Serial.print(", ");
    Serial.print(servoApos);
    Serial.print(", ");
    Serial.println(tPower);
    delay(15);

    buttonState = digitalRead(buttonPin);
    buttonState2 = digitalRead(buttonPin2);

    if (buttonState == HIGH && position < 135) {
        servoA.write(position++);
    }

    if (buttonState2 == HIGH && position > 45) {
        servoA.write(position--);
    }

    if (buttonState == HIGH && buttonState2 == HIGH) {
        myFile.close();
    }
}

```

## Appendix D: Table of Test Runs from Alden Research Laboratory

---

Test #	Speed (ft/s)	Notes
20	1.0	bad
21	1.0	Turbine fixed angled $\sim 30^\circ$ CCW towards tether side of boat
22	1.0	same
23	1.0	same
24	1.0	same
25	1.0	same
26	1.0	same
27	1.0	same
28	1.0	same
29	1.0	same
30	1.0	same
31	1.5	bad
32	1.5	same
33	1.5	same
34	1.5	same
35	1.5	same
36	1.5	same
37	1.5	same
38	1.5	same
39	1.5	same
40	1.5	same
41	1.5	same
42	1.5	same
43	2.0	same, boat submerges a bit at high velocity
44	2.0	same, but turbine angled -30 degrees CW towards non-tether side from current
45	2.0	same
46	2.0	long test with maintenance visible towards end
47	0.5	normal test
48	0.5	same
49	0.5	same
50	0.5	No Boat Movement
51	0.5	same
52	0.5	same
53	0.5	bad
54	1.0	No Boat Movement
55	1.0	same
56	1.0	same
57	1.5	No Boat Movement
58	1.5	same
59	1.5	same
60	2.0	No Boat Movement
61	2.0	same
62	2.0	same
63	2.0	bad
64	2.0 - 0	No Movement, 2.0 ft/s to 0.0 ft/s

# Appendix E: TUSK Equations of Motion

---

Equations of motion presented below are taken from [3]. For the purposes of this Appendix only, take  $\phi = q_4$ ,  $\theta = q_5$ , and  $\psi = q_6$ .

$$\ddot{q}_1 = - \left[ -Q_{q_1} + mg \cos(q_2) \cos(q_3) + \frac{1}{2} [2g\rho_c \cos(q_2) \cos(q_3)q_1 + \rho_c \dot{q}_1^2 - 2mq_1 \dot{q}_2^2 - \rho_c q_1^2 \dot{q}_2^2 - q_1 \cos^2(q_2)(2m + \rho_c q_1) \cdot \dot{q}_3^2] \right] \cdot \frac{1}{m + \rho_c q_1} \quad (\text{E.1})$$

$$\ddot{q}_2 = -3 \cdot \left[ -Q_{q_2} - g \cos(q_3)q_1 [-2m(RB) + (\rho_c - \rho_b)q_1] \cdot \frac{\sin(q_2)}{2} + q_2(2m + \rho_c q_1)\dot{q}_1\dot{q}_2 + \frac{1}{6} [q_1^2(3m + \rho_c q_1) \sin(2q_2)\dot{q}_3^2] \right] \cdot \frac{1}{q_1^2(3m + \rho_c q_1^2)} \quad (\text{E.2})$$

$$\ddot{q}_3 = -3 \cdot \sec^2(q_2) \left[ -Q_{q_3} - g \cos(q_2)q_1 [-2m(RB) + (\rho_c - \rho_b)q_1] \cdot \frac{\sin(q_3)}{2} + q_1 \cos^2(q_2)(2m + \rho_c q_1)\dot{q}_1\dot{q}_3 - 2 \cos(q_2)q_1^2(3m + \rho_c q_1)\dot{q}_2\dot{q}_3 \frac{\sin(q_2)}{3} \right] \cdot \frac{1}{q_1^2(3m + \rho_c q_1)} \quad (\text{E.3})$$

$$\begin{aligned} \ddot{\phi} = & - \left[ Q_\phi - J_1 \cos(\theta)\dot{\psi}\dot{\theta} - (J_2 - J_3)[\cos(\theta) \sin(\phi)\dot{\phi} + \cos(\phi)\dot{\theta}] \cdot [\cos(\theta) \cos(\phi)\dot{\psi} + \sin(\phi)\dot{\theta}] \right] \\ & \cdot \frac{1}{J_1} \left\{ \sin(\theta) \left[ -J_1(J_2 - J_3) \cos(\theta) \sin(2\phi) \cdot \left[ -Q_\theta \right. \right. \right. \\ & + \left( [-2J_1 + J_2 + J_3 + (-J_2 + J_3) \cos(2\phi)] \sin(2\theta)\dot{\psi}^2 \cdot \frac{1}{4} \right) + \dot{\phi}((J_1 + (J_2 - J_3) \cos(\theta) \cos(2\phi))\dot{\psi} \\ & \left. \left. \left. + (-J_2 + J_3) \sin(2\phi)\dot{\theta} \right] \cdot \frac{1}{2} + [J_2 + J_3 + (J_2 - J_3) \cos(2\phi)] \cdot \frac{1}{2} \cdot \left[ J_1 \sin(\theta) \left[ -Q_\phi \right. \right. \right. \right. \\ & - J_1 \cos(\theta)\dot{\psi}\dot{\theta} - (J_2 - J_3)[\cos(\theta) \sin(\phi)\dot{\psi} + \cos(\phi)\dot{\theta}][\cos(\theta) \cos(\phi)\dot{\psi} - \sin(\phi)\dot{\theta}] \left. \left. \left. \right] + J_1 \left[ -Q_\psi \right. \right. \right. \\ & + \frac{1}{2} [2J_1 - J_2 - J_3 + (J_2 - J_3) \cos(2\phi)] \sin(2\theta)\dot{\psi}\dot{\theta} + \frac{1}{2} (-J_2 + J_3) \sin(2\phi) \sin(\theta)\dot{\theta}^2 + \cos(\theta)\dot{\phi}(-J_1\dot{\theta} \\ & \left. \left. \left. + (J_2 - J_3)(\cos(\theta) \sin(2\phi)\dot{\psi} + \cos(2\phi)\dot{\theta})) \right] \right] \right] \right\} \cdot \left\{ -J_1(J_2 - J_3)^2 \cos^2(\theta) \sin^2(2\phi) \cdot \frac{1}{4} \right. \\ & + [J_2 + J_3 + (J_2 - J_3) \cos(2\phi)] \cdot \left( J_1 \left[ [2J_1 + J_2 + J_3 + (-J_2 + J_3) \cos(2\phi)] \cdot \frac{1}{4} \right. \right. \\ & \left. \left. + [-2J_1 + J_2 + J_3 + (-J_2 + J_3) \cos(2\phi)] \cos(2\theta) \cdot \frac{1}{4} \right] - J_1^2 \sin^2(\theta) \right) \cdot \frac{1}{2} \left. \right\}^{-1} \quad (\text{E.4}) \end{aligned}$$



$$\begin{aligned}
\ddot{\theta} = & -2 \cdot \left[ -Q_\theta + \frac{1}{4} [(-2J_1 + J_2 + J_3 + (-J_2 + J_3) \cos(2\phi)) \sin(2\theta) \dot{\psi}^2] \right. \\
& + \dot{\phi} [J_1 + (J_2 - J_3) \cos(2\phi)] \cos(\theta) \dot{\psi} + (-J_2 + J_3) \sin(2\phi) \dot{\theta} \left. \right] \cdot [J_2 + J_3 + (J_2 - J_3) \cos(2\phi)]^{-1} \\
& + \left\{ (J_2 - J_3) \cos(\theta) \sin(2\phi) \cdot \left[ - \left[ J_1 (J_2 - J_3) \cos(\theta) \sin(2\theta) \cdot \left[ -Q_\theta + \frac{1}{4} [(-2J_1 + J_2 + J_3 \right. \right. \right. \right. \\
& \quad \left. \left. \left. + (-J_2 + J_3) \cos(2\phi)) \sin(2\theta) \dot{\psi}^2 \right] + \dot{\phi} ([J_1 + (J_2 - J_3) \cos(2\phi)] \cos(\theta) \dot{\psi} \right. \right. \right. \\
& \quad \left. \left. + (-J_2 + J_3) \sin(2\phi) \dot{\theta} \right] \right] \cdot \frac{1}{2} + \left[ [J_2 + J_3 + (J_2 - J_3) \cos(2\phi)] J_1 \sin(\theta) [-Q_\phi - J_1 \cos(\theta) \dot{\psi} \dot{\theta} \right. \right. \\
& \quad \left. \left. - (J_2 - J_3) [\cos(\theta) \sin(\phi) \dot{\psi} + \cos(\phi) \dot{\theta}] [\cos(\theta) \cos(\phi) \dot{\psi} - \sin(\phi) \dot{\theta}] \right] \right. \\
& + J_1 \left( -Q_\psi + [2J_1 - J_2 - J_3 + (J_2 - J_3) \cos(2\phi)] \sin(2\theta) \dot{\psi} \dot{\theta} \cdot \frac{1}{2} + [(-J_2 + J_3) \sin(2\phi) \sin(\theta) \dot{\theta}^2] \cdot \frac{1}{2} \right. \\
& \quad \left. + \cos(\theta) \dot{\phi} [-J_1 \dot{\theta} [-J_1 \dot{\theta} + (J_2 - J_3) [\cos(\theta) \sin(2\phi) \dot{\psi} + \cos(2\phi) \dot{\theta}]] \right) \cdot \frac{1}{2} \left. \right\} \cdot \left\{ [J_2 + J_3 \right. \\
& \quad \left. + (J_2 - J_3) \cos(2\phi)] \left[ -J_2 (J_2 - J_3)^2 \cos^2(\theta) \sin^2(2\phi) \cdot \frac{1}{4} \right. \right. \\
& \quad \left. \left. + [J_2 + J_3 + (J_2 - J_3) \cos(2\phi)] \cdot \left( J_1 \left[ [2J_1 + J_2 + J_3 + (-J_2 + J_3) \cos(2\phi)] \cdot \frac{1}{4} \right. \right. \right. \right. \\
& \quad \left. \left. \left. + [(-2J_1 + J_2 + J_3 + (-2J_2 + J_3) \cos(2\phi)) \cos(2\theta) \cdot \frac{1}{4}] - J_1^2 \sin^2(\theta) \right) \cdot \frac{1}{2} \right] \right\}^{-1} \\
& \tag{E.5}
\end{aligned}$$

$$\begin{aligned}
\ddot{\psi} = & - \left\{ - \left[ J_1 (J_2 - J_3) \cos(\theta) \sin(2\phi) \left[ -Q_\theta + \frac{1}{4} [(-2J_1 + J_2 + J_3 \right. \right. \right. \right. \\
& \quad \left. \left. \left. + (-J_2 + J_3) \cos(2\phi)) \sin(2\theta) \dot{\psi}^2 \right] + \dot{\phi} ([J_1 + (J_2 - J_3) \cos(2\phi)] \cos(\theta) \dot{\psi} \right. \right. \right. \\
& \quad \left. \left. + (-J_2 + J_3) \sin(2\phi) \dot{\theta} \right] \right] \cdot \frac{1}{2} + [J_2 + J_3 + (J_2 - J_3) \cos(2\phi)] \cdot \left( J_1 \sin(\theta) (-Q_\phi - J_1 \cos(\theta) \dot{\psi} \dot{\theta} \right. \\
& \quad \left. - (J_2 - J_3) [\cos(\theta) \sin(\phi) \dot{\psi} + \cos(\phi) \dot{\theta}] [\cos(\theta) \cos(\phi) \dot{\psi} - \sin(\phi) \dot{\theta}] \right) \\
& \quad \left. + J_1 \left( -Q_\psi + [2J_1 - J_2 - J_3 + (J_2 - J_3) \cos(2\phi)] \sin(2\theta) \dot{\psi} \dot{\theta} \cdot \frac{1}{2} \right. \right. \\
& \quad \left. \left. + [(-J_2 + J_3) \sin(2\phi) \sin(\theta) \dot{\theta}^2] \cdot \frac{1}{2} + \cos(\theta) \dot{\phi} [-J_1 \dot{\theta} + (J_2 - J_3) [\cos(\theta) \sin(2\phi) \dot{\psi} \right. \right. \\
& \quad \quad \left. \left. + \cos(2\phi) \dot{\theta}]] \right) \right) \cdot \frac{1}{2} \left. \right\} \cdot \left\{ -J_1 (J_2 - J_3)^2 \cos^2(\theta) \sin^2(2\phi) \cdot \frac{1}{4} \right. \\
& \quad \left. + [J_2 + J_3 (J_2 - J_3) \cos(2\phi)] \cdot \left( J_1 \left[ [2J_1 + J_2 + J_3 + (-J_2 + J_3) \cos(2\phi)] \cdot \frac{1}{4} \right. \right. \right. \\
& \quad \left. \left. \left. + [(-2J_1 + J_2 + J_3 + (-J_2 + J_3) \cos(2\phi)) \cos(2\theta) \cdot \frac{1}{4}] - J_1^2 \sin^2(\theta) \right) \cdot \frac{1}{2} \right] \right\}^{-1} \\
& \tag{E.6}
\end{aligned}$$

# Appendix F: Derivation of Lagrangian for TUSK

---

To find the tether kinetic energy, consider a differential element on the tether at a distance  $s$  away from its origin. Its position vector is given by

$$\mathbf{r} = \begin{bmatrix} s \cos(q_2) \sin(q_3) \\ s \sin(q_2) \\ s \cos(q_2) \cos(q_3) \end{bmatrix} \quad (\text{F.1})$$

Since the tether is rigid,  $\dot{s} = \dot{q}_1$ . Now we differentiate to find the velocity of the point on the tether.

$$\dot{\mathbf{r}} = \frac{d\mathbf{r}}{dt} = \begin{bmatrix} \dot{q}_1 \cos(q_2) \sin(q_3) - s\dot{q}_2 \sin(q_2) \sin(q_3) + s\dot{q}_3 \cos(q_2) \cos(q_3) \\ \dot{q}_1 \sin(q_2) + s\dot{q}_2 \cos(q_2) \\ \dot{q}_1 \cos(q_2) \cos(q_3) - s\dot{q}_2 \sin(q_2) \cos(q_3) + s\dot{q}_3 \cos(q_2) \sin(q_3) \end{bmatrix} \quad (\text{F.2})$$

Now, we integrate over the tether to find the total kinetic energy. Note that  $\rho$  is a linear density of the tether ( $\frac{\text{mass}}{\text{length}}$ ).

$$K_{tether} = \int_{tether} \frac{1}{2} \|\dot{\mathbf{r}}\|^2 dm = \frac{\rho}{2} \int_0^{q_1} |\dot{\mathbf{r}}|^2 ds \quad (\text{F.3})$$

$$K_{tether} = \frac{\rho}{2} \int_0^{q_1} \left\{ [\dot{q}_1 \cos(q_2) \sin(q_3) - s\dot{q}_2 \sin(q_2) \sin(q_3) + s\dot{q}_3 \cos(q_2) \cos(q_3)]^2 + [\dot{q}_1 \sin(q_2) + s\dot{q}_2 \cos(q_2)]^2 + [\dot{q}_1 \cos(q_2) \cos(q_3) - s\dot{q}_2 \sin(q_2) \cos(q_3) + s\dot{q}_3 \cos(q_2) \sin(q_3)]^2 \right\} ds \quad (\text{F.4})$$

$$K_{tether} = \frac{\rho}{2} \left[ \frac{(\dot{q}_1 \cos(q_2) \sin(q_3) - s\dot{q}_2 \sin(q_2) \cos(q_3) - s\dot{q}_3 \cos(q_2) \sin(q_3))^3}{3(-\dot{q}_2 \sin(q_2) \cos(q_3) + \dot{q}_3 \cos(q_2) \cos(q_3))} + \frac{(\dot{q}_1 \sin(q_2) + s\dot{q}_2 \cos(q_2))^3}{3(\dot{q}_2 \cos(q_2))} + \frac{(\dot{q}_1 \cos(q_2) \cos(q_3) - s\dot{q}_2 \sin(q_2) \cos(q_3) - s\dot{q}_3 \cos(q_2) \sin(q_3))^3}{3(-\dot{q}_2 \sin(q_2) \cos(q_3) - \dot{q}_3 \cos(q_2) \sin(q_3))} \right]_0^{q_1} \quad (\text{F.5})$$

After evaluating the bounds of integration, the numerator of each fraction becomes the difference of perfect cubes like  $a^3 - b^3$  which can be factored as  $(a - b)(a^2 + ab + b^2)$ . In this separation, the  $(a - b)$  term in each fraction will cancel its corresponding denominator, simplifying the kinetic energy to

$$\begin{aligned}
K_{tether} = \frac{\rho q_1}{6} \{ & 3\dot{q}_1^2 \cos^2(q_2) + 3\dot{q}_1^2 \sin^2(q_1) + q_1^2 \dot{q}_3^2 \cos^2(q_2) - 3q_1 \dot{q}_1 \dot{q}_2 \sin(q_2) \cos(q_2) \\
& - 3q_1 \dot{q}_1 \dot{q}_2 \sin(q_2) \cos(q_2) + 3q_1 \dot{q}_1 \dot{q}_3 \sin(q_2) \cos(q_2) - 3q_1 \dot{q}_1 \dot{q}_3 \sin(q_2) \cos(q_3) \\
& + q_1^2 \dot{q}_2^2 \sin^2(q_2) + q_1^2 \dot{q}_2^2 \cos^2(q_2) \}
\end{aligned} \tag{F.6}$$

$$K_{tether} = \frac{\rho q_1}{6} [3\dot{q}_1^2 + q_1^2 (\dot{q}_2^2 + \dot{q}_3^2 \cos(q_2))] \tag{F.7}$$

Now we need to find the kinetic energy of the boat. This kinetic energy has two components, translational and rotational. The translational kinetic energy only involves the generalized coordinates  $q_1, q_2$ , and  $q_3$ , while the rotational kinetic energy only involves the coordinates  $q_4, q_5$ , and  $q_6$ .

$$K_{kite} = \underbrace{\frac{M}{2} |\dot{\mathbf{r}}_{s=q_1}|^2}_{\text{Translational}} + \underbrace{\frac{1}{2} \boldsymbol{\omega} \cdot J \boldsymbol{\omega}}_{\text{Rotational}} \tag{F.8}$$

First, focus on the translational kite kinetic energy.

$$K_{kite,trans} = \frac{M}{2} |\dot{\mathbf{r}}_{s=q_1}|^2 \tag{F.9}$$

$$\begin{aligned}
K_{kite,trans} = & [\dot{q}_1 \cos(q_2) \sin(q_3) - q_1 \dot{q}_2 \sin(q_2) \sin(q_3) + q_1 \dot{q}_3 \cos(q_2) \cos(q_3)]^2 \\
& + [q_1^2 \sin^2(q_2) + q_1 \dot{q}_2 \cos(q_2)]^2 \\
& + [q_1 \cos(q_2) \cos(q_3) - q_1 \dot{q}_2 \sin(q_2) \cos(q_3) - q_1 \dot{q}_3 \cos(q_2) \sin(q_3)]^2
\end{aligned} \tag{F.10}$$

Squaring each of these terms out and simplifying gives:

$$K_{kite,trans} = \frac{M}{2} [\dot{q}_1^2 + q_1^2 (\dot{q}_2^2 + \dot{q}_3^2 \cos^2(q_2))] \tag{F.11}$$

Now, to find the rotational kinetic energy, we must find the angular velocity vector in terms of the rate of change of the Euler angles  $q_4, q_5$ , and  $q_6$  using the addition theorem for angular velocities.

$$\begin{bmatrix} \omega_1 \\ \omega_2 \\ \omega_3 \end{bmatrix} = \begin{bmatrix} 1 & 0 & -\sin(q_5) \\ 0 & \cos(q_4) & \sin(q_4) \cos(q_5) \\ 0 & -\sin(q_4) & \cos(q_4) \cos(q_5) \end{bmatrix} \begin{bmatrix} \dot{q}_4 \\ \dot{q}_5 \\ \dot{q}_6 \end{bmatrix} \quad (\text{F.12})$$

$$\begin{bmatrix} \omega_1 \\ \omega_2 \\ \omega_3 \end{bmatrix} = \begin{bmatrix} \dot{q}_4 - \dot{q}_6 \sin(q_5) \\ \dot{q}_5 \cos(q_4) + \dot{q}_6 \sin(q_4) \cos(q_5) \\ -\dot{q}_5 \sin(q_4) + \dot{q}_6 \cos(q_4) \cos(q_5) \end{bmatrix} \quad (\text{F.13})$$

Also, we can assume that the inertia tensor,  $J$ , is diagonal in the form:

$$J = \begin{bmatrix} J_1 & 0 & 0 \\ 0 & J_2 & 0 \\ 0 & 0 & J_3 \end{bmatrix} \quad (\text{F.14})$$

Now we can calculate the rotational kinetic energy.

$$K_{kite,rot} = \frac{1}{2} \boldsymbol{\omega} \cdot J \cdot \boldsymbol{\omega} = \frac{1}{2} [J_1 \omega_1^2 + J_2 \omega_2^2 + J_3 \omega_3^2] \quad (\text{F.15})$$

$$K_{kite,rot} = \frac{1}{2} [J_1 (\dot{q}_4 - \dot{q}_6 \sin(q_5))^2 + J_2 (\dot{q}_5 \cos(q_4) + \dot{q}_6 \sin(q_4) \cos(q_5))^2 + J_3 (-\dot{q}_5 \sin(q_4) + \dot{q}_6 \cos(q_4) \cos(q_5))^2] \quad (\text{F.16})$$

Now, to complete the Lagrangian, we need to include the potential energy. The only potential energy of the system is the gravitational and buoyancy potential energy due to the tether and boat.

$$U = \frac{1}{2} (\rho - \rho_b) g q_1^2 \cos(q_2) \cos(q_3) - Mg(RB) q_1 \cos(q_2) \cos(q_3) \quad (\text{F.17})$$

The boat has reserve buoyancy  $(RB) = \frac{F_B - Mg}{Mg}$  and buoyant density  $\rho_b$  (buoyancy per unit volume). Now the final Lagrangian becomes

$$\begin{aligned}
\mathcal{L} = & \frac{1}{2} [J_1 (\dot{q}_4 - \dot{q}_6 \sin(q_5))^2 + J_2 (\dot{q}_5 \cos(q_4) + \dot{q}_6 \sin(q_4) \cos(q_5))^2 + J_3 (-\dot{q}_5 \sin(q_4) \\
& + \dot{q}_6 \cos(q_4) \cos(q_5))^2] + \frac{\rho q_1}{6} [3\dot{q}_1^2 + q_1^2 (\dot{q}_2^2 + \dot{q}_3^2 \cos(q_2))] + \frac{M}{2} [\dot{q}_1^2 + q_1^2 (\dot{q}_2^2 + \dot{q}_3^2 \cos^2(q_2))] \\
& - \frac{1}{2} (\rho_c - \rho_b) g q_1^2 \cos(q_2) \cos(q_3) + Mg(RB)q_1 \cos(q_2) \cos(q_3)
\end{aligned}
\tag{F.18}$$

# Appendix G: Equations of Motion from Derived Lagrangian

---

Using the Lagrangian given by Equation F.18, the equations of motion given in Appendix E can be re-derived using the Euler Lagrange equation, given by Equation 5.2, applied to each of the six generalized coordinates:  $q_1$ ,  $q_2$ ,  $q_3$ ,  $q_4$ ,  $q_5$ , and  $q_6$ .

First, apply Equation 5.2 for the  $q_1$  coordinate.

$$\frac{d}{dt} \left( \frac{\partial \mathcal{L}}{\partial \dot{q}_1} \right) - \frac{\partial \mathcal{L}}{\partial q_1} = Q_{q_1} \quad (\text{G.1})$$

$$\begin{aligned} \frac{d}{dt} [\rho \dot{q}_1 q_1 + M \dot{q}_1] - \frac{\rho \dot{q}_1^2}{2} - \frac{\rho q_1^2}{2} [\dot{q}_2^2 + \dot{q}_3^2 \cos^2(q_2)] - M q_1 [\dot{q}_2^2 + \dot{q}_3^2 \cos^2(q_2)] \\ + \rho g q_1 \cos(q_2) \cos(q_3) + M g \cos(q_2) \cos(q_3) = Q_{q_1} \end{aligned} \quad (\text{G.2})$$

This can be rearranged and solved for  $\ddot{q}_1$ .

$$\begin{aligned} \ddot{q}_1 = - \left[ -Q_{q_1} + m g \cos(q_2) \cos(q_3) \right. \\ \left. + \frac{1}{2} [2g\rho q_1 \cos(q_2) \cos(q_3) + \rho \dot{q}_1^2 - 2M q_1 \dot{q}_2^2 - \rho q_1^2 \dot{q}_2^2 - q_1 \cos^2(q_2)(2M + \rho q_1) \dot{q}_3^2] \right] \end{aligned} \quad (\text{G.3})$$

Now, apply Equation 5.2 for the  $q_2$  coordinate and perform some trigonometric simplifications.

$$\begin{aligned} \frac{d}{dt} \left[ \frac{\rho q_1^3 \dot{q}_2}{3} + M q_1^2 \dot{q}_2 \right] + \frac{\rho q_1^3 \dot{q}_3^2 \sin(2q_2)}{6} + \frac{M q_1^2 \dot{q}_3^2 \sin(2q_2)}{2} \\ - \frac{1}{2} (\rho - \rho_b) g q_1^2 \sin(q_2) \cos(q_3) + M g (RB) q_1 \sin(q_2) \cos(q_3) = Q_{q_2} \end{aligned} \quad (\text{G.4})$$

Solving for  $\ddot{q}_2$  yields

$$\begin{aligned} \ddot{q}_2 = -3 \cdot \left[ -Q_{q_2} - g \cos(q_3) q_1 [-2M(RB) + (\rho - \rho_b) q_1] \cdot \frac{\sin(q_2)}{2} \right. \\ \left. + q_2 (2m + \rho q_1) \dot{q}_1 \dot{q}_2 + \frac{1}{6} [q_1^2 (3m + \rho q_1) \sin(2q_2) \dot{q}_3^2] \right] \cdot \frac{1}{q_1^2 (3m + \rho q_1^2)} \end{aligned} \quad (\text{G.5})$$

Now, apply Equation 5.2 for the  $q_3$  coordinate and perform some trigonometric simplifications.

$$\begin{aligned} \frac{d}{dt} \left[ \frac{\rho q_1^3 \dot{q}_3 \cos^2(q_2)}{3} + M q_1^2 \dot{q}_3 \cos^2(q_2) \right] - \frac{1}{2}(\rho - \rho_b) g q_1^2 \cos(q_2) \sin(q_3) \\ + M g (RB) q_1 \cos(q_2) \sin(q_3) = Q_{q_3} \end{aligned} \quad (\text{G.6})$$

$$\begin{aligned} \ddot{q}_3 = -3 \sec^2(q_2) \cdot \left[ -Q_{q_3} - g \cos(q_2) q_1 [-2M(RB) + (\rho - \rho_b) q_1] \cdot \frac{\sin(q_3)}{2} \right. \\ \left. + q_1 \cos^2(q_2) (2M + \rho q_1) \dot{q}_1 \dot{q}_3 - 2 \cos(q_2) q_1^2 (3M + \rho q_1) \dot{q}_2 \dot{q}_3 \frac{\sin(q_2)}{3} \right] \cdot \frac{1}{q_1^2 (3M + \rho q_1)} \end{aligned} \quad (\text{G.7})$$

As expected, equations G.3, G.5, and G.7 match equations E.1, E.2, and E.3 respectively.

The derivations of the equations of motion for  $q_4$ ,  $q_5$ , and  $q_6$  are more complicated, as those three coordinates are more coupled. There will be acceleration terms of each coordinate present in each equation obtained from the Euler-Lagrange equation. To verify the equations without much simplification, numerical results were tested in MATLAB. First, applying the Euler-Lagrange equation in the  $q_4$  variable gives

$$\begin{aligned} \frac{d}{dt} [2J_1 \dot{q}_4 - 2J_1 \dot{q}_6 \sin(q_5)] - [-J_2 \dot{q}_5^2 \sin(2q_4) + 2J_2 \dot{q}_5 \dot{q}_6 \cos(2q_4) \cos(q_5) \\ + J_2 \dot{q}_6^2 \sin(2q_4) \cos^2(q_5) + J_3 \dot{q}_5^2 \sin(2q_4) \\ - 2J_3 \dot{q}_5 \dot{q}_6 \cos(2q_4) \cos(q_5) - J_3 \dot{q}_6^2 \sin(2q_4) \cos^2(q_5)] = 2Q_{q_4} \end{aligned} \quad (\text{G.8})$$

This can be expanded and simplified to

$$\begin{aligned} 2J_1 \ddot{q}_4 - 2J_1 \ddot{q}_6 \sin(q_5) - 2J_1 \dot{q}_5 \dot{q}_6 \cos(q_5) = -J_2 \dot{q}_5^2 \sin(2q_4) \\ + 2J_2 \dot{q}_5 \dot{q}_6 \cos(2q_4) \cos(q_5) + J_2 \dot{q}_6^2 \sin(2q_4) \cos^2(q_5) + J_3 \dot{q}_5^2 \sin(2q_4) \\ - 2J_3 \dot{q}_5 \dot{q}_6 \cos(2q_4) \cos(q_5) - J_3 \dot{q}_6^2 \sin(2q_4) \cos^2(q_5) + 2Q_{q_4} \end{aligned} \quad (\text{G.9})$$

Next, applying it in the  $q_5$  variable yields

$$\begin{aligned} \frac{d}{dt} [2J_2 \dot{q}_5 \cos^2(q_4) + J_2 \dot{q}_6 \sin(2q_4) \cos(q_5) + 2J_3 \dot{q}_5 \sin^2(q_4) - J_3 \dot{q}_6 \sin(2q_4) \cos(q_5)] \\ - [-2J_1 \dot{q}_4 \dot{q}_6 \cos(q_5) + J_1 \dot{q}_6^2 \sin(2q_5) - J_2 \dot{q}_5 \dot{q}_6 \sin(2q_4) \sin(q_5) - J_2 \dot{q}_6^2 \sin^2(q_4) \sin(2q_5) \\ + J_3 \dot{q}_5 \dot{q}_6 \sin(2q_4) \sin(q_5) - J_3 \dot{q}_6^2 \cos^2(q_4) \sin(2q_5)] = 2Q_{q_5} \end{aligned} \quad (\text{G.10})$$

Simplifying this, one obtains

$$\begin{aligned}
& 2J_2\ddot{q}_5 \cos^2(q_4) - 2J_2\dot{q}_4\dot{q}_5 \sin(2q_4) + J_2\ddot{q}_6 \sin(2q_4) \cos(q_5) + 2J_2\dot{q}_4\dot{q}_6 \cos(2q_4) \cos(q_5) \\
& - J_2\dot{q}_5\dot{q}_6 \sin(2q_4) \sin(q_5) + 2J_3\ddot{q}_5 \sin^2(q_4) + 2J_3\dot{q}_4\dot{q}_5 \sin(2q_4) - J_3\ddot{q}_6 \sin(2q_4) \cos(q_5) \\
& - 2J_3\dot{q}_4\dot{q}_6 \cos(2q_4) \cos(q_5) + J_3\dot{q}_5\dot{q}_6 \sin(2q_4) \sin(q_5) = -2J_1\dot{q}_4\dot{q}_6 \cos(q_5) \quad (\text{G.11}) \\
& + J_1\dot{q}_6^2 \sin(2q_5) - J_2\dot{q}_5\dot{q}_6 \sin(2q_4) \sin(q_5) - J_2\dot{q}_6^2 \sin^2(q_4) \sin(2q_5) \\
& + J_3\dot{q}_5\dot{q}_6 \sin(2q_4) \sin(q_5) - J_3\dot{q}_6^2 \cos^2(q_4) \sin(2q_5) + 2Q_{q_5}
\end{aligned}$$

Finally, applying the Euler-Lagrange equation in the  $q_6$  variable gives

$$\begin{aligned}
& \frac{d}{dt} \left[ -2J_1\dot{q}_4 \sin(q_5) + 2J_1\dot{q}_6 \sin^2(q_5) + J_2\dot{q}_5 \sin(2q_4) \cos(q_5) \right. \\
& \left. + 2J_2\dot{q}_6 \sin^2(q_4) \cos^2(q_5) - J_3\dot{q}_5 \sin(2q_4) \cos(q_5) + 2J_3\dot{q}_6 \cos^2(q_4) \cos^2(q_5) \right] = 2Q_{q_6} \quad (\text{G.12})
\end{aligned}$$

A final simplification results in

$$\begin{aligned}
& -2J_1\ddot{q}_4 \sin(q_5) - 2J_1\dot{q}_4\dot{q}_5 \cos(q_5) + 2J_1\ddot{q}_6 \sin^2(q_5) + 2J_1\dot{q}_6\dot{q}_5 \sin(2q_5) \\
& + J_2\ddot{q}_5 \sin(2q_4) \cos(q_5) + 2J_2\dot{q}_4\dot{q}_5 \cos(2q_4) \cos(q_5) - J_2\dot{q}_5^2 \sin(2q_4) \sin(q_5) \\
& + 2J_2\ddot{q}_6 \sin^2(q_4) \cos^2(q_5) + 2J_2\dot{q}_4\dot{q}_6 \sin(2q_4) \cos^2(q_6) - 2J_2\dot{q}_5\dot{q}_6 \sin^2(q_4) \sin(2q_5) \\
& - J_3\ddot{q}_5 \sin(2q_4) \cos(q_5) - 2J_3\dot{q}_4\dot{q}_5 \cos(2q_4) \cos(q_5) + J_3\dot{q}_5^2 \sin(2q_4) \sin(q_5) \\
& + 2J_3\ddot{q}_6 \cos^2(q_4) \cos^2(q_5) - 2J_3\dot{q}_4\dot{q}_6 \sin(2q_4) \cos^2(q_5) - 2J_3\dot{q}_5\dot{q}_6 \cos^2(q_4) \sin(2q_5) = 2Q_{q_6} \quad (\text{G.13})
\end{aligned}$$

It was confirmed numerically using MATLAB that Equations G.9, G.11, and G.13 provide the same results for  $\ddot{q}_4$ ,  $\ddot{q}_5$ , and  $\ddot{q}_6$  as Equations E.4, E.5, and E.6, finalizing the derivation and validation of the TUSK equations of motion.



## Appendix H: Derivation of SUSK Lagrangian

---

Consider a boat as a point mass on the end of a uniformly dense tether. As the tether has constant length, it can be described completely by one coordinate,  $q_2$  (for consistency with previous derivations). To find the kinetic energy of the system, consider the tether and the point mass separately. Consider a differential element of the tether located at distance  $s$  from the origin. Along the tether,  $s$  varies between 0 and  $L$ .

$$dK = \frac{1}{2}v^2 dm = \frac{1}{2}(s\dot{q}_2)^2(\rho ds) \quad (\text{H.1})$$

Integrate along the tether to get the total energy of the tether.

$$K_{tether} = \frac{\rho\dot{q}_2^2}{2} \int_0^L s^2 ds = \frac{\rho\dot{q}_2^2 L_t^3}{6} \quad (\text{H.2})$$

Next, the kinetic energy of the boat is given by

$$K_{boat} = \frac{1}{2}Mv^2 = \frac{ML_t^2\dot{q}_2^2}{2} \quad (\text{H.3})$$

As the boat stays on the surface of the water, which is equipotential for gravitational and buoyant potential energies, the potential energy can be taken as zero. This gives that the Lagrangian is simply the kinetic energy.

$$\mathcal{L} = \frac{L_t^2}{2} \left[ \frac{\rho L_t}{3} + M \right] \dot{q}_2^2 \quad (\text{H.4})$$

The Euler-Lagrange equation in the  $q_2$  variable is

$$\frac{d}{dt} \left( \frac{\partial \mathcal{L}}{\partial \dot{q}_2} \right) - \frac{\partial \mathcal{L}}{\partial q_2} = Q_{q_2} \quad (\text{H.5})$$

Applying Equation H.5 in the  $q_2$  variable gives the equation of motion,

$$\ddot{q}_2 = \frac{Q_{q_2}}{L_t^2} \left[ \frac{\rho L_t}{3} + M \right]^{-1}, \quad (\text{H.6})$$

which matches Equations I.3 and 5.3.

# Appendix I: Derivation of Boat Equations of Motion Using Newton's Laws

---

Using Newton's Second Law in its rotational form, given by Equation I.1, provides an alternate derivation of boat motion that is consistent with the Lagrangian formulation.

$$\sum \tau = I\alpha = I\ddot{\theta} \quad (\text{I.1})$$

Summing the torques on the boat and tether system about the gimbal (fixed point on the tether) gives the equation

$$\left( ML_t^2 + \frac{\rho L_t^3}{3} \right) \ddot{q}_2 = Q_{q_2} \quad (\text{I.2})$$

which makes use of the moment of inertia of a rod about its end  $\frac{ML^2}{3}$ . Simplifying this equation gives

$$\ddot{q}_2 = \frac{Q_{q_2}}{L_t^2} \left[ \frac{\rho L_t}{3} + M \right]^{-1} \quad (\text{I.3})$$

which is identical to Equation H.6.

# Appendix J: MATLAB<sup>®</sup> Code for Dynamic Simulations

---

Main script:

```
clc;
clear variables;
close all;

global Qq2 L rho M q2lim vcurrent Qq6 J2 S A_t rho_t
global C_p Servo_Torque A_b Re visc Servo_Speed

size = 'small';
%Make 'small' if for model, make 'large' if for prototype (full size) system

l_boat = 0.4;           % Boat Length (m)
w_boat = 0.2;           % Boat Width (m)
visc = 1E-3;           % Viscosity of Water (N*s/m^2)
A_b = l_boat*w_boat;   % Area of Boat (m^2)
Servo_Speed = 1.165;   % Angular Velocity of Servo (rad/s)
L = 3.66;              % Tether Length (m)
M = 2.4;               % Boat Mass (kg)
rho = 1025;            % Density of Water (m/s)
q2lim = 40*pi/180;     % Limit Angle (rad)
vcurrent = 0.4572;     % Ambient Current Velocity (m/s)
S = 0.05;              % Wing Area (m^2)
A_t = pi*0.074^2;      % Turbine Area (m^2)
rho_t = 0.2;           % Tether Linear Density (kg/m)
C_p = 16/27;           % Turbine Power Coefficient

SF = 20;               % Scale Factor

if strcmp(size,'large')
l_boat = l_boat*SF;
w_boat = w_boat*SF;
visc = visc*1;
A_b = l_boat*w_boat;
Servo_Torque = Servo_Torque*1;
Servo_Speed = Servo_Speed*1;
L = L*2*SF;
M = M*SF^3;
rho = rho*1;
Qq2 = Qq2*1;
q2lim = q2lim*1;
```

```

vcurrent = vcurrent*sqrt(SF);
Qq6 = Qq6*1;
J2 = J2*SF^5;
S = S*SF^2;
A_t = A_t*SF^2;
rho_t = rho_t*SF^2;
C_p = C_p*1;
end

iterations = 10000; % Must be sufficiently big to prevent numerical error
subiterations = 5; % Must be bigger than 4
tinit = 0;
tfinal = 125;

q2_init = -43*pi/180; % Initial Boat Position
q2dot_init = -0.01; % Initial Boat Velocity
theta_init = 0; % Initial Wing Position
thetadot_init = 0; % Initial Wing Velocity

q2_cum = zeros(1,(subiterations - 1)*iterations); % Cumulative Boat Position Array
q2dot_cum = zeros(1,(subiterations - 1)*iterations); % Cumulative Boat Angular Velocity Array
alpha_cum = zeros(1,(subiterations - 1)*iterations); % Cumulative Angle of Attack Array
t_cum = zeros(1,(subiterations - 1)*iterations); % Cumulative Time Array
power_cum = zeros(1,(subiterations - 1)*iterations); % Cumulative Power Array
vctotal_cum = zeros(1,(subiterations - 1)*iterations); % Cumulative Apparent Velocity Array
tension_cum = zeros(1,(subiterations - 1)*iterations); % Cumulative Tension Array
moment_cum = zeros(1,(subiterations - 1)*iterations); % Cumulative Tether Moment Array
theta_cum = zeros(1,(subiterations - 1)*iterations); % Cumulative Wing Position Array
thetadot_cum = zeros(1,(subiterations - 1)*iterations); % Cumulative Wing Angular Velocity Array
loverd_cum = zeros(1,(subiterations - 1)*iterations); % Cumulative Lift to Drag Array

for n = 1:iterations
    if abs(q2dot_init) > 100
        break
    end
    fprintf('Iteration %i/%i, %g%% Completed \n',...
        [n iterations n/iterations*100]); % Iteration Counte
    tspanfinal = (tfinal - tinit)/iterations*n;
    tspaninit = (tfinal - tinit)/iterations*(n-1);
    tsubspan = linspace(tspaninit, tspanfinal, subiterations);

    vcurrent_vec = [0; vcurrent; 0]; %Current Vector

    rboat_vec = [-L*sin(q2_init); L*cos(q2_init); 0]; % Boat Position Vector

```

```

vboat_vec = [-L*q2dot_init*cos(q2_init); -L*q2dot_init*sin(q2_init); 0]; % Boat Velocity Vector
boat_hat = [cos(q2_init); sin(q2_init); 0]; % Boat Velocity Vector Direction
vinduced_vec = -vboat_vec; % Induced Current Velocity Due to Boat Motion

vctotal_vec = vinduced_vec + vcurrent_vec; % Total Current Velocity Vector
vctotal = norm(vctotal_vec); % Total Current Speed

w_angle = q2_init + theta_init; % Angle of Initial Right Edge of Wing
w_hat = [cos(w_angle); sin(w_angle); 0]; % Unit Vector Pointing off Initial Right Edge of Wing

cosalpha = dot(w_hat, vctotal_vec)/vctotal; % Cosine of Angle of Attack

if cosalpha >= 0
    vel_direction = atan2(vctotal_vec(2), vctotal_vec(1));
    if abs(vel_direction - w_angle) >= pi/2
        if vel_direction < w_angle
            vel_direction = vel_direction + 2*pi;
        else
            w_angle = w_angle + 2*pi;
        end
    end
    if vel_direction >= w_angle
        alpha = acos(cosalpha);
    elseif vel_direction < w_angle
        alpha = -acos(cosalpha);
    end
    alpha_deg = alpha*180/pi;
    [CL, CD] = getliftanddragcoeff(alpha_deg);
    Lift = 0.5*rho*vctotal^2*S*CL;
    Drag = 0.5*rho*vctotal^2*S*CD;
    Drag_0ther = turbine_and_boat_drag(vctotal);
    Drag = Drag + Drag_0ther;
    Force_Normal_To_Wing = Lift*cos(alpha) + Drag*sin(alpha);
    Force_Axial_To_Wing = -Lift*sin(alpha) + Drag*cos(alpha);
    Force_Along_Tether = Force_Normal_To_Wing*sin(theta_init) - Force_Axial_To_Wing*cos(theta_init);
elseif cosalpha < 0
    vel_direction = atan2(vctotal_vec(2), vctotal_vec(1));
    psi1 = mod(vel_direction,2*pi);
    psi2 = mod((w_angle + pi),2*pi);
    if abs(psi1 - psi2) >= pi/2
        if psi1 < psi2
            psi1 = psi1 + 2*pi;
        else
            psi2 = psi2 + 2*pi;
        end
    end
end

```

```

        end
    end
    if psi1 >= psi2
        alpha = -acos(-cosalpha);
    elseif psi2 > psi1
        alpha = acos(-cosalpha);
    end
    alpha_deg = alpha*180/pi;
    [CL, CD] = getliftanddragcoeff(alpha_deg);
    Lift = 0.5*rho*vctotal^2*S*CL;
    Drag = 0.5*rho*vctotal^2*S*CD;
    Drag_Other = turbine_and_boat_drag(vctotal);
    Drag = Drag + Drag_Other;
    Force_Normal_To_Wing = Lift*cos(alpha) + Drag*sin(alpha);
    Force_Axial_To_Wing = Lift*sin(alpha) - Drag*cos(alpha);
    Force_Along_Tether = Force_Normal_To_Wing*sin(theta_init) - Force_Axial_To_Wing*cos(theta_init);
end
Tether_Tension = sqrt(Lift^2 + Drag^2 - Force_Along_Tether^2);
Re = rho*vctotal*l_boat/visc;
Qq2 = L*Force_Along_Tether;

%trim_thetas = [1.3 -0.3 -0.3 -1.3 1.3 0.3 0.3 -1.3];
%trim_thetas = [1.2 -0.4 -0.4 -1.2 1.2 0.4 0.4 -1.2];
trim_thetas = [41 -38 -46 -46 41 41 34 -46]*pi/180;

position_and_speed_case = 1;
if q2dot_init < 0
    if q2_init < -q2lim
        position_and_speed_case = 1;
    elseif q2_init < 0
        position_and_speed_case = 2;
    elseif q2_init >= 0 && q2_init <= q2lim
        position_and_speed_case = 3;
    elseif q2_init > q2lim
        position_and_speed_case = 4;
    end
elseif q2dot_init >= 0
    if q2_init < -q2lim
        position_and_speed_case = 5;
    elseif q2_init < 0
        position_and_speed_case = 6;
    elseif q2_init >= 0 && q2_init <= q2lim
        position_and_speed_case = 7;

```

```

elseif q2_init > q2lim
    position_and_speed_case = 8;
end
end

% Move Servo if needed
if abs(trim_thetas(position_and_speed_case) - theta_init) > 0.02
    thetadot_init = sign(trim_thetas(position_and_speed_case) - theta_init)*Servo_Speed;
else
    thetadot_init = 0;
end

% Equations of motion (ODE45 not used to save time)
% [t,q] = ode45(@(t,q) Simple_ODE(t,q), tsubspan, [q2_init; q2dot_init; theta_init; thetadot_init]);
q(:,1) = Qq2/L^2*(rho_t*L/3 + M)^(-1)*(tsubspan - tsubspan(1)).^2/2 + ...
    q2dot_init*(tsubspan - tsubspan(1)) + q2_init;
q(:,2) = Qq2/L^2*(rho_t*L/3 + M)^(-1)*(tsubspan - tsubspan(1)) + q2dot_init;
q(:,3) = theta_init + thetadot_init*(tsubspan - tsubspan(1));
q(:,4) = thetadot_init;

% Calculate Lift to Drag Ratio
loverd = Lift/Drag;

% Add to cumulative arrays of coordinates
q2_cum((n-1)*(subiterations - 1) + 1:n*(subiterations - 1)) = q(1:end-1,1);
q2dot_cum((n-1)*(subiterations - 1) + 1:n*(subiterations - 1)) = q(1:end-1,2);
theta_cum((n-1)*(subiterations - 1) + 1:n*(subiterations - 1)) = q(1:end-1,3);
thetadot_cum((n-1)*(subiterations - 1) + 1:n*(subiterations - 1)) = q(1:end-1,4);
alpha_cum((n-1)*(subiterations - 1) + 1:n*(subiterations - 1)) = alpha;

% End of previous interval becomes new initial conditions
q2_init = q(end,1);
q2dot_init = q(end,2);
theta_init = q(end,3);
thetadot_init = q(end,4);

% Add to cumulative arrays
tension_cum((n-1)*(subiterations - 1) + 1:n*(subiterations - 1)) = Tether_Tension;
moment_cum((n-1)*(subiterations - 1) + 1:n*(subiterations - 1)) = Qq2;

```

```

t_cum((n-1)*(subiterations - 1) + 1:n*(subiterations - 1)) = tsubspan(1:end-1);
vctotal_cum((n-1)*(subiterations - 1) + 1:n*(subiterations - 1)) = vctotal;
power_cum((n-1)*(subiterations - 1) + 1:n*(subiterations - 1)) = ...
    abs(C_p*0.5*rho*vctotal^2*A_t*dot(vctotal_vec,[sin(q2_init); cos(q2_init); 0]));
loverd_cum((n-1)*(subiterations - 1) + 1:n*(subiterations - 1)) = loverd;
end

%% Plotting

close all;

cartesian_cum = [L*cos(q2_cum); -L*sin(q2_cum); 0*q2_cum];
limit_cartesian1 = [L*cos(q2lim); -L*sin(q2lim); 0];
limit_cartesian2 = [L*cos(q2lim); L*sin(q2lim); 0];
x = cartesian_cum(1,:);
y = cartesian_cum(2,:);
z = cartesian_cum(3,:);

figure('name','q2andq2dot');
subplot(5,1,1)
plot(t_cum, q2_cum*180/pi,'linewidth',2);
ylabel('$$$q_2$ (deg)$$','fontsize',14,'interpreter','latex');
title('q_2 vs t','fontsize',14);
subplot(5,1,2)
plot(t_cum, q2dot_cum*180/pi,'linewidth',2);
ylabel('$$\dot{q}_2$ \left(\frac{deg}{s}\right)$$','fontsize',14,'interpreter','latex');
title('q_2dot vs t','fontsize',14);
subplot(5,1,3)
plot(t_cum, theta_cum*180/pi,'linewidth',2);
ylabel('$$\theta$ (deg)$$','fontsize',14,'interpreter','latex');
title('\theta vs t','fontsize',14);
subplot(5,1,4)
plot(t_cum, thetadot_cum*180/pi,'linewidth',2);
ylabel('$$\dot{\theta}$ \left(\frac{deg}{s}\right)$$','fontsize',14,'interpreter','latex');
title('\theta dot vs t','fontsize',14);
subplot(5,1,5)
plot(t_cum, alpha_cum*180/pi,'linewidth',2);
xlabel('$$$t$$$','fontsize',18,'interpreter','latex');
ylabel('$$\alpha$ (deg)$$','fontsize',14,'interpreter','latex');
title('\alpha vs t','fontsize',14);
fig = gcf;
fig.PaperUnits = 'inches';
fig.PaperPosition = [0 0 5 7];
print('MostRecentangles','-dpng')

```



```

figure('name','vctotal');
subplot(5,1,1)
plot(t_cum, vctotal_cum/vcurrent,'linewidth',2);
ylabel('$$\frac{V_a}{V_{current}}$$','interpreter','latex','fontsize',16);
title('Apparent Velocity as a multiple of current velocity vs t','fontsize',14)
subplot(5,1,2)
plot(t_cum, tension_cum,'linewidth',2);
ylabel('Tether Tension (N)','fontsize',14);
title('Tether Tension vs t','fontsize',14)
subplot(5,1,3)
plot(t_cum, moment_cum,'linewidth',2);
ylabel('$$Qq^2 (N\cdot m)$$','fontsize',14);
title('Qq2 vs t','fontsize',14)
subplot(5,1,4)
plot(t_cum, power_cum,'linewidth',2);
ylabel('Power (W)','fontsize',14);
title('Power vs t','fontsize',14);
subplot(5,1,5)
plot(t_cum,loverd_cum,'linewidth',2);
ylabel('$$\frac{L}{D}$$','fontsize',14,'interpreter','latex')
xlabel('t (s)','fontsize',18)
title('Lift to Drag Ratio vs t','fontsize',14)
fig = gcf;
fig.PaperUnits = 'inches';
fig.PaperPosition = [0 0 7 9];
print('MostRecentOther','-dpng')

figure('name','cartesian2d');
plot([0 limit_cartesian1(2)],[0 limit_cartesian1(1)],'k-.','linewidth',1.5)
hold on
plot(y,x,'linewidth',2);
hold on
plot(0,0,'o','markersize',15)
plot([0 limit_cartesian2(2)],[0 limit_cartesian2(1)],'k-.','linewidth',1.5)
axis equal
legendd = legend('q_{2,lim}');
set(legendd,'fontsize',16)
xlabel('y (m)','fontsize',14);
ylabel('x (m)','fontsize',14);
title('Cartesian Boat Position','fontsize',14)
print('MostRecentCartesian','-dpng')

```

```

% Print Average Poewr
fprintf('Average Power = %f\n', mean(power_cum));

% To make animation

% figure;
% for i = 1:length(t_cum)/100:length(t_cum);
%     plot3(x,y,z);
%     xlim([-1.1*L 1.1*L]);
%     ylim([-1.1*L 1.1*L]);
%     zlim([-1.1*L 1.1*L]);
%     hold on
%     xlabel('x');
%     ylabel('y');
%     zlabel('z');
%     title('3D Position With Tether');
%     plot3([0 x(i)], [0 y(i)], [0 z(i)], 'k');
%     plot3([0 x(i)], [0 y(i)], [0 z(i)], 'rk');
%     title(strcat('t = ', num2str(t_cum(i))));
%     plot3(x(i), y(i), z(i), '.r', 'markersize', 25);
%     pause(0.001);
%     hold off
% end

```

ODE45 function (unused in final simulation because equations of motion were explicitly solved over each time step for speed).

```
function xdot = Simple_ODE(t,x)
```

```
% q2, q2dot, theta, thetadot
```

```
global Qq2 L rho M rho_t Servo_Torque J2
```

```
xdot = ones(4,1);
```

```
xdot(1) = x(2);
```

```
xdot(2) = Qq2/L^2*(rho_t*L/3 + M)^(-1);
```

```
xdot(3) = x(4);
```

```
xdot(4) = 0;
```

Lift and drag coefficient function

```
function [cl, cd] = getliftanddragcoeff(alpha_deg)
```

```
if alpha_deg < -10 && alpha_deg >= -90
```

```
    cl = 0.00028125*alpha_deg^2 + 0.020625*alpha_deg - 0.421875;
```

```
    cd = 0.00002235577*alpha_deg^2 - 0.007014423*alpha_deg - 0.0123798;
```

```
elseif alpha_deg <= 16
```

```

c1 = -0.000376346*alpha_deg^3 + 0.00061774*alpha_deg^2 + 0.135442*alpha_deg + 0.3163;
cd = 0.000346154*alpha_deg^2 - 0.00053846*alpha_deg + 0.02;
elseif alpha_deg <= 90
c1 = -0.00044515*alpha_deg^2 + 0.032321145*alpha_deg + 0.69682035;
cd = 0.0000949879*alpha_deg^2 + 0.00749885*alpha_deg - 0.0442985;
else
disp('Error: Angle of attack exceeds 90 degrees')
end
Hull and turbine drag function
function drag = turbine_and_boat_drag(velocity)

global rho A_t A_b

turbine_drag = 4/9*velocity^2*A_t*rho;    %Betz Turbine (referenced from Olinger and Wang Paper)
%boat_drag_coeff = 1.328/sqrt(Re); %Bring in form factor????????
boat_drag_coeff = 0.35;
boat_drag = boat_drag_coeff*0.5*rho*velocity^2*A_b;
drag = turbine_drag + boat_drag;

```

# References

---

- [1] Antonello Cherubini, Andrea Papini, Rocco Vertechy, and Marco Fontana. Airborne wind energy systems: A review of the technologies. *Renewable and Sustainable Energy Reviews*, 51:1461–1476, 2015.
- [2] Moritz Diehl. Airborne wind energy: Basic concepts and physical foundations. In *Airborne Wind Energy*, pages 3–22. Springer, 2013.
- [3] David J Olinger and Yao Wang. Hydrokinetic energy harvesting using tethered undersea kites. *Journal of Renewable and Sustainable Energy*, 7(4):043114, 2015.
- [4] Hydorun harnessing hydrokinetic energy.  
<https://patentscope.wipo.int/search/en/detail.jsf?docId=WO2014063258>, 2014.
- [5] Michael Hoel and Snorre Kverndokk. Depletion of fossil fuels and the impacts of global warming. *Resource and energy economics*, 18(2):115–136, 1996.
- [6] Susan Solomon, Gian-Kasper Plattner, Reto Knutti, and Pierre Friedlingstein. Irreversible climate change due to carbon dioxide emissions. *Proceedings of the national academy of sciences*, pages pnas–0812721106, 2009.
- [7] Marilena Kampa and Elias Castanas. Human health effects of air pollution. *Environmental pollution*, 151(2):362–367, 2008.
- [8] Alana ES Duerr and Manhar R Dhanak. An assessment of the hydrokinetic energy resource of the florida current. *IEEE Journal of Oceanic Engineering*, 37(2):281–293, 2012.
- [9] Miles L Loyd. Crosswind kite power). *Journal of energy*, 4(3):106–111, 1980.
- [10] Mario Zanon, Sébastien Gros, Joel Andersson, and Moritz Diehl. Airborne wind energy based on dual airfoils. *IEEE Transactions on Control Systems Technology*, 21(4):1215–1222, 2013.
- [11] Stationary and mobile turbine motion. <http://rtcmagazine.com/articles/view/102112>, 2011. Accessed: 2016-10-26.

- [12] Energy harvesting from tethered undersea kites.  
<http://www.energyharvestingjournal.com/articles/5635/energy-harvesting-from-tethered-undersea-kites>, July 2013. Accessed:  
2016-10-26.
- [13] Windlift. <http://windlift.com/>, 2016. Accessed: 2016-10-26.
- [14] Deep green technology. <http://minesto.com/deep-green/>, 2016. Accessed: 2016-10-26.
- [15] Minesto Deep Green Technical Data.  
[minesto.com/Resources/dgtechnical-data-sheet.pdf](http://minesto.com/Resources/dgtechnical-data-sheet.pdf). Accessed: 2016-10-26.
- [16] Hydorun - technology. <http://hydorun.ca/technology/>, 2014.
- [17] Ryan Fredette. Scale-model testing of tethered undersea kites for power generation. Master's thesis, Worcester Polytechnic Institute, 2015. Accessed: 2016-10-26, Graduate Thesis Research Report No. etd-070615-124912. Available at <https://web.wpi.edu/Pubs/ETD/Available/etd-070615-124912/>.
- [18] Nyansafo Aye-Addo, James O'Connor, Randy Perez. Design of a scale-model tethered undersea kite for power generation. Technical report, Worcester Polytechnic Institute, 2014. Accessed: 2016-10-26, Undergraduate Major Qualifying Project No. E-project-050114-105311. Available at <https://web.wpi.edu/Pubs/E-project/Available/E-project-050114-105311/unrestricted/TUSK'Project'Final'AOP.pdf>.
- [19] John Anderson, Jr. *Fundamentals of Aerodynamics*. McGraw-Hill, 5th edition, 2011.
- [20] David J. McIntyre. *Quantum Mechanics: A Paradigms Approach*. Pearson, 2013.
- [21] Islam Hussein, David Olinger, and Gretar Tryggvason. Stability and control of ground tethered energy systems. In *AIAA Guidance, Navigation, and Control Conference*, page 6231, 2011.
- [22] Sighard F Hoerner. Fluid dynamic drag. 1965. *Bricktown, NJ: Published by the author*, 1992.